

# **Harnessing Buckling to Create Functionality in Origami Tubes**

by

Zhongyuan Wo

A dissertation submitted in partial fulfillment  
of the requirements for the degree of  
Doctor of Philosophy  
(Civil Engineering)  
in the University of Michigan  
2022

Doctoral Committee:

Assistant Professor Evgueni T. Filipov, Chair  
Professor Sherif El-Tawil  
Professor John A. Shaw  
Associate Professor Seymour M.J. Spence

Zhongyuan Wo  
wozhy@umich.edu  
ORCID iD: 0000-0002-9765-4697

© Zhongyuan Wo 2022

## **ACKNOWLEDGMENTS**

First and foremost, I would like express my sincere appreciation for my research advisor, Dr. Evgueni Filipov, both academically and personally. Since I joined the group, he has been constantly providing motivations, fruitful insights, and general resources that I will need to advance in my research. I have learned more than I could have ever imagined from his work ethic, professionalism, and wisdom. The training and support I have received will be a life-long treasure.

I would also to thank, Professor El-Tawil, Professor Shaw, and Professor Spence for agreeing to serve on my dissertation committee, as well as providing insightful feedback to my dissertation. This thesis would not have been accomplished without their comments and suggestions,

I would like to thank Professor McCormick for granting me the privilege of working with him as a graduate student instructor of CEE 413: Design of Metal Structures.

This dissertation is dedicated to my girlfriend, Xing Xu, whose support and encouragement have helped me overcome many difficulties during this long journey.

## TABLE OF CONTENTS

ACKNOWLEDGMENTS . . . . .	ii
LIST OF FIGURES . . . . .	v
LIST OF TABLES . . . . .	xiii
ABSTRACT . . . . .	xiv
CHAPTER	
<b>1 Introduction . . . . .</b>	<b>1</b>
1.1 A brief overview of origami-inspired morphable structures . . . . .	2
1.2 Origami-inspired tubular structures . . . . .	3
1.2.1 Origami-inspired tube applications . . . . .	3
1.2.2 Buckling in origami tubes . . . . .	5
1.2.3 Origami-inspired tube geometries . . . . .	7
1.3 Scope of the thesis . . . . .	8
<b>2 Locking Zipper-coupled Origami Tubes for Deployable Energy Absorption . . . . .</b>	<b>11</b>
2.1 Introduction . . . . .	11
2.2 System and methods . . . . .	14
2.2.1 Geometry, fabrication, and locking of origami tubes . . . . .	14
2.2.2 Finite element model . . . . .	17
2.2.3 Experimental methods . . . . .	19
2.3 Results . . . . .	25
2.3.1 Quasi-static axial tests . . . . .	25
2.3.2 Benchmark comparison . . . . .	27
2.3.3 Influence of the end constraints . . . . .	28
2.3.4 Parametric study . . . . .	30
2.3.5 Drop tests and dynamic analyses . . . . .	34
2.4 Locking mechanism . . . . .	35
2.5 Concluding remarks . . . . .	37
<b>3 Bending Stability of Corrugated Tubes with Anisotropic Frustum Shells . . . . .</b>	<b>39</b>
3.1 Introduction . . . . .	39
3.2 Geometry and model . . . . .	41

3.2.1	Geometric parameters and cross-sections . . . . .	41
3.2.2	The numerical method . . . . .	45
3.2.3	Boundary effects of the end constraints . . . . .	49
3.3	Bending stability of circular cross-sections . . . . .	50
3.3.1	Influences of thickness, frusta angle, and crease stiffness . . . . .	50
3.3.2	Verifying geometric and stiffness effects with a simple mechanism model	53
3.4	Cross-sectional influence on the bending stability . . . . .	56
3.4.1	From a circular to an orthotropic cross-section . . . . .	56
3.4.2	Cross-sections with negative curvature . . . . .	58
3.4.3	Cross-sectional effects on the energy distributions . . . . .	59
3.4.4	Energy landscapes for the orthotropic shapes . . . . .	61
3.4.5	Non-symmetric bending . . . . .	62
3.5	Physical models with folding stiffness . . . . .	64
3.6	Concluding remarks . . . . .	66
<b>4</b>	<b>Tunable Mechanics of the Multi-stable Corrugated Tube with Conical Kresling Pattern</b>	<b>68</b>
4.1	Introduction . . . . .	68
4.2	Geometry, global multi-stability, and numerical model . . . . .	70
4.2.1	Geometry definition . . . . .	71
4.2.2	Different types of multi-stability . . . . .	71
4.2.3	Numerical model and predictions . . . . .	74
4.2.4	Stiffness of the bar and hinge model . . . . .	75
4.3	The pop-up deformation . . . . .	80
4.3.1	Pop-up and the resulting shape change . . . . .	80
4.3.2	Tunable deformation . . . . .	84
4.4	Tunable stiffness . . . . .	86
4.4.1	Tunable axial stiffness . . . . .	86
4.4.2	Tunable bending stiffness . . . . .	89
4.4.3	Sensitivity of the analyses . . . . .	91
4.5	Discussion . . . . .	94
4.5.1	Findings . . . . .	94
4.5.2	Conceptual applications . . . . .	95
4.6	Concluding remarks . . . . .	97
<b>5</b>	<b>Conclusion</b> . . . . .	<b>99</b>
5.1	Contributions and impacts . . . . .	99
5.2	Suggestions for future work . . . . .	101
5.2.1	Continuing work from the thesis . . . . .	101
5.2.2	Long-term future work . . . . .	102
<b>BIBLIOGRAPHY</b>		<b>106</b>

## LIST OF FIGURES

### FIGURE

1.1	Origami-inspired morphable structures at multiple scales and in different disciplines. (A) Deployable sandwich surfaces [23]. (B) Origami solar panel in its folded state (on the top) and deployed state (on the bottom) [24]. (C) An accordion shelter [25]. (D) Interlocking cellular assemblages of origami tubes [3]. (E) Rotorcraft protec- tor based on modified Miura-ori pattern [26]. (F) and (G) Micrometer-scale active origami structures [27,28]. . . . .	2
1.2	Properties and applications of origami tubes. (A) A deployable traffic cone and (B) vase [29]. (C) Switching between two modes by reconfiguring the Yoshimura tube cross-section [30]. (D) A deployable metamaterial based on the Miura-ori pat- tern [31]. (E) A corrugated tube becomes curved after pressurization [21]. (F) Pro- grammable stiffness of the Kresling tower [8]. (G) Axial energy-absorbing test of an origami tube [32]. (H) A crawler [33] and (I) a robotic arm based on the Kresling origami [22]. (J) An inflatable arch in its flat and deployed stable states [34]. (K) A transformable wheel [35]. . . . .	4
1.3	Buckling-induced mechanics and applications. (A) A Venus flytrap in its open and closed states [37]. (B) An inflatable jumper by shell snapping [38]. (C) A planar origami pattern is snapped into a 3D soccer shape [39]. (D) Typical load-displacement curves of axially compressing prismatic tubes and origami tubes. (E) The load- displacement curve of a bi-stable origami tube. (F) A corrugated origami tube in its two stable states: deployed and bent. (G) The Kresling module can be popped up into a much stiffer, dome-like shape. (H) A Kresling module will typically be elongated due to inflation. By buckling a single valley crease, a Kresling module can bend after inflation [40]. . . . .	6
1.4	Some common designs of origami tubes. From left to right: zipper-coupled origami tube [45], bendy straw [46], conical Kresling tube, cylindrical Kresling tower [8], Yoshimura tube [5], and waterbomb tube [47]. . . . .	7

2.1	Conceptual force-displacement curves of different energy-absorbing tubes. (A) A prismatic tube has a high peak force for crushing ( $P_{\max}$ ) with the total absorbed energy represented by the area underneath the curve ( $\approx \delta \cdot P_m$ ). (B) Introducing origami patterns in the design can reduce the peak force while increasing the total energy absorbed [36]. (C) The proposed origami tubes here could deploy to increase the crushing distance $\delta$ while remaining stowed prior to use. The increased crushing distance could allow for more energy absorption than a passive system with comparable peak forces. (D) Deployment of the proposed tubes can tune the initial stiffness, the peak forces and the total absorbed energy. . . . .	13
2.2	Geometry, fabrication, and locking. (A) A unit cell of the Miura-ori pattern is defined by: side lengths $a, c$ , vertex angle $\alpha$ , and folding angle $\theta$ . (B) Zipper-tubes at 30% and 90% extension with one segment indicated. (C) Fabrication process of locked zipper tubes. Paper tubes are shown on the left for visual clarity, and a final tube made from polyester sheets is shown on the right. (D) Comparison of load bearing capacity between unlocked (left) and locked (right) zipper tubes. Locking restricts the kinematic motion and makes the structure significantly stiffer. (E) Axial loading response in quasi-static experiments for locked and unlocked tubes. The locked structure ultimately crushes resulting in the nonlinear response. . . . .	15
2.3	Finite element model. (A) The zoom-in figure on top shows the details of the connections between adjacent panels. Finite element model of the locked zipper tubes on the bottom is only representative and a finer mesh is used for the analyses. (B) Axial force-displacement simulation for locked zipper tube with different length scale parameters $L^*$ . . . . .	16
2.4	Experimental methods. (A) A locked zipper tube in a quasi-static test. (B) The drop test frame. (C) Two laser pointers at the tops of the tubes allow for accurate tracking of the position with a high-speed camera. . . . .	18
2.5	Preliminary tests. (A) Stress-strain relationship of polyester under different loading rates. (B) Force-displacement response of polyester sheet connected with adhesive to an acrylic plate. (C) Force-displacement response of two polyester sheets connected by adhesive. . . . .	21
2.6	Laser tracking process. (A) Sketch of the side view of the test setup and diagram of the error analysis of the distance measurement. (B) A representative frame shot by the high-speed camera during the drop test. The two white spots corresponding to two laser pointers attached to the top of zipper tubes and tracking points are selected as the centroids of the spots. (C) Illustration of pixel coordinates: the pixel x coordinate of the $i^{\text{th}}$ grid shown in the figure is five, the $j^{\text{th}}$ grid is eight. (D) Time history of displacement: raw data and processed data for zipper tubes at 95% extension and 52% extension. . . . .	24

2.7	Quasi-static axial loading response of locked tubes. (A) Load-unload cycle response of tubes extended to 52%, 72%, and 95% (top) and corresponding experimental photos for the 95% and 52% extensions (bottom). The shaded area is the dissipated energy during a load-unload cycle. (B) Mean value of loading responses from seven experiments for each extension. (C) Mean value of energy absorption from seven experiments for each extension. (D) Comparison of mean force between experimental testing and numerical FEM simulation (for a crushing distance $\delta/l_c = 50\%$ ). (E) Comparison of absorbed energy between experimental testing and numerical FEM simulation (for a crushing distance $\delta/l_c = 50\%$ ). . . . .	25
2.8	Comparison of the energy absorption behavior between prismatic tubes and locked zipper tubes of the same length. (A) Experimental photos of prismatic square tubes, the numbering corresponds to part (B). (B) Mean value of loading responses from seven experiments for prismatic tubes and locked zipper tubes at 95% extension. . . . .	27
2.9	Comparison of the energy absorption behavior between zipper tubes that are locked on both ends and zipper tubes that are restrained only on the bottom end. Comparison of mean force for (A) different extensions, and (B) different number of segments, while the extension is set to be 82%. The crushing distance $\delta/L_c = 50\%$ . Plastic deformation for (C) the bottom-restrained and (D) the fully-locked tubes with different number of segments deployed to 82% extension (PEEQ is plotted on the undeformed shape). . . . .	29
2.10	Parametric variation of tube geometry. (A) Energy absorption and (B) maximum force for tubes with different number of segments. (C) Plastic deformation for two tubes with a different number of segments (PEEQ is plotted on the undeformed shape). Distributed panel plastification is observed for tubes with only two segments, whereas most plastic deformation occurs around fold lines for tubes with ten segments. (D) Energy absorption and (E) maximum force for tubes with different vertex angles. (F) Plastic deformation for tubes with different vertex angles deployed to 95% extension (PEEQ is plotted on the undeformed shape). Distributed panel plastification is observed for tubes with a vertex angle of $\alpha = 75^\circ$ , whereas most plastic deformation happens around fold lines for tubes with a vertex angle of $\alpha = 35^\circ$ . (G) Energy absorption and (H) maximum force for tubes with different aspect ratios. (I) Plastic deformation for tubes with different aspect ratios deployed to 95% extension (PEEQ is plotted on the undeformed shape). Distributed panel plastification is observed for tubes with an aspect ratio of $a/c = 2$ , whereas most plastic deformation happens around fold lines for tubes with an aspect ratio of $a/c = 0.5$ . . . . .	31
2.11	Drop tests demonstrating peak accelerations in a low-energy impact scenario. (A) Time history of acceleration for tubes with an extension of 52% and (B) tubes with an extension of 95%. (C) The peak accelerations after collision versus drop heights. The 90% confidence intervals are indicated with vertical bars and are derived from four repeated tests. . . . .	34

2.12 Self-locking of the zipper-coupled tube. (A) A tube at 72% extension is deployed to 95% extension by squeezing the sides. Panels on the ends are locked into one-way inclined ridges that are bonded onto the rigid plates. The lock edge is parallel to the glued edge. (B) Corresponding experimental photos of the deployment and locking. The tube is: 1) at the initial state; 2) deployed and locked at around 70% extension; 3) deployed and locked at around 90% extension, and a mass of 500g is supported on the top; 4) retracted to the initial state by releasing the locking ridges from the tube edge. The inserts show the locking ridges at the initial state (1) and a deployed state (3). See Movie S4. . . . .	36
3.1 Geometry and cross-sections of the corrugated straw. (A) A straw with ten unit cells. (B) A unit cell in three configurations: extended, collapsed, and bent. (C) The longitudinal section can be defined by five independent parameters. (D) Circular cross-section. (E) The track shape with $d/r = 1.1$ (F) The dumbbell shape with $d/r = 1.1$ , $\lambda_\varphi = 1.8$ . (G) The three-leaf clover shape with $\lambda_\varphi = 1.8$ . . . . .	41
3.2 The bar and hinge model and calibration. (A) Decomposition of the bar and hinge model, where the aspect ratio $\alpha = H/W$ defines the density of the mesh. (B) One triangular panel with bars (top), and the isometric view of a typical bending hinge that is connected to two triangular panels. (C) Four-point bending setup and a typical deformed state. (D) The finite element (FE) model consists of shell elements and connector elements. (E) A typical bi-stable energy profile when the energy of the crease folding is not considered. The energy barrier is denoted by $E_b$ , and the stable rotation is $\phi_b$ . (F) Comparison of energy barriers and (G) the stable rotation states between the FE model and the calibrated bar and hinge model. (H) Stability predictions for twenty five combinations of $\theta_1$ and $t/R$ . The FE predictions are slightly different from the predictions with bar and hinge model, but both models show the same trends. . . . .	46
3.3 Boundary effects of the four-point bending simulation. (A) Four-point bending setup of a corrugated tube with $N = 4$ unit cells. (B) A typical deformed state and the corresponding moment diagram. The corrugated part is strained by a nearly flat moment stage, where the center moment is of magnitude $M$ . (C) As the tube rotates, the moment $M$ will fluctuate to the negative region only for bi/multi-stable cases. The first peak $M_p$ is selected to explore convergence of the behavior with respect to the number of units. (D) Relative errors of $M_p$ between tubes with $N$ units and a tube with ten units. For four tube geometries with $N = 2$ , the relative errors are less than 3% (the insert). (E) Stability predictions for corrugated tubes of $N = 10$ unit cells. The predictions is nearly identical to those with $N = 2$ unit cells, and both show the same trends. . . . .	50

3.4	Effects of frustum slant angle $\theta_1$ , shell thickness, and crease stiffness on the bending stability. (A) Energy profiles with different combinations of the above three parameters. The first three cases have zero crease stiffness, while the crease stiffness of case 4 is defined by $L^*/R = 30$ . (B) Energy redistributions from the peak point to the valley point of the stretching energy curve. The redistribution is presented by plotting the change of energy in bars and bending hinges. The sheet thicknesses are $t/R = 0.0175$ . The color scale indicates the magnitude of energy change, and the compressive side of the straw is shown. (C) The stability map for twenty five cases of varied thicknesses and slant angles, with zero-stiffness folding hinges. Each grid shows the stability type with different colors for the corresponding case. (D) An expanded stability map with various crease stiffness defined by Eq. 3.5, where the transition boundaries of tubes with $L^*/R = \infty, 30, 3$ are marked with dashed lines. . . . .	51
3.5	Four-bar linkage model that can capture key geometric influences on bending stability. (A) The linkage model in its original configuration, and the bent state via partial inversion of cranks. (B) A typical bi-stable energy profile, where the slant angle is $\theta_1 = 30^\circ$ and $t/R = 0.0145$ . (C) Stability map that captures the trend that bi-stable bending is possible with lower thickness or higher slant angle. (D) Energy during the inversion of the left (or compressive) side of the mechanism dominates the total strain energy. S indicates the stretching of the translational springs while B indicates bending of the rotational springs. (E) Bi-stable configurations $\psi_b$ and (F) Energy barriers $\bar{E}_b$ both increase with $\theta_1$ , and only experience a minor influence from the thickness. These trends are consistent with those of the bar and hinge, and FE models. . . . .	53
3.6	Orthotropic bending stabilities of the track shape. (A) Isotropic bending with circular cross-sections turns into orthotropic bending about the strong and weak axis with the track shape. (B) The stability map of the track shape with $d/r = 0.18$ and (C) $d/r = 0.75$ . The top row corresponds to the strong-axis bending, and the bottom row corresponds to the weak-axis bending. Transition boundary of the circular cross-section from mono-stable domain to the bi-stable domain is marked with dashed lines. (D) As the distance $d$ increases, the energy barrier $E_b$ decreases in both bending directions; the second stable state $\phi_b$ of the weak-axis bending stays roughly the same, whereas that of the strong-axis bending is decreased. . . . .	57
3.7	Bending stabilities for cross-sections that have negative curvature. (A) The strong-axis and weak-axis bending with the dumbbell shape. (B) The stability map of the dumbbell shape with $\lambda_\varphi = 2.5$ and (C) $\lambda_\varphi = 1.5$ . Transition boundary of the track shape of the same distance $d$ is marked with dashed lines. (D) The dumbbell shape morphs to the track shape as the controlling parameter $\lambda_\varphi$ increases towards $\infty$ . For both bending directions, energy barriers $E_b$ decrease during the process, and the stable rotation $\phi_b$ stays at the same level. . . . .	58

3.8	Redistributions of stretching (top row) and bending energy (bottom row) from the peak point to the valley point of the stretching energy curve. From the left to the right: strong-axis bending of the track shape, weak-axis bending of the track shape, and strong-axis bending of the dumbbell shape. The outer radius $R$ is fixed to be 31 mm, and the other parameters are: $d/r = 0.75$ , $\theta_1 = 20^\circ$ , $t/R = 0.019$ , and $\lambda_\varphi = 1.5$ . The color scale indicates the magnitude of the energy change. The limits of the color scale of the bending energy are trimmed to be the same as the stretching energy, and any magnitude that exceeds the range is plotted using the threshold color. The energy is shown for exaggerated bar and hinge elements, with elements near zero energy staying hidden. . . . .	60
3.9	Energy behavior of bending the orthotropic cross-sections in different directions. (A) The track-shape cross-section and (B) the dumbbell-shape cross-section are bent along all the directions in the XY-plane. (C) Energy landscapes of the track shape and (D) the dumbbell shape, where the distance from the centroid represents rotation $\phi$ . Four local minima of energy are marked with pentagrams, and the rotations at which the peak energy is achieved are denoted with the green dashed lines. (E) Strain energy magnitude for the track shape and (F) the dumbbell shape at specific rotations: $\phi = 1^\circ, 1.5^\circ$ , and the peak and valley of the directional energy profiles. The peak energy is nearly-identical for all directions, while valley energies show four local minima. . . . .	61
3.10	Energy behaviors and stabilities of the clover cross-section. (A) The two-units structure with cross-sections of the clover shape is bent along all directions in the XY-plane. (B) Energy landscape has six local minima and they are marked with pentagrams. Peak-energy rotations are denoted with the dashed line. (C) Strain energy magnitude at specific rotations: $\phi = 1.2^\circ, 1.8^\circ$ , and the peak and the valley of directional energy profiles. (D) Stability map for the clover shape with $\lambda_\varphi = 1.5$ and different $d/r$ ratios, when bending along two unique stable directions $0^\circ$ , (E) $180^\circ$ , and (F) the unstable direction $90^\circ$ . . . . .	63
3.11	Physical models with non-zero folding stiffness and simulated results of the bar and hinge model with $L^*/R = 3$ . (A) The paper model with circular cross-sections can stay at the bent state. (B) The model with the track-shape cross-sections bent about the weak-axis and (C) the strong-axis. The weak-axis bending is mono-stable while the strong-axis bending stays at the second stable configuration. Their stabilities are predicted correctly using the same stiffness parameter as the circular case. . . . .	65
4.1	Geometry of the Kresling cone and the corrugated tube. (A) A multi-stable straw in its three stable states. (B) An origami unit can be decomposed into Kresling frusta, for which the geometry can be described by the planar views. (C) A Kresling corrugated tube in its extended, bent, and collapsed states, illustrated by computer models (top row) and paper prototypes (bottom row). The two angles are $\theta_1 = 30^\circ$ , $\tau = 0^\circ$ (top frusta) and $\theta_1 = 70^\circ$ , $\tau = 0^\circ$ (bottom frusta) (D) Three stable states of the Kresling frustum ( $\theta_1 = 65^\circ$ , $\tau = 50^\circ$ ) shown by computer models (top row) and paper prototypes (bottom row). (E) Three components of the bar and hinge model shown on the single frustum. (F) The numerical predictions of stability for different geometry of the Kresling tube. (G) A ten-frusta corrugated tube showing three types of stable states ( $\theta_1 = 65^\circ$ , $\tau = 50^\circ$ ). . . . .	73

4.2	Stiffness definition of the bar and hinge model. (A) A frustum is discretized into bars and hinges. (B) The in-plane bars and the area definition. (C) The hinges for capturing the out-of-plane bending of the panels. (D) The hinges for representing the folding of the creases. . . . .	77
4.3	Comparison of the numerical predictions between the finite-element (FE) model and the bar and hinge model. In-plane deformations of triangular panels are simulated as stretching and shearing using the bar and hinge model (A, D) and the FE model (B, E), respectively. The normalized stiffness of stretching and shearing are shown in (C) and (F) for triangles of various shapes. (G) Finite-element model of the Kresling frustum shown with a representative sketch of the meshing scheme, while a finer mesh is used for the actual analyses. The zoom-in plot shows the details of the connections between adjacent panels. (H) Predictions of the axial stiffness of the frustum with the bar and hinge model and the FE model. (I) A sample bi-stable axial loading response of the frustum, where the critical force and the corresponding axial displacement are denoted by $P_{cr}$ and $\Delta_{cr}$ , respectively. (J) Predictions of $P_{cr}$ and $\Delta_{cr}$ with the bar and hinge model and the FE model. . . . .	79
4.4	Pop-through of valley creases converts the cone to a dome-like shape. (A) A paper cone in its initial state (i) and pop-up state (ii). The zoom-in photo (iii) shows the panel curvature after pop-up. (B) By placing a node on the valley crease, the pop-up process can be simulated by the bar and hinge model. (C) The energy landscape of a bi-stable pop-up process. (D) The bar strains experienced during the pop-up process. (E) The energy distribution at the pop-up state. The folding, stretching, and bending energy plots are counterclockwise arranged. (F) Left: Numerical predictions of the pop-up stability with respect to the geometric parameters and the sheet thickness; Right: underlying energy behaviors of two mono-stable cases. (G) Shape change from the initial state to the pop-up state, including the enclosed volume (Left), the twisting angle (Middle), and the slant angle (Right). . . . .	83
4.5	Pop-through of valley creases enables the switching of deformation modes. (A) Under vertical loading, many Kresling frusta geometries are mono-stable and collapse via a twisting motion from their initial states. However, they can also be axially inverted after experiencing a pop-up deformation. (B) The axial mode switch demonstrated with a paper prototype. (C) By pop-through of only one crease, the Kresling frustum reaches a tilted state, which allows for continuously-changing orientations and bending-like multi-stability over the tube length, as shown in (D). . . . .	85
4.6	The conical Kresling has a tunable axial stiffness. (A) The paper frustum can be collapsed by a thin plastic panel when it is in the initial state, but can support three calibration weights of 1.5 kg when in a pop-up state. (B) The simulation setup using the bar and hinge model. (C) Numerical predictions of the axial force-displacement ( $\Delta$ ) curves of the initial frustum and the pop-up frustum show that the structure stiffer by more than ten thousand times. (D) The change of energy in different bending, folding, and stretching elements during the vertical loading for the initial frustum and (E) the pop-up frustum. (F) The ratio of the pop-up stiffness to the initial stiffness for different geometric parameters. . . . .	87

4.7	The tunable axial stiffness is verified by experimental tests. (A) A paper frustum being quasi-statically compressed in its initial state (top) and pop-up state (bottom). (B) The axial loading responses of paper frusta with four geometries. The solid lines are the averaged responses, and the shaded region denote the range of experimental data. The dashed lines denote the bar and hinge predictions when the Young's modulus equals to 3.5 GPa. (C) Comparison of the stiffness ratio between the bar and hinge model and the experimental results. The bars show one standard error for seven tests. . . . .	89
4.8	Multi-stability of twisting and pop-up leads to tunable bending stiffness of the Kresling corrugated tube. (A) Deformation eigenmodes that correspond to the global bending of the twelve-frustum tube at its twisted state (top), initial state (middle), and pop-up state (bottom). (B) The normalized bending eigenvalue ( $\bar{\lambda}$ ) vs. the initial twisting angle for the three stable states. (C) Deformation of the corrugated tube when used as cantilevers at different stable configurations. The left end is fixed, and a uniform load is applied on the right end. The deformed shapes are scaled so the maximum displacement for each case is equal to the difference of the inner and the outer radius. (D) The equivalent section modulus ( $\text{mm}^4$ ) based on the cantilever test for loads in the X-Y plane represented as a polar plot at the three stable states, respectively. Here, the outer radius $R$ is set to be 31 mm, and the section modulus is shown as distance from origin. . . . .	91
4.9	Sensitivity of the axial stiffness tuning with respect to the crease stiffness. . . . .	92
4.10	Reinforcing the ends of the tube prevents localized deformation modes but does not lead to a significant change in the bending eigenvalues. The deformation modes of global bending, as well as the normalized eigenvalues, are shown for tubes with (A) reinforced ends and (B) unreinforced ends. For the reinforced cases, the end frusta will not be popped or axially compressed. All eigenvalues are normalized by the maximum eigenvalue of the reinforced tube within the range of $\tau \in [35^\circ, 55^\circ]$ . . . . .	93
4.11	The estimated equivalent section modulus converges with the number of frusta. A tube with twenty frusta is used as a point of comparison to find the relative error. For the cantilever tests that are presented in Fig. 4.8, the relative errors are below 1%. . . . .	94
4.12	Conceptual applications of Kresling corrugated tubes. (A) Tunable and deployable energy absorption system. The axial loading response is shown for the initial and pop-up frustum states, with the corresponding Von Mises stresses at the final crushed states. (B) Kresling frusta with decreasing radii are axially stacked to construct a deployable traffic cone that allows compact storage. (C) The different frusta of a reconfigurable robotic arm, can deform between the compliant mode and the stiff joint-link mode. . . . .	97
5.1	Program the tunability in (A) multi-stable origami and (B) rigid-foldable origami with internal pressure. . . . .	103
5.2	The zoom-in view of a meter-scale origami tube assembled by connecting corrugated panels with piano hinges (tube courtesy: Anna Jia and Yi Zhu). . . . .	105

## **LIST OF TABLES**

### TABLE

2.1	The ratio of the amount of energy absorbed at 95% extension to the corresponding peak force ( $\delta \cdot P_m / P_{\max}$ ). . . . .	32
3.1	Geometric parameters of the corrugated tube . . . . .	44

## ABSTRACT

Thin-walled origami-inspired tubes can be used as lightweight systems for various functional applications in engineering. Folding motions can allow for deployment, reconfiguration, and compact storage of the systems, while buckling of the thin walls can be used to tune the system properties or achieve secondary functions such as energy absorption. This thesis aims to explore the stability of morphing tubes and harness buckling for functional applications.

The dissertation first explores a deployable design where origami tubes extend, lock, and absorb energy through crushing (buckling and plasticity). Numerical and experimental studies investigate the tunable stiffness and energy absorption behaviors of these systems under static and dynamic scenarios. The stiffness, peak crushing force, and total energy absorption of these origami tubes can be changed through reconfiguration. These deployable systems can increase the crushing distance between impacting bodies and can allow for on-demand energy absorption characteristics.

Next, the bending stability that allows for morphing in corrugated tubes is explored (bending in drinking straws). Finite element models and a reduced-order elastic simulation package can capture the nonlinear multi-stable behaviors. Modified cross-sections for the corrugated tubes are introduced and explored to identify how geometry affects bending stability, energy barriers, and stable configurations. Results show that thinner shells, steeper cones, and weaker creases are required to achieve bending bi-stability.

A bar and hinge simulation model is then used to identify and capture a unique pop-up mechanism in Kresling origami that enables shape-morphing and stiffness tuning. By buckling the valley creases, the conical Kresling will pop into a dome-like shape and the crease network will be distorted. As a result, the flexible twisting motion via crease folding is prohibited, and the cone stiffness can be increased by up-to-four orders of magnitude. Parametric studies revealed that a shallower and more twisted Kresling unit will have more significant stiffness tuning. Experimental tests were used to verify the numerical predictions of tunable stiffness.

This thesis explores how buckling in thin-walled origami tubes can be harnessed for functional purposes. The mechanics of three different tubular designs are explored to give insight on how geometry, sheet thickness, and material properties affect the buckling and multi-stable behaviors. These findings can inform future designs of tubular origami for shape-morphing and other functional uses.

# CHAPTER 1

## Introduction

Origami, the ancient art of folding thin sheets, provides an efficient method to build 3D systems from planar sheets with predefined patterns of creases. People may have adopted the idea from nature, as some flying animals [1] are equipped with folding mechanisms to pack their wings when relaxing, and to deploy them when flying. These natural instances are unlikely to be deliberately designed, but they reveal the core functionality brought by creases. Through concentrated local rotations around crease lines, the origami systems can undergo substantial change of shape, enabling deployable and reconfigurable designs with properties that are otherwise not achievable through conventional structures.

Recently, origami principles have gone far beyond artwork and have stepped into various engineering fields, including structures that can be deployed to achieve complex functions [2,3,4,5,6,7], metamaterials that are benefitted by the morphing potentials [8,9,10,11,12,13], and new fabrication techniques [14, 15, 16, 17, 18]. Many applications come from the morphing potential of origami, and in particular, origami-inspired tubular structures have gained increasing interests [2,19,20,21]. Tubular structures with creases can either be deployed through kinematic foldings, or by snap-through instabilities that involve panel deformations. Those deployable tubes have been utilized for versatile applications, such as tunable stiffness [8], achieving gripping motions [21], reconfigurable robotic arms [22], and energy absorptions [20]. Our work in this thesis focuses on the tubular origami structures, exploring associated tunable properties and applications, as well as the geometric influences.

The following sections of this chapter are organized as follows. Section 1.1 will give a brief overview of multi-scale morphable structures in different disciplines. Section 1.2 narrows the scope from general morphing structures to a specific category: deployable tubes. In this section, we will review the common designs of origami tubes, their novel properties and associated applications, and the perspectives from which buckling can be utilized. Section 1.3 summarizes the highlights of the thesis work that will be presented in the following chapters.

## 1.1 A brief overview of origami-inspired morphable structures

Origami principles have been applied in various engineering disciplines by utilizing their morphing potential. The morphable structures can be deployed and compactly stowed to save storage space, without sacrificing the complexity of functionalities. Moreover, deployability and reconfigurability enable designs of meta-systems, in which geometries and properties can be adaptable and programmable. These designs and systems can be found in drastically different scales from micrometer to infrastructure scale, and some of the representative applications are shown in Fig. 1.1.

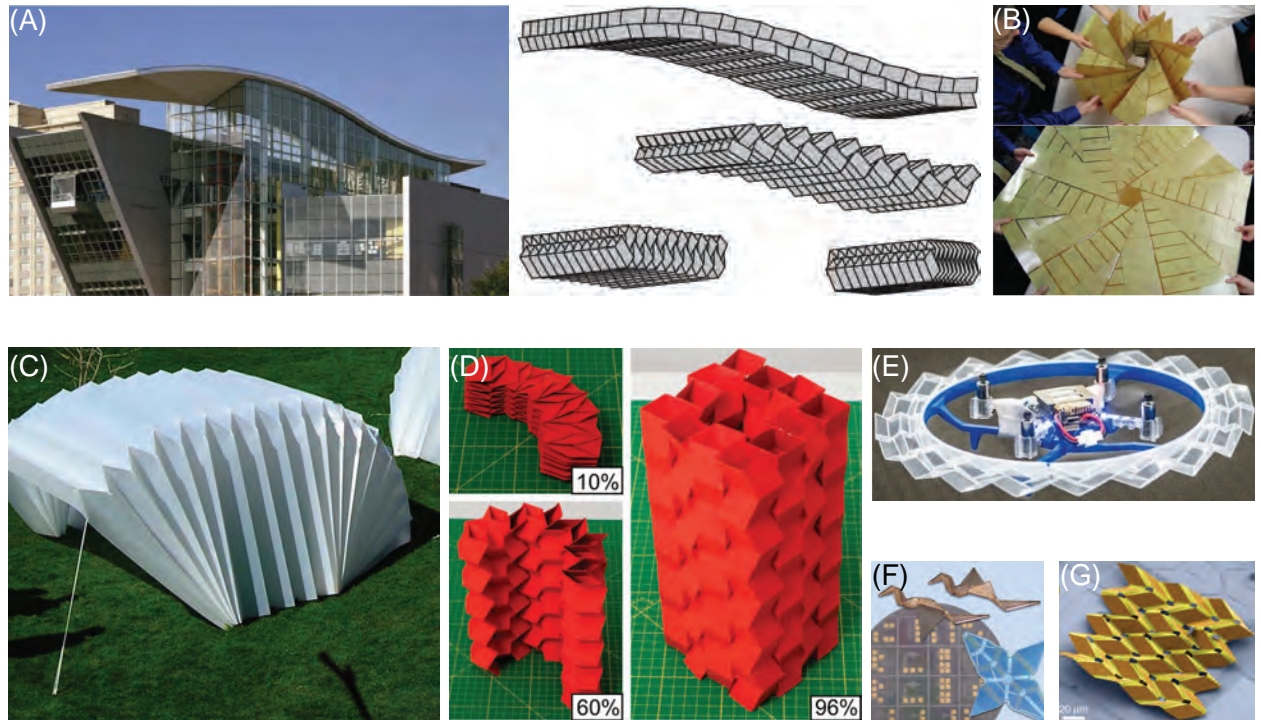


Figure 1.1: Origami-inspired morphable structures at multiple scales and in different disciplines. (A) Deployable sandwich surfaces [23]. (B) Origami solar panel in its folded state (on the top) and deployed state (on the bottom) [24]. (C) An accordion shelter [25]. (D) Interlocking cellular assemblages of origami tubes [3]. (E) Rotorcraft protector based on modified Miura-ori pattern [26]. (F) and (G) Micrometer-scale active origami structures [27, 28].

At structural-engineering scales, origami-inspired structures provide deployable solutions for creating building components such as canopies (Fig. 1.1A). The smooth functional surfaces maintain a high out-of-plane stiffness during and after deployment. At human scales, origami patterns can be designed into thin-shell structures to create deployable surface systems, which can be rapidly deployed to enable optimal solar insulation (Fig. 1.1B). A similar strategy has also been

used to manufacture accordion shelters that are easy to transport when stowed and adaptable to various environments when deployed (Fig. 1.1C).

At decimeter scales, origami morphable structures offer efficient methods for creating structures of which the mechanical properties can be tuned. Cellular assemblages of pre-folded thin sheets can be deployed and interlocked into a stiff conforming shape during the deployment (Fig. 1.1D). The popular Miura-ori pattern is employed to develop a free-to-spin protector for rotorcraft to reduce the impact forces of collision (Fig. 1.1E). At micro scales, origami patterns can be cut into planar systems to create 3D active structures, which are otherwise difficult to build through traditional methods. Photolithography-based methods have been used to create micro-origami that are suitable for creating medical devices and micro-robots (Fig. 1.1F, G).

## 1.2 Origami-inspired tubular structures

### 1.2.1 Origami-inspired tube applications

Among various forms of morphable structures, the deployable tubular structure is a specific group that shares a similar shape to thin-walled tubes, yet can deform via concentrated deformations of crease lines. Based on the morphing potential and tubular form, there are three main benefits from engineering perspective:

**The first benefit** is inherited from morphable structures: *these tubes are deployable and reconfigurable*. As a specific category of deployable structures, they can be compactly stowed to save space, and rapidly deployed to certain functional shapes (Fig. 1.2A, B). Typically, these tubes have only one flexible mode (longitudinal deployment) through which they can deform without bending or stretching of panels. The limitation of deployment motion could be a drawback in some situations, but it also facilitates the tubular system advantages for suitable applications. With the simple actuation only on one end, the zipper-coupled tube can be deployed along its longitudinal direction while maintaining stiffness for other directional loads [3]. There also exist some tubular designs that can be reconfigured along other directions. For instance, the Yoshimura tube can be transformed from the load-bearing mode to a flexible mode by reconfiguring the cross-section (Fig. 1.2C). Moreover, origami tubes can be further assembled into deployable metamaterials (Fig. 1.2D).

**The second benefit** comes from *the continuity of the structure envelope*. By carefully sealing both ends, the deployable tubes are airtight, and thus can be pneumatically actuated to achieve complex tasks, and acquire distinct mechanical properties. Based on the corrugated tubes, du Pasquier et al. proposed a pneumatic toolkit that can achieve bending and extending motions (Fig. 1.2E). Internal pressure can also change the energy landscape of deployable tubes and enable more

stable states [19].

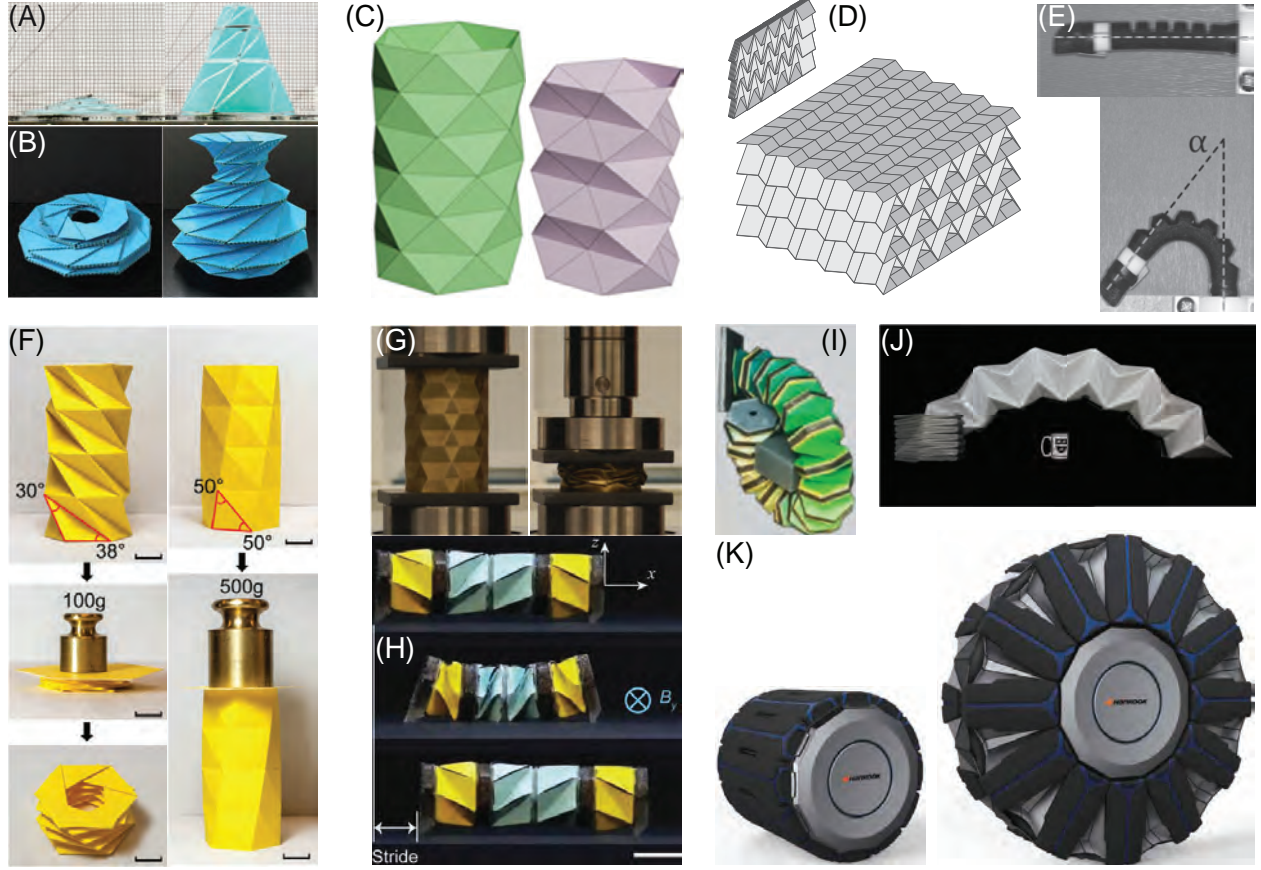


Figure 1.2: Properties and applications of origami tubes. (A) A deployable traffic cone and (B) vase [29]. (C) Switching between two modes by reconfiguring the Yoshimura tube cross-section [30]. (D) A deployable metamaterial based on the Miura-ori pattern [31]. (E) A corrugated tube becomes curved after pressurization [21]. (F) Programmable stiffness of the Kresling tower [8]. (G) Axial energy-absorbing test of an origami tube [32]. (H) A crawler [33] and (I) a robotic arm based on the Kresling origami [22]. (J) An inflatable arch in its flat and deployed stable states [34]. (K) A transformable wheel [35].

**The third benefit** is the *programmability facilitated by the large design space*. The programmability is reflected in the way that mechanical properties can be drastically tailored by changing the design parameters. Stiffness of the Kresling origami tube, for example, can be differed by several orders of magnitude via changing the design angles (Fig. 1.2F). In the following chapters of main results, I will present parametric studies that reveal how the design parameter can change the energy-absorbing performance, the multi-stability, and the stiffness tuning.

As empowered by these benefits, origami tubes have inspired numerous applications, in which they can either improve the performance of conventional devices or create novel functions, such as

improved energy-absorbing performance (Fig. 1.2G), complex motions of crawling and gripping (Fig. 1.2H, I), pneumatic deployment of a meter-scale arch (Fig. 1.2J), and the transformable wheel that can adapt to different terrains (Fig. 1.2K).

### 1.2.2 Buckling in origami tubes

Structural buckling, once regarded as an undesired phenomenon that causes catastrophic failures, has now emerged as a new route to create functionalities in structures and artificial materials. In nature, the doubly curved leaves of the Venus flytrap can rapidly snap to a closed state to capture insects (Fig. 1.3A). A similar snap-through process often causes a sudden release of stored elastic energy that can generate powerful motions, e.g., jumping of an inflated soft shell (Fig. 1.3B). From the static perspective, buckling of structural elements opens a route for assembling 3D structures from planar 2D surfaces, which is crucial in the field of photolithography-based fabrication (Fig. 1.3C).

In this work, I aim to create functionality in origami tubes with strategically-triggered buckling from three perspectives. For tubular energy absorbers that dissipate energy through the buckling and plastic yielding of thin shells, an ideal design should have both low peak force  $P_{\max}$  and high mean crushing force  $P_m$  (Fig. 1.3D). The peak force, defined as the largest reaction force during the axial crushing, needs to be low to reduce the possible damage that is transmitted to the protected object [36]. The mean crushing force, is the total energy absorption divided by the crushing distance  $\delta$ , needs to be high to absorb more impact energy (Fig. 1.3D). As compared to the prismatic counterpart, stamping origami patterns onto the tube surfaces will introduce geometric imperfections, which can reduce the peak force and trigger a buckling mode that is equally or more efficient in terms of energy absorption, i.e., lower  $P_{\max}$  and similar  $P_m$  (Fig. 1.3D).

Besides the improvement of plastic energy absorption, the instability can also be utilized in designing a reusable elastic mechanism that traps impact energy (Fig. 1.3E). For a bi-stable mechanism, the reaction force is first positive then negative. The difference between the energy input and output,  $E_{\text{in}} - E_{\text{out}}$ , is the amount of energy that is locked into the system.

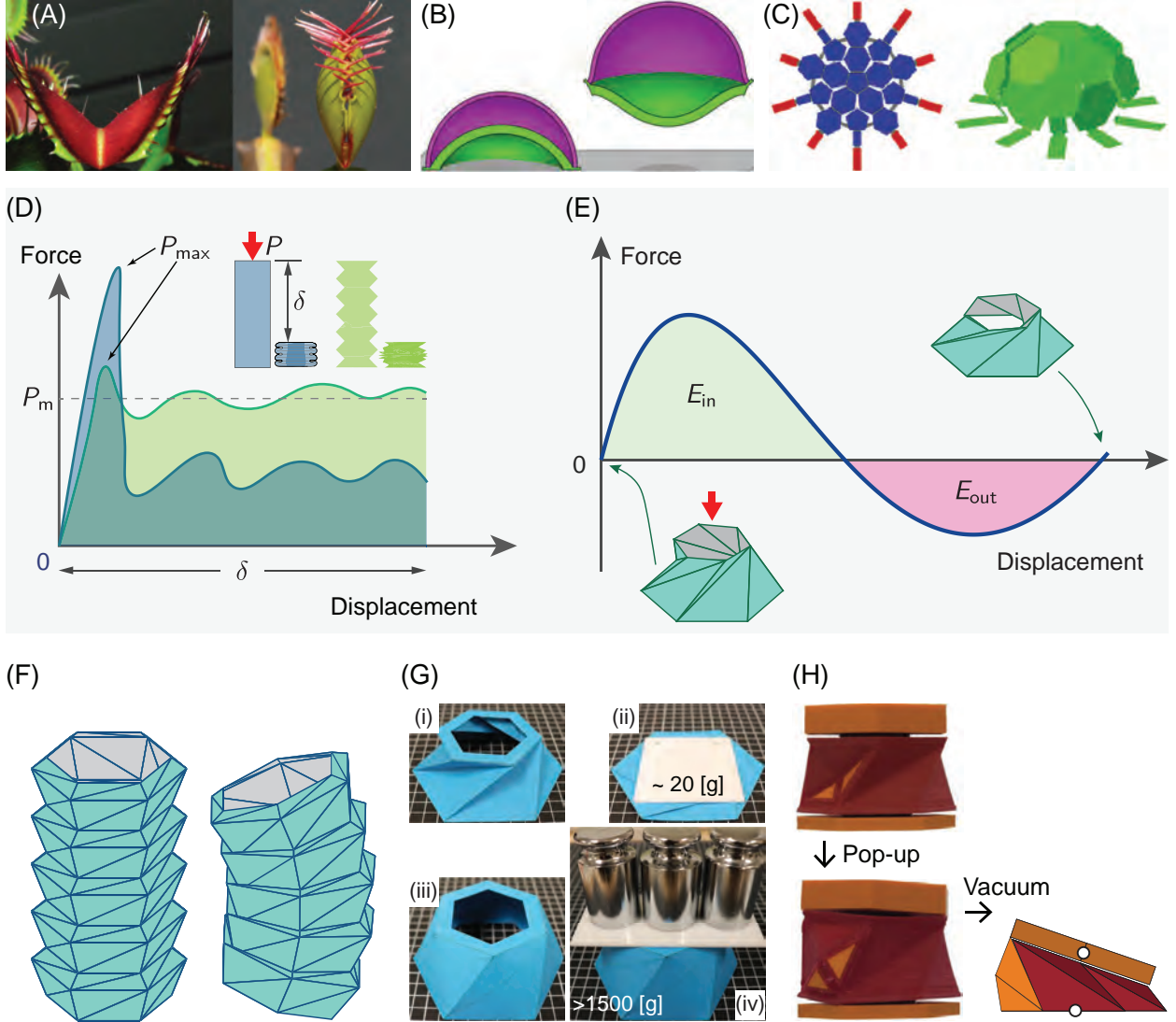


Figure 1.3: Buckling-induced mechanics and applications. (A) A Venus flytrap in its open and closed states [37]. (B) An inflatable jumper by shell snapping [38]. (C) A planar origami pattern is snapped into a 3D soccer shape [39]. (D) Typical load-displacement curves of axially compressing prismatic tubes and origami tubes. (E) The load-displacement curve of a bi-stable origami tube. (F) A corrugated origami tube in its two stable states: deployed and bent. (G) The Kresling module can be popped up into a much stiffer, dome-like shape. (H) A Kresling module will typically be elongated due to inflation. By buckling a single valley crease, a Kresling module can bend after inflation [40].

For the thin-walled origami tubes, another benefit of elastic buckling is multiple stable states. The bendy straw, for example, can morph and lock with both longitudinal and rotational deformations [41]. From the geometry perspective, a bendy straw is a corrugated tube consisting of frusta that are serially connected by creases (Fig. 1.3F). Each frustum can experience either a full

shell inversion that shortens the tube length, or a partial inversion that enables global rotation (Fig. 1.3F). Those functions allow the corrugated tube to conform to different shapes [42], and transport fluids and gases [43, 44]. The shape-morphing and multi-stable features then lead to the tunable mechanics. As an example, the Kresling cone is flexible in its original configuration, which can collapse under a plastic plate that weighs only  $\sim 20$  g (Fig. 1.4G, i to ii). Once it is popped up into a dome-like shape (i to iii), it can support more than 1500 g of weight, without showing visible deformations (iii to iv). Moreover, the crease buckling can break up the topological arrangement of crease lines, opening up different deformation modes for tubes that will otherwise only elongate or shorten under pressurization (Fig. 1.3H).

### 1.2.3 Origami-inspired tube geometries

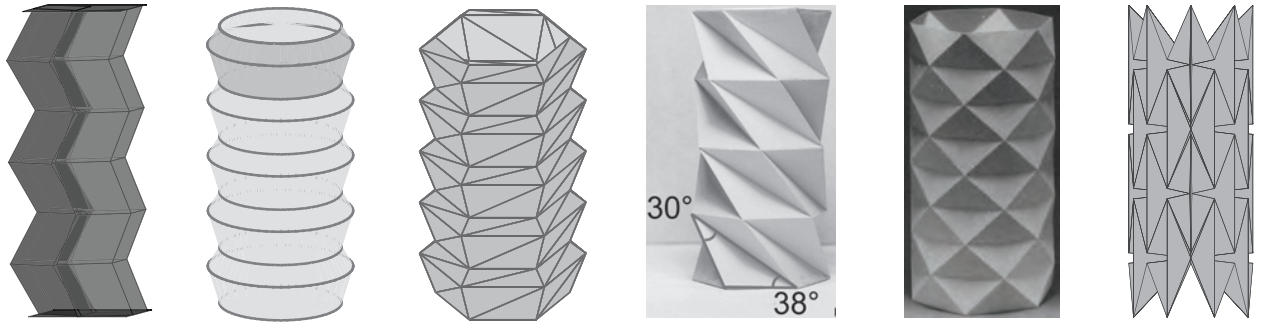


Figure 1.4: Some common designs of origami tubes. From left to right: zipper-coupled origami tube [45], bendy straw [46], conical Kresling tube, cylindrical Kresling tower [8], Yoshimura tube [5], and waterbomb tube [47].

Three different testbeds are selected for exploring the benefits of buckling in origami tubes, ranging from the well-known Miura origami to modified conical origami patterns. For the energy-absorbing improvement, I proposed a deployable energy absorber based on the zipper-coupled origami tubes (Fig. 1.4). The zipper-coupled tube is a rigid-foldable tubular mechanism that shows high bending stiffness when deployed [3]. It can be assembled to form a foldable cellular metamaterial [31] or a deployable canopy with high out-of-plane stiffness [23]. With a self-locking mechanism, the tube can be deployed to and locked at various configurations. As a result, the energy performance can be tuned for different application scenarios.

I then use the bendy straw to explore how geometry affects the local snap-through of frustum shells and the associated multi-stability of corrugated tubes. The corrugated flexible drinking straw has been used in daily life for decades [48]. Recently, it has drawn research attention for its axial and bending multi-stability, such as a reusable energy absorber [20] and a wire-like structure that

can fit arbitrary 3D shapes [42]. In this thesis, I use an elasticity-based bar and hinge model to simulate its multi-stable bending behavior. Since the model can predict accurate elastic response rapidly, I also run extensive parametric studies to explore the geometric influences.

The next tubular design investigated in this thesis is the conical Kresling tube, a generalization of the traditional Kresling tower. Typically, the Kresling tube family can transition between two axial stable configurations via a twisting motion [49]. Such axial bi-stability can be employed to build a mechanical memory device [50], or be used to design a meta-structure with tunable band frequency [51]. Recently, the Kresling tube has also received research attention for its bending properties, such a magneto robotic arm [22] and an articulated robotic arm with tunable bending stiffness [52]. In Chapter 4, I identify a new stable configuration of the Kresling tube. By buckling the valley creases outwards, a unit cell of the Kresling tube can be converted to a dome-like shape which will be substantially stiffer than the initial configuration.

Besides the above tubular designs that will be presented in the following chapters, there are other tubular designs that have received increasing research attention, such as the Yoshimura tube and the Waterbomb tube (Fig. 1.4). As comparing to the conventional energy absorbers, origami crashboxes based on the Yoshimura pattern show superior performance [53]. By squeezing the sides, the Yoshimura tube can be reconfigured to show drastically different stiffness [30]. The waterbomb tube, as a reconfigurable structure, can be used to build a transformable wheel [35], or be assembled to an earthworm-like robot [54].

### 1.3 Scope of the thesis

The main objective of this thesis is to explore the aforementioned buckling-induced functions of origami tubes. The global mechanical properties are investigated using a reduced-order bar and hinge model, the finite-element method, and with experiments. Based on the zipper-coupled tubes, I explore a deployable design concept that can be extended and locked at various lengths to tune the energy-absorbing performance. I next explore the bending stability of curved-crease origami tubes, showing the influence of geometry and tube cross-section on the system stability. Finally, I explore the conical Kresling origami tube, where the valley creases can be buckled to increase the stiffness in both the axial and bending directions. A detailed discussion of the thesis organization is as follows.

**Chapter 2** presents a deployable energy absorber that can extend, lock, and is intended to absorb energy through crushing (buckling and plasticity). Energy absorption devices are widely used to mitigate damage from collisions and impact loads. Due to the inherent uncertainty of possible impact characteristics, passive energy absorbers with fixed mechanical properties are not capable of serving in versatile application scenarios. The proposed system concept is unique be-

cause origami deployment can increase the crushing distance between two impacting bodies and can tune the energy absorption characteristics. I show that the stiffness, peak crushing force, and total energy absorption of the origami tubes all increase with the deployed state. I present numerical and experimental studies that investigate these tunable behaviors under both static and dynamic scenarios. The energy-absorbing performance of the deployed origami tubes is slightly better than conventional prismatic tubes in terms of total absorbed energy and peak force. When the origami tubes are only partially deployed, they exhibit a nearly-elastic collapse behavior, however, when they are locked in a more deployed configuration they can experience non-recoverable crushing with higher energy absorption. Parametric studies reveal that the geometric design of the tube can control the nonlinear relationship between energy absorption and deployment. A physical model shows the potential of the self-locking after deployment. This concept for deployable energy-absorbing origami tubes can enable future protective systems with on-demand properties for different impact scenarios.

**Chapter 3** investigates the geometric influence on the bending stability of corrugated tubes with curved creases. Thin-walled corrugated tubes that have a bending multistability, such as the bendy straw, allow for variable orientations over the tube length. Compared to the long history of corrugated tubes in practical applications, the mechanics of the bending stability and how it is affected by the cross-sections and other geometric parameters remain unknown. To explore the geometry-driven bending stabilities, I used several tools, including a reduced-order simulation package, a simplified linkage model, and physical prototypes. I found the bending stability of a circular two-unit corrugated tube is dependent on the longitudinal geometry and the stiffness of the crease lines that connect separate frusta. Thinner shells, steeper cones, and weaker creases are required to achieve bending bi-stability. I then explored how the bending stability changes as the cross-section becomes elongated or distorted with concavity. I found the bending bi-stability is favored by deep and convex cross-sections, while wider cross-sections with a large concavity remain mono-stable. The different geometries influence the amounts of stretching and bending energy associated with bending the tube. The stretching energy has a bi-stable profile and can allow for a stable bent configuration, but it is counteracted by the bending energy which increases monotonically. The findings from this work can enable informed design of corrugated tube systems with desired bending stability behavior.

In **Chapter 4**, I study the tunable stiffness and the multi-stability of corrugated tubes consisting of serially interconnected polygonal frusta based on Kresling origami pattern. Under appropriate geometric designs, the origami corrugated tube either has straw-like multi-stability with axial inversion and bending, or has multiple axial stable states via a twisting motion. I focus on the latter category and reveal another stable "pop-up" configuration via local buckling of the valley creases. By switching among the three types of stable configurations, the corrugated tube can exhibit dras-

tically different axial and bending stiffness. Moreover, the deformation mode can switch from twisting to inversion after the pop-up. To quantify the tunable mechanical properties, I employ an elasticity-based bar and hinge model and perform parametric studies to discover the relationship between the geometry and the mechanics. The results suggest that a higher initial twisting and a lower initial slope will provide more significant stiffness and shape tuning, and the frustum stiffness can be increased by four orders of magnitude. To validate the numerical results, I fabricate proof-of-concept origami frusta and corrugated tubes. These prototypes demonstrate the desired multi-stable behavior, the tunable stiffness, and the deformation mode switching. This design of corrugated tubes has potential applications including tunable energy absorbers, deployable traffic cones, and reconfigurable robotic arms.

**Chapter 5** summarizes the main findings and conclusions from the thesis. I also present outlooks into future studies that can push the origami tubes with structural instability towards real-world applications.

## CHAPTER 2

# Locking Zipper-coupled Origami Tubes for Deployable Energy Absorption

Origami principles can be beneficial to tubular energy absorbers from three aspects. First, an origami tubular energy absorber can be deployed to increase the crushing distance. Second, it can be reconfigured to tune its performance. Third, as compared to prismatic tubes, a tube with origami pattern will crush in a mode that is more efficient in terms of absorbing impact energy. In this chapter, we propose a deployable energy absorber based on the zipper-coupled origami tube. With zip-tie mechanisms, the system can be deployed and locked at various configurations to provide tunable energy absorption. Here, we use finite-element simulations and quasi-static tests to quantify the tunability, and we perform parametric studies to find out the optimal design under different application scenarios. This work has been published as: [Wo, Z., Raneses, J.M., and Filipov, E. T., Locking Zipper-coupled Origami Tubes for Deployable Energy Absorption, ASME. J. Mech. Rob. 14\(4\): 041007. doi:10.1115/1.4054363.](#)

## 2.1 Introduction

Conventional energy absorption systems serve as passive sacrificial structures that absorb the kinetic energy of an impact through buckling, crumpling, and plastic deformation. Thin walled prismatic tubes and cellular structures are effective in this role because they can provide a large amount of energy absorption for their small overall mass [55]. The energy absorption characteristics of such structures are typically evaluated from quasi-static compressive tests where the crushing distance ( $\delta$ ), mean crushing force ( $P_m$ ), and peak crushing force ( $P_{\max}$ ), are of primary interest (Fig. 2.1A). The total energy that can be absorbed by the system is  $\delta \cdot P_m$ , while the peak crushing force is of interest as it correlates with the forces and accelerations translated to the object that is to be protected.

One recent innovation for energy-absorbing tubes has been to use origami inspired patterns in the design and fabrication of the thin-walled structures [36]. The pre-patterned geometry triggers

controlled buckling modes during crushing, which in turn can reduce the peak forces and increase the total amount of energy absorbed (Fig. 2.1B). Origami can also offer a variety of geometric design options and can have the benefit of easy fabrication from a flat developable surface [53,56,57]. For example, a thin-walled tube with pre-folded Yoshimura pattern [32] and a sandwich-like structure with Kresling pattern [58] can both provide favorable energy-absorbing behaviors. However, all of these previous origami systems are passive, and the entire energy absorption performance is determined by the design geometry and material properties.

In this chapter, we present a concept that takes further advantage of the origami principles and uses the folding kinematics of zipper-coupled tubes [3] to enable deployment and tuning of the energy absorber. By deploying the origami, it becomes possible to initiate earlier contact between colliding objects and to increase the crushing distance ( $\delta$ ) of the system. The longer crushing distance allows for an increase in the amount of absorbed energy if we assume that forces would be in the same range (Fig. 2.1C). Additionally, a deployable energy absorber could be stowed compactly prior to impact in order to save onboard space or improve the aerodynamics in vehicle applications.

Deployment of the origami tubes also enables tunable performance of the energy absorber as shown conceptually in Fig. 2.1D. The proposed structures have the potential to deploy, lock, and crush at different geometric states where each state offers drastically different force-displacement characteristics. Our results, presented later in the chapter, show that the crushing distance ( $\delta$ ), mean crushing force ( $P_m$ ), and peak crushing force ( $P_{\max}$ ), can all be increased by elongating the origami tubes. Depending on the mass and velocity of an impacting object, the energy absorber could be deployed to minimize the peak force and absorb only the desired amount of kinetic energy (Fig. 2.1D).

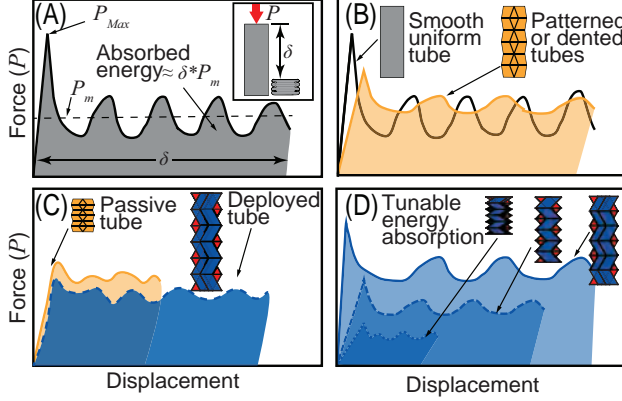


Figure 2.1: Conceptual force-displacement curves of different energy-absorbing tubes. (A) A prismatic tube has a high peak force for crushing ( $P_{max}$ ) with the total absorbed energy represented by the area underneath the curve ( $\approx \delta \cdot P_m$ ). (B) Introducing origami patterns in the design can reduce the peak force while increasing the total energy absorbed [36]. (C) The proposed origami tubes here could deploy to increase the crushing distance  $\delta$  while remaining stowed prior to use. The increased crushing distance could allow for more energy absorption than a passive system with comparable peak forces. (D) Deployment of the proposed tubes can tune the initial stiffness, the peak forces and the total absorbed energy.

The deployable origami structures explored in this chapter share similarities with other energy-absorber designs in the emerging field of mechanical metamaterials [59, 60, 61]. Similar to the proposed origami structures, the programmable behavior of these metamaterials is a function of their design and geometric architecture. However, the proposed systems are also fundamentally different. In contrast to designs that store and dissipate energy through elastic behaviors [61], the proposed origami tubes are non-recoverable and energy is absorbed through crushing, buckling, and plasticity in the thin sheets (non-recoverable, but a lighter and more efficient method for energy absorption). The potential capability for deployment is also different because the origami tubes could increase the crushing distance, and enable on-demand tuning of the system behavior.

This work serves as an initial demonstration and a proof of concept for the deployable origami tube energy absorbers. To present their capabilities, this chapter is structured as follows: First, the geometry, material properties, and fabrication of the origami tubes are discussed with an emphasis on locking the tubes into a specific state. Next, a finite element (FE) model is introduced to study the energy absorption behavior. The experimental setup for quasi-static and dynamic drop tests are then described. A series of quasi-static experiments are performed to quantify the energy absorption behavior of the tubes at different states of deployment. The effect of tube locking on the energy performance is explored by simulating tube crushing with only one or both ends of the tube restrained. Analytical simulations of the systems allow for a comprehensive parametric study, which explores the performance, and tunable designs offered by various geometries of the tube. A

series of dynamic drop tests are used to demonstrate the tunable stiffness and its influence on the initial impact. Next, a prototype of the zip-tie mechanism is integrated into a physical model to enable self-locking. Finally, the concluding remarks summarize the results, present limitations of the current study, and emphasize topics for further research including the deployment mechanisms, and the physical fabrication of the proposed energy absorbers. An earlier version of this study was presented by the authors in a conference publication [62], while the work presented here contains a more extensive numerical and experimental exploration of the energy absorbing tubes.

## 2.2 System and methods

### 2.2.1 Geometry, fabrication, and locking of origami tubes

The geometry of the proposed deployable energy-absorbing tubes originates from the popular Miura-ori origami pattern. This pattern was first explored as a way to package large membranes and deploy them in outer space [63]. The Miura-ori has been applied in various engineering disciplines, such as the self-locking metamaterials [31] and the deployable canopies [64]. The Miura-ori pattern is developable making it easy to fold directly from a flat sheet. It is flat foldable so it can be stowed compactly and is rigid foldable which allows for fabrication with rigid panel components connected by flexible hinges. The structure also has one-Degree-of-Freedom (DOF) origami kinematics which allows for a prescriptive longitudinal deployment where only the hinges (or folds) deform. Finally, the zipper-coupling concept for Miura-ori tubes adds stiffness to the origami structure [3], which makes it possible to lock the system and crush it as will be discussed further.

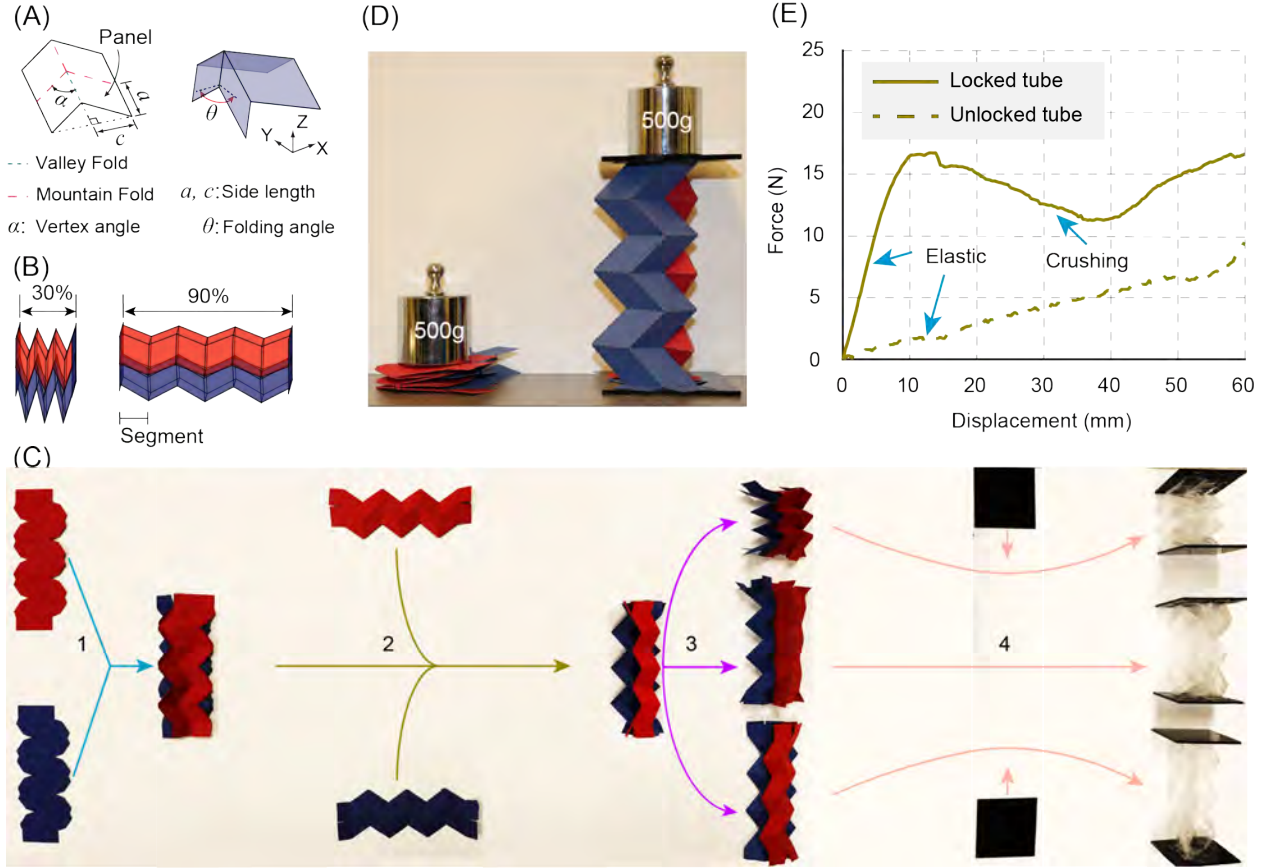


Figure 2.2: Geometry, fabrication, and locking. (A) A unit cell of the Miura-ori pattern is defined by: side lengths  $a, c$ , vertex angle  $\alpha$ , and folding angle  $\theta$ . (B) Zipper-tubes at 30% and 90% extension with one segment indicated. (C) Fabrication process of locked zipper tubes. Paper tubes are shown on the left for visual clarity, and a final tube made from polyester sheets is shown on the right. (D) Comparison of load bearing capacity between unlocked (left) and locked (right) zipper tubes. Locking restricts the kinematic motion and makes the structure significantly stiffer. (E) Axial loading response in quasi-static experiments for locked and unlocked tubes. The locked structure ultimately crushes resulting in the nonlinear response.

The geometric definition of the Miura-ori pattern and zipper tubes begins by prescribing the dimensions of the unit cell (Fig. 2.2A). The unit cell is formed by four identical panels connected at a vertex, with each panel defined by a height  $a$ , width  $c$ , and vertex angle  $\alpha$  (the acute angle of the parallelogram). This unit cell can be folded into a three-dimensional shape where the current geometric configuration is governed by the dihedral folding angle  $\theta \in [0, \pi]$ .

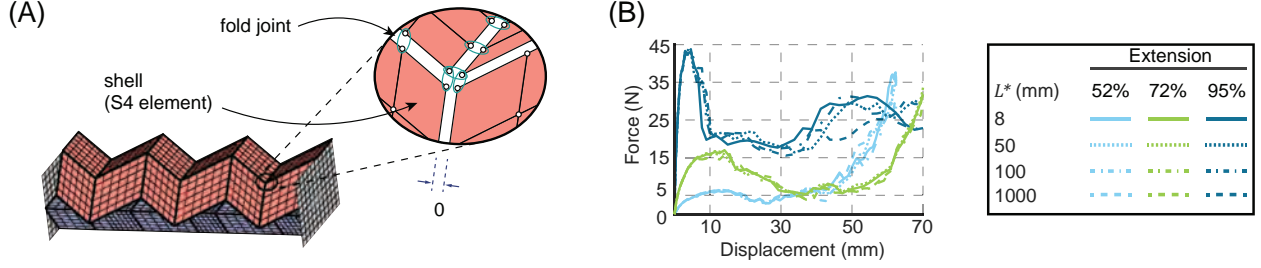


Figure 2.3: Finite element model. (A) The zoom-in figure on top shows the details of the connections between adjacent panels. Finite element model of the locked zipper tubes on the bottom is only representative and a finer mesh is used for the analyses. (B) Axial force-displacement simulation for locked zipper tube with different length scale parameters  $L^*$ .

The zipper-coupled tube system (Fig. 2.2B) is constructed by repeating and connecting symmetric Miura-ori cells. Instead of the dihedral angle, it is more intuitive to use a percentage of extension to define the longitudinal configuration of the tubes. The percentage equals to the ratio of current length to the maximum extended length, which is the product of the number of segments ( $N$ ) and the panel width ( $c$ ). The tube is thus fully deployed when the extension is 100% ( $\theta = \pi$ ) and packed into a compact size when the extension is 0% ( $\theta = 0$ ). This structure has only one flexible deformation mode through which it can be deployed with bending around the fold lines. Other deformation modes require engagement of panel bending and stretching, which significantly increases the stiffness of the system [3].

The zipper tubes were manually folded and glued from laser-cut polyester Mylar® sheets with a thickness of 0.127 mm. Based on a prior work [65], the tubes for all experimental tests consist of six segments, with their planar geometry set to be  $a = c = 25$  mm, and  $\alpha = 55^\circ$ . The systems were locked by constraining both ends with significantly thicker 5 mm acrylic plates.

Fabrication of the locked zipper tubes consists of four major steps (Fig. 2.2C). First, two Miura-ori patterns with three units (six segments) are perforated by a Universal Laser System (VLS 6) and folded into a 3D shape. These two Miura-ori sheets are then flattened again and glued in the zipper orientation (Step 1). This assembly is folded into a 3D shape and two additional Miura-ori sheets are glued to form the complete unlocked zipper tubes (Step 2). Specifically, one sheet is rotated and glued to the other in a zig-zag manner, and a prior work [3] illustrated the connection in its second figure. This system can fold and unfold freely to different states (Step 3). The zipper tubes are designed with tabs on both ends that are glued to two square acrylic plates to lock the tubes (Step 4). The connections between zipper tubes and acrylic plates were made by gluing the two parts together with a LOCTITE® bonding system. The tabs are continuous with the base sheet and are perforated to fold orthogonally against the acrylic plate. Therefore, the relative translation between the zipper tubes and the acrylic plate is restrained, while the edges of the tube are free to

rotate relative to the plate. When this connection with the endplates is complete the structure is locked and can no longer fold without crushing.

We explored zipper tube systems locked at three different levels of extension,  $\sim 50\%$ ,  $\sim 75\%$  and  $\sim 95\%$ . These extensions are chosen to represent a half, three quarters and near fully deployed systems. A 100% deployed structure is not feasible because it is completely flat ( $\theta = \pi$ ). Seven tubes were fabricated for each of the three desired extension ranges. Due to manufacturing error the tubes aimed at half extension ( $\sim 50\%$ ) averaged at 52%, those at the three-quarters extension averaged at 72%, and those at the high extension averaged at 95%. In the subsequent text, we use these averaged extensions to represent the systems folded at the three different extensions.

To demonstrate the importance of locking on the axial stiffness, in Fig. 2.2D we present two identical zipper tubes made with construction paper. The locked structure weights 8.6 grams and can support a mass of 500 g without a visible deformation (58 times its own weight), while the unlocked structure collapses into a flat state by following the one DOF folding kinematics. We also make a quantitative comparison of the axial loading response between locked and unlocked tubes (Fig. 2.2E), where the tests are conducted on polyester prototypes. For the locked tube system, the ends are constrained with acrylic plates. The initial stiffness of the two cases is drastically different. The locked tube has an initial stiffness of 1.8 N/mm, while the unrestrained tube has a stiffness of 0.2 N/mm. The unrestrained tube does not have a zero stiffness and has a generally elastic response because the folds of the system remain elastic, and fabrication imperfections (e.g. adhesive at fold vertices) restrict the perfect kinematic motion of the Miura-ori pattern. These preliminary tests show the large difference that can be obtained by locking the ends of the tubes. We then explore the nonlinear axial crushing of these systems in the subsequent sections.

### 2.2.2 Finite element model

In this chapter, we use a finite element model (ABAQUS/Explicit [66]) that consists of shells elements and rotational hinges as the basis for numerical simulation. The origami panels are meshed with *S4* general purpose shell elements (Fig. 2.3A). Adjacent panels are connected via connector elements (hinges) with prescribed rotational stiffness to simulate the bending behavior of fold lines. Each end of the thin tube system is connected to a plate with significantly higher stiffness to restrain translational movements.

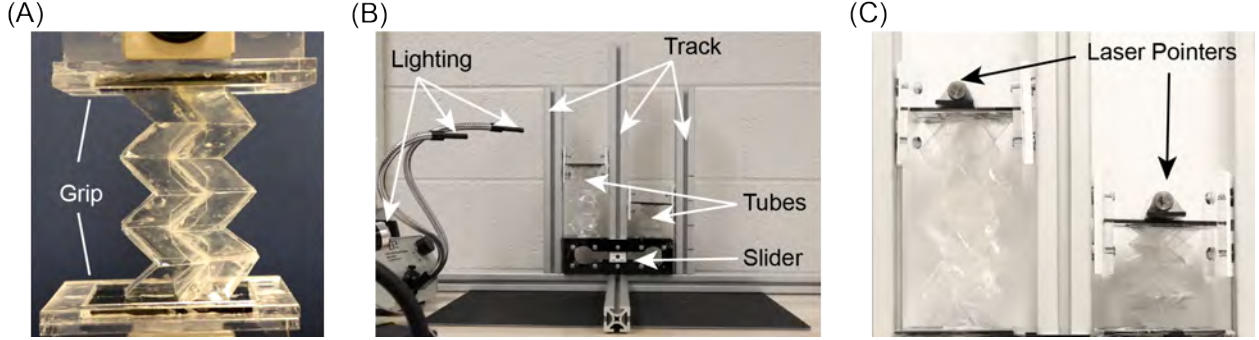


Figure 2.4: Experimental methods. (A) A locked zipper tube in a quasi-static test. (B) The drop test frame. (C) Two laser pointers at the tops of the tubes allow for accurate tracking of the position with a high-speed camera.

In the simulation, the crushing of locked zipper tubes is modeled as axial compression between two rigid plates. One of the rigid plates is set to be completely fixed by restraining all six DOFs, while the moving plate is constrained to only translate along the axial direction of the zipper tubes. The crushing process is controlled by assigning a prescribed downward displacement to the moving plate, in which the moving rate is applied by using a smooth amplitude definition. Self-contact (surface to surface) is applied to model contact between different parts of the zipper tubes and rigid plates. Friction resulting from contact is considered in the model with a coefficient of friction of  $\mu = 0.25$ . The reaction force in the axial direction is monitored in each simulation step and is recorded with respect to the position of the top plate. The force-displacement data is then used to calculate absorbed energy, mean force and maximum force. Convergence with respect to the mesh size is examined, and a mesh size of  $2.5 \times 2.5$  mm is chosen because it is able to provide a strain energy solution that is within 2% of a mesh with  $1 \times 1$  mm elements. The simulation time is set to be 20 ms to keep the ratio of kinetic energy to strain energy under 5% so the dynamic effects can be considered as negligible to the global response.

Material properties for the polyester films are assumed to be isotropic. Young's modulus is set to be  $E = 4.4$  GPa based on the material tests, and Poisson's ratio is assumed to be  $\nu = 0.33$ . The model dimensions and thickness are set to be the same as the physical models that were fabricated. The rotational stiffness ( $K_l$ ) of the folds can vary dramatically due to the variation in materials, fabrication, and folding history. Previous research [67, 68] reveals that ( $K_l$ ) is expected to be proportional to the length of fold lines and the bending stiffness of the thin-sheet material. The equation to calculate rotational stiffness is empirically written as

$$K_l = \frac{L_F}{L^*} \cdot \frac{Et^3}{12(1 - \nu^3)} \quad (2.1)$$

where  $E$ ,  $\nu$  are the Youngs modulus and Poissons ratio of material, and  $t$  is the thickness of panels.  $L^*$  is the length scale parameter which relates the bending of fold lines to the bending of initially flat sheets.

The stiffness  $K_l$  is then dependent on  $L^*$  and there is no theoretical basis for determining the exact value of  $L^*$ . Therefore, a sensitivity analysis is performed (Fig. 2.3B) by compressing tubes of 52%, 72%, and 95% extension with different length scales,  $L^* = 8, 50, 500, 1000$  mm. As the response curves are relatively close to each other for substantially different length scales, we determine that the global crushing behavior is not sensitive to the local fold stiffness. This phenomenon occurs because the axial crushing is mainly influenced by the constrained geometry from the rigid end plates rather than the local bending stiffness.

Based on the material tests, the elastoplastic constitutive relationship for the polyester material used in the numerical simulation can be modeled as the following

$$\sigma \text{ (Mpa)} = \begin{cases} 4400\varepsilon & \varepsilon < \varepsilon_y = 0.0227 \\ 153.86(\varepsilon - \varepsilon_y) + 100 & \varepsilon_y \leq \varepsilon \leq 0.15 \\ 120 & 0.15 \leq \varepsilon \end{cases} \quad (2.2)$$

### 2.2.3 Experimental methods

Quasi-static uniaxial compression tests of locked zipper tubes are used to explore the nonlinear force-displacement behavior of these systems. First, a set of tensile coupon tests were performed to verify the elastic modulus of the polyester sheets and to test the strength of the adhesive connections. The stress-strain relationships of the coupons are used for the numerical simulations and provide background on the validity and limitations of the experimental tests.

A specialized grip (Fig. 2.4A) is fabricated to connect the locked zipper tubes to the test machine, where the tube endplates fit within voids of the grips and are adhered with plastic tape to stay in place. This configuration allows the test machine to apply a compressive force to the locked zipper tubes without restricting rotation at the top. An Instron 5969 dual column axial testing frame is used for the testing with a 1000N load cell attached to the top grip to record the reaction force. The displacement of the load cell is controlled and recorded by the machine. A testing rate of 25.4 mm/min is used for all experimental tests in this study. Through the numerical simulation we showed that even at fast loading rates (completing the analysis in 20 ms) the internal dynamics are insignificant when compared to the nonlinear crushing behaviors.

Drop tests are carried out to explore the dynamic properties of locked zipper tubes under a low-energy scenario. The displacement is recorded by tracking a laser pointer attached to the top of the constrained zipper tubes using a high-speed camera. The setup for the dynamic experiments is shown in Fig. 2.4B, C. The tests are built into a vertical track with T-slot parts (80/20 Inc.).

A slider which can move vertically along the track was used to hold the zipper tubes. Horizontal movement at the top of the tubes was restricted by additional sliders while still allowing for vertical movement of the tube (Fig. 2.4B). Two tubes can be accommodated on the slider and tested under the same conditions. They are dropped simultaneously and the sliders for horizontal restriction are the same for both tubes. A lighting system is provided to illuminate the devices in order to capture high-quality images with a high-speed camera (Photron INC., FASTCAM SA5). Videos are recorded at a frame rate of 2000 frames per second. For the quantitative results, displacement is tracked using the high-speed images. Tracking of the objects was most precise when measured from two laser pointers attached to the top of the zipper tubes (Fig. 2.4C). These laser pointers provided precise point-based locations for the tube tops through the duration of the drop test.

### 2.2.3.1 Preliminary experimental tests

The experimental study in this work explored the energy absorption through a series of quasi-static compression tests and dynamic drop tests. We performed a series of component tests to verify the overall suitability of the fabricated prototypes and identify limitations in the experimental study. First, the stress-strain relationship of the polyester sheet was tested with different loading rates as shown in Fig. 2.5(A). As the strain rate is doubled, the elastic modulus is not affected, and the yield stress is reduced only by several percent. Thus, when considering the quasi-static tests that we perform in this research (loading rate of 25.4 mm/min), the behavior of the polyester can be considered rate independent. Within the dynamic drop tests, we did not observe yielding and failures, and can assume that the materials remained in the rate-independent elastic region.

Next, we performed tests on the bonding strength of the adhesive system. We tested several types of fabrication and adhesive types and found the LOCTITE® bonding system to be the only one suitable for connecting the polyester sheets. Fig. 2.5(B) shows ten component tests where a 2 cm by 10 cm strip of polyester (0.127 mm thick) is adhered to an acrylic plate of the same surface dimensions (5 mm thick). The adhered region is 5 mm by 2 cm. A tensile test on this connection shows that most samples reach the yield strength of the polyester with some samples failing at 90% of the yield strength. The polyester to acrylic connection is representative of how the tubes are connected to the base plates which is important for achieving the locked behavior. We conduct a similar test to investigate the connection strength between two polyester sheets (same dimensions and adhered region as above). These tests are representative of the regions of tubes that are adhered together. In this set of ten tests (Fig. 2.5(C)) only four tests reach the fully yield strength of the polyester, and two samples fail at a strength as low as 30% of the yield strength. In the axial tests of the zipper tubes, we did sometimes observe adhesion failures at the connections between tubes. The majority of these failures occurred during the densification phase of the testing (Fig. 2.7-point No. 3). The uncertainty associated with the adhesive failures is likely the reason for

the larger spread in experimental results recorded for the tubes at a 95% deployment (Fig. 2.5(C)). Despite this variability, the overall trends between extension and axial performance match between the experimental and analytical results.

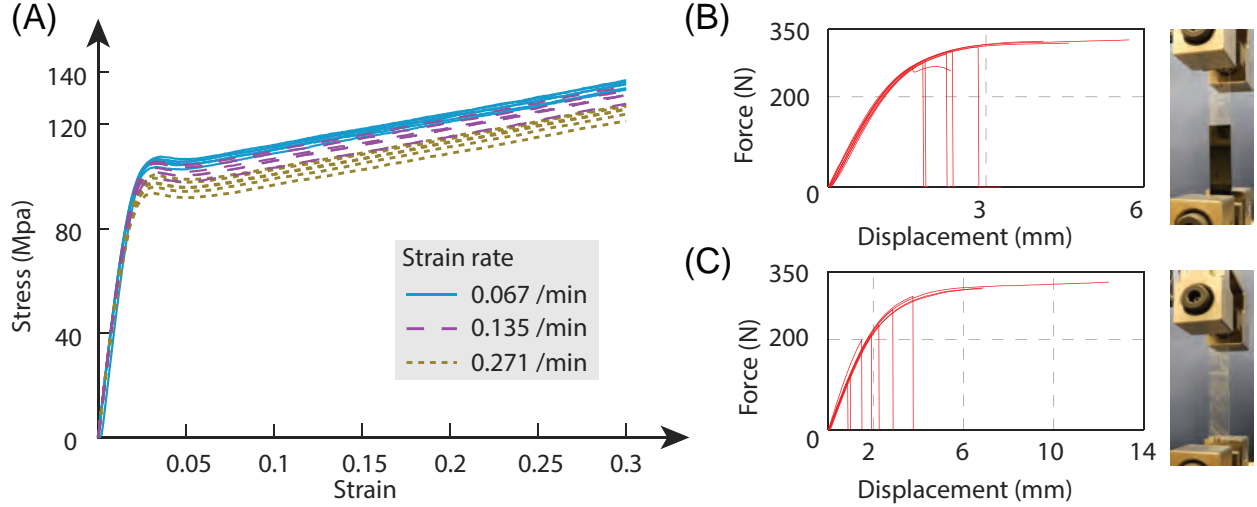


Figure 2.5: Preliminary tests. (A) Stress-strain relationship of polyester under different loading rates. (B) Force-displacement response of polyester sheet connected with adhesive to an acrylic plate. (C) Force-displacement response of two polyester sheets connected by adhesive.

### 2.2.3.2 Laser tracking and error analysis

Considering that the falling displacements are measured with images, a possible source of error in the measurement may come from the transformation between real distances and camera-recorded distances. The camera-recorded distance is the field angle corresponding to the real distance, and an equal distance in different positions could induce different field angles. A sketch of the side view of the test setup is shown in Fig. 2.6(A) to illustrate this error and to provide a guide for displacement calculation. The high-speed camera is set to be on the same horizontal plane of the collision point, and the side view can be simplified into the diagram shown in Fig. 2.6(A).

The distance between the track and camera is  $L$ , the falling distance is  $d_F$ , two identical infinitesimal displacements near the starting point and the end point are denoted with  $d_x$ . The field angles corresponding to  $d_F, d_x$  are  $\varphi, d\theta_1, d\theta_2$ . The following relationships can be derived using the basic trigonometry:

$$\varphi = \tan^{-1} \left( \frac{d_F}{L} \right) \quad (2.3)$$

$$d\theta_1 \approx \frac{dx \cdot \cos \varphi}{L / \cos(\varphi)} = \frac{dx}{L} \cdot \cos^2 \varphi \quad (2.4)$$

$$d\theta_2 = \frac{dx}{L} \quad (2.5)$$

Substituting  $d_F = 15\text{cm}$ ,  $L = 105\text{cm}$  into Eq. (2.4), (2.5), the relative error of field angles is

$$\text{error} = \frac{d\theta_1 - d\theta_2}{d\theta_2} \approx 0.02 = 2\% \quad (2.6)$$

Therefore, the largest relative error of the camera-recorded distances in different positions is no more than 2%. In the next section, we show how the pixel distances (see the next section) can be used to calculate the time history of displacement.

The acceleration is measured by twice differentiating the displacement time history during the drop test. Displacement of the laser pointer is recorded at intervals of  $\Delta t = 0.5\text{ ms}$ . Calculation of the time history of acceleration was conducted using three steps: i) calculate the pixel coordinates of the laser pointers in the images; ii) convert pixel coordinates to physical distance; iii) twice differentiate the displacement time history to obtain the acceleration time history.

Pixel coordinates of the laser pointer in every frame were obtained by translating the images into black and white. A representative frame of the falling process (Fig. 2.6(C)) has two white spots corresponding to two laser pointers on different zipper tubes. As the falling is guided by the slide track to follow the x-direction, only the x-coordinate of the pixels is calculated. A tracking point, which is the centroid point of the white spot (Fig. 2.6(C)), is selected to represent the location at the top of the tube (centroid of light). The x-coordinate of the tracking point in the  $k^{\text{th}}$  frame can be calculated as:

$$x^k = \frac{1}{N} \sum_{i=1}^N x_i^k \quad (2.7)$$

where  $N$  is the number of pixels in the white spot,  $x_i^k$  is the pixel-coordinate of the  $i^{\text{th}}$  pixel (see Fig. 2.6(D) for the illustration). Then the displacement (in terms of the number of pixels) in the  $k^{\text{th}}$  frame can be calculated as following

$$D^k = x^k - x^1 \quad (2.8)$$

This pixel-displacement can be converted to displacement in meters by dividing by a constant

$$d^k = \frac{D^k}{\lambda} \quad (2.9)$$

where  $\lambda = 5837\text{ m}^{-1}$  is the obtained by taking a benchmark image. The displacement time history of the tracking point is then obtained as  $d^k \sim t^k$ , where  $t^k = k \cdot \Delta t$ .

The time history of the acceleration is calculated by differentiating the displacement time history. Considering that high frequency noise in the original data can deviate the results from the

actual value, post-processing is needed to smooth the data. The displacement is downsampled by 12 and then smoothed using the moving average filter. The filter can be expressed as

$$\tilde{d}^k = \sum_{i=k-2}^{k+2} \frac{d^i}{5}, \quad \tilde{d}^1 = d^1, \quad \tilde{d}^2 = \frac{d^1 + d^2 + d^3}{3} \quad (2.10)$$

where  $d^i$  is the un-smoothed data and  $\tilde{d}^i$  is the smoothed data. A comparison between the raw data and the processed data is shown in Fig. 2.6(E) for one drop test from 15 cm. The difference brought by the process as shown can be neglected and the smoothed displacement data is used to calculate acceleration by twice differentiation.

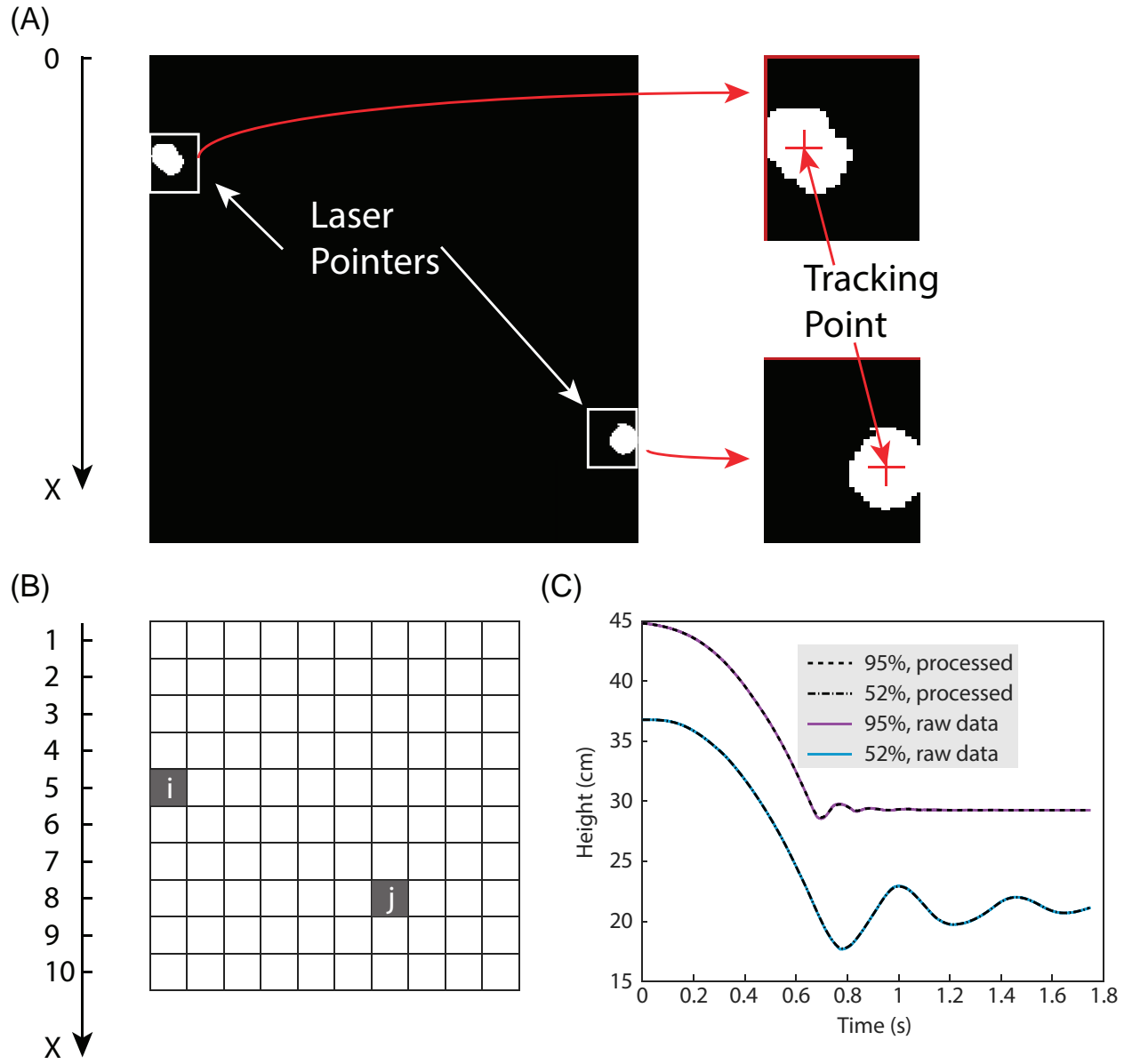


Figure 2.6: Laser tracking process. (A) Sketch of the side view of the test setup and diagram of the error analysis of the distance measurement. (B) A representative frame shot by the high-speed camera during the drop test. The two white spots corresponding to two laser pointers attached to the top of zipper tubes and tracking points are selected as the centroids of the spots. (C) Illustration of pixel coordinates: the pixel x coordinate of the  $i^{\text{th}}$  grid shown in the figure is five, the  $j^{\text{th}}$  grid is eight. (D) Time history of displacement: raw data and processed data for zipper tubes at 95% extension and 52% extension.

## 2.3 Results

### 2.3.1 Quasi-static axial tests

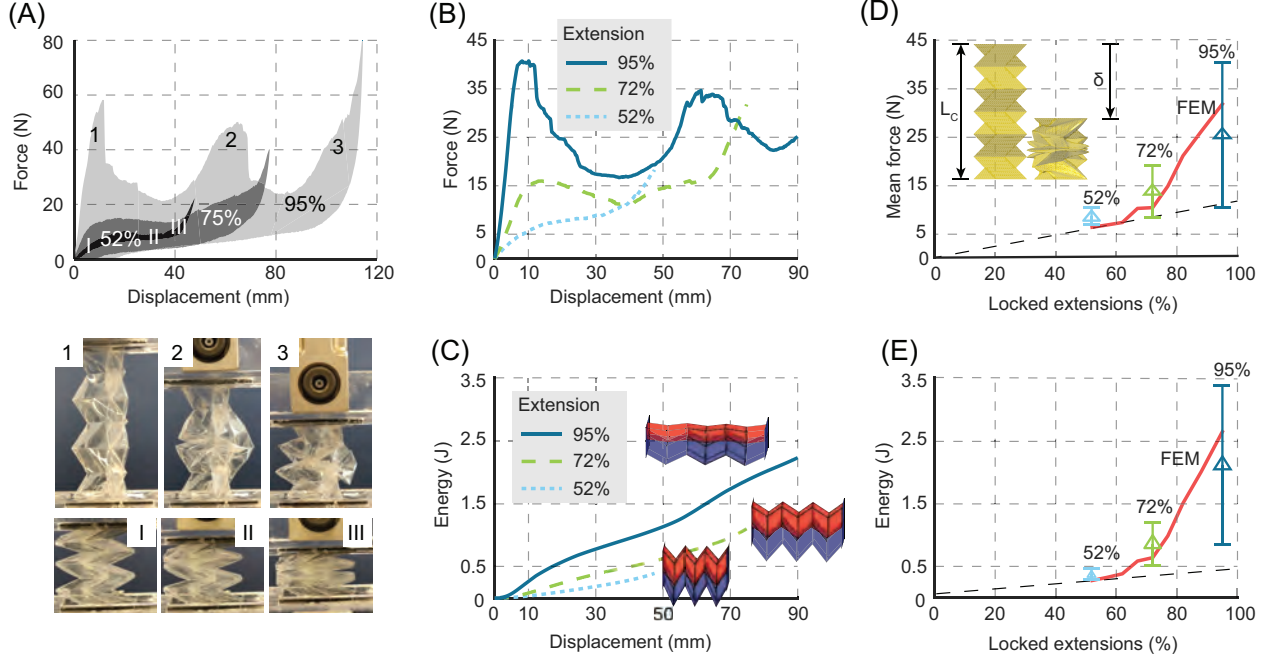


Figure 2.7: Quasi-static axial loading response of locked tubes. (A) Load-unload cycle response of tubes extended to 52%, 72%, and 95% (top) and corresponding experimental photos for the 95% and 52% extensions (bottom). The shaded area is the dissipated energy during a load-unload cycle. (B) Mean value of loading responses from seven experiments for each extension. (C) Mean value of energy absorption from seven experiments for each extension. (D) Comparison of mean force between experimental testing and numerical FEM simulation (for a crushing distance  $\delta/l_c = 50\%$ ). (E) Comparison of absorbed energy between experimental testing and numerical FEM simulation (for a crushing distance  $\delta/l_c = 50\%$ ).

Zipper tubes locked at three different states of extension, 52%, 72% and 95%, are tested with a load-unload cycle (Fig. 2.7A, Movie S1), where the shaded area denote the dissipated energy during a load-unload cycle. The initial stiffness increases with the extension of the tubes (i.e. 1N/mm for the 52%, 1.8N/mm for the 72%, and 6.5N/mm for the 95%). The tubes at 52% extension show a nearly elastic response and recovery; and thus, little energy is dissipated. During loading there is some elastic buckling and minor yielding (point No. I), followed by a plateau (point No. II), and finally some densification of the tube (point No. III). Upon recovery, the force-displacement response is nearly identical with the buckled locations recovering to the initial configuration. For the tubes with 52% extension, most of the deformations occur as recoverable buckling and local

bending around fold lines which follows the one DOF kinematics of the origami. The tubes locked at higher extensions have a more nonlinear force-displacement response because more panel deflection, buckling, and local yielding occur. The force-displacement results for the zipper tubes at 95% extension show three peaks during the loading process. Before the first peak, the zipper tubes have a linear elastic response to the axial loading. Due to the buckling and local cracking in the adhesive around fold lines, the force drops sharply at point No. 1. As the loading is continued, localized contact occurs at the central segments, which leads to another peak in the force-displacement curve (point No. 2). More buckling around end-segments of the tube brings the force down until the whole structure becomes densified (point No. 3). As the system is unloaded, it has a low stiffness and recovers near linearly (from 80 to 0 mm displacement). The response of the tube with 72% extension is between the two other cases. Buckling, yielding and local bending around fold lines are affecting the global responses simultaneously in the tube with 72% extension. Buckling and yielding induce a drastic change in the forces and non-recoverable deformations, whereas the local bending will increase the forces and recover after unloading. A combination of these opposing effects distinguishes the loading response from the nearly elastic behavior of the tube with 52% extension, or the fluctuating forces of the tube with 95% extension.

To verify the overall behavior with respect to extension, seven individual tests are performed for each of the three cases. The overall force-displacement for the three sets of tests are similar to those shown in Fig. 2.7A. The systems with low extension (52%) have a nearly recoverable response, those at a high extension (95%) have three peaks, and the third set (72%) again fall in the middle. The load-displacement response for each set of tubes are averaged and presented in Fig. 2.7B. The overall behavior is again influenced by the extensions. The tubes with larger extension exhibit a larger axial stiffness, a higher peak force for crushing, and are able to provide a longer crushing distance before densification.

As illustrated in the Fig. 2.1A, the absorbed energy for each test is characterized as the area underneath the force-displacement curve. Fig. 2.7C shows the absorbed energy versus the crushing distance for the three sets of experimental tests (each set is averaged). This plot shows another tunable behavior benefited from the deployable property of these systems. The tubes with larger extensions have higher levels of energy-absorbing capability even for the same crushing distance (slopes of lines in Fig. 2.7C). From the quantitative comparison of mean values of energy absorption, the locked zipper tubes extended to 95% can absorb 2.3J while those at 52% absorb less than 0.4J. However, the mean forces and peak forces also increase with the extension. In summary, the behavior obtained from quasi-static tests show that the axial response including stiffness, peak force for crushing, and total energy absorption can be changed dramatically for the same tube design. By deploying and locking the tubes at different extensions, it is possible to tune the behavior without changing the system design.

Finite element numerical simulations are performed for the same range of tube extensions, and the results are compared with experimental results in terms of the mean reaction force and absorbed energy (Fig. 2.7D, E). The large variation of experimental results comes from the limited specimens. For each deployment ratio, we made seven samples for the quasi-static compressions. The variation can be narrowed by testing more samples.

These results are obtained when we compare the systems over a crushing distance of  $\delta/L_c = 60\%$  of the total length of locked zipper tubes (see schematic in Fig. 2.7D). Comparing over only a portion of the crushing distance (50-80%) provides a more reasonable comparison, because the finite element models substantially overestimate forces and energy absorption in the densification regime. For the limited range, the mean forces and total energies are in reasonable agreement with those obtained from the compression experiments. Additionally, the overall trends are similar and show that the extension can be used to increase the forces and the total amount of energy absorbed. Finally, the increase of energy absorption from extending the tubes is substantially faster than a linear growth (dashed line in Fig. 2.7E). In other words, if the tube is already deployed past 50% extension, a small additional extension will result in much higher forces and energy absorption.

### 2.3.2 Benchmark comparison

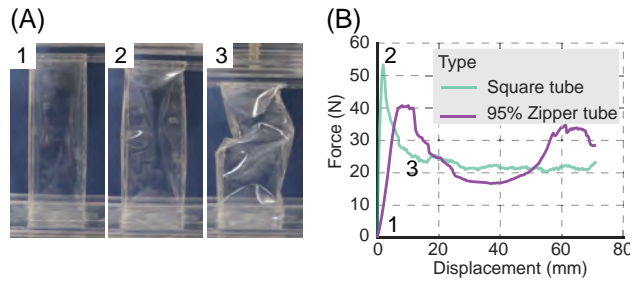


Figure 2.8: Comparison of the energy absorption behavior between prismatic tubes and locked zipper tubes of the same length. (A) Experimental photos of prismatic square tubes, the numbering corresponds to part (B). (B) Mean value of loading responses from seven experiments for prismatic tubes and locked zipper tubes at 95% extension.

Seven conventional square tubes of the same length and cross-sectional area are tested to set a benchmark for evaluating the relative energy-absorbing behavior of the locked zipper tubes. The square tube is selected as a representative of the conventional thin-walled prismatic energy absorbers, because those devices have similar loading responses where the critical buckling causes a high initial peak force and subsequent sharp decrease. These square tubes are fabricated with the same polyester sheets as the locked zipper tubes, where the total amount of material used

and the axial length of the squared-tube are equal to the locked zipper tubes at 95% extension. Both ends of the prismatic tube are glued to two square acrylic plates to restrain the translational movement (Fig. 2.8A). These prismatic tubes are tested using the same loading procedure as the locked zipper tubes and the mean loading responses are plotted in Fig. 2.8B for the prismatic tubes and the locked zipper tubes at 95% extension. The energy-absorbing characteristics are compared over the whole crushing distance of  $0.5L_c = 72.5$  mm, where  $L_c$  is the initial length of both tubes. The comparison shows that initial peak force of the locked zipper tubes (40.7N) is 23.6% lower than the initial peak force of the prismatic tubes (53.3N), whereas mean crushing force of the locked zipper tubes (24.9N) is slightly higher than the mean crushing force of the prismatic tubes (23.9N). These results show that the zipper coupled origami pattern offers similar advantages for energy absorption as those presented with other origami inspired designs [36], and can provide an overall comparable response to prismatic tubular systems. Notice that if the comparison is carried out over a shorter crushing distance (e.g.,  $0.14L_c \approx 20$  mm), the mean crushing force of the square tube (29.5N) will be greater than that of the zipper tube (28.8N). However, to absorb more impact energy, a thin-walled tube is typically crushed over a longer portion of the initial length (e.g., half of the initial length or more).

### 2.3.3 Influence of the end constraints

Figure 2.2D shows that a zipper tube that is locked on both ends can offer significantly more stiffness than an unrestrained tube, and is thus suitable for energy absorption. The numerical study of energy characteristics is now extended to zipper tubes that are only restrained on the bottom, and the locking at the top plate is released. The FE model of the bottom-restrained zipper tube is built with same geometry as the fully-locked tube, while the top plate now only serves as a moving plate to compress the tube. Finite element simulations are performed for the same range of extensions from 52% to 95%, and the mean crushing forces are compared with those of fully-locked tubes (Fig. 2.9A). The results compare the tubes over a crushing distance of  $\delta/L_c = 50\%$  of the total length. Both trends show that the mean forces ( $P_m$ ) increases with the axial extension, while the fully-locked tubes have a higher  $P_m$  over the whole range of extensions. The fully-locked zipper tube can absorb more energy because the restraint from the top plate results in more panel crushing within the segments that are close to the top.

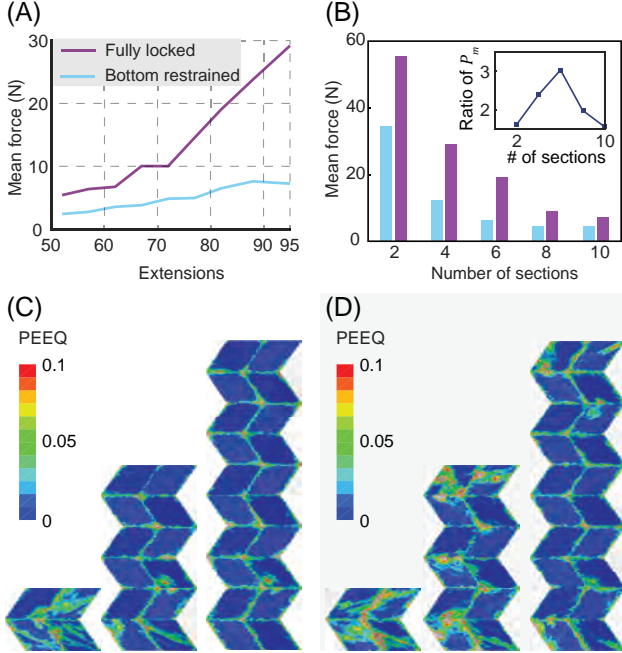


Figure 2.9: Comparison of the energy absorption behavior between zipper tubes that are locked on both ends and zipper tubes that are restrained only on the bottom end. Comparison of mean force for (A) different extensions, and (B) different number of segments, while the extension is set to be 82%. The crushing distance  $\delta/L_c = 50\%$ . Plastic deformation for (C) the bottom-restrained and (D) the fully-locked tubes with different number of segments deployed to 82% extension (PEEQ is plotted on the undeformed shape).

For zipper tubes with different number of segments, the top restraint has a different level of influence on the overall energy behavior. Keeping the panel geometry to be the same, zipper tubes with different number of segments are compressed from 82% extension, and their mean forces are shown in Fig. 2.9B. With more segments in the tube, the mean force decreases for both the fully-locked and the bottom-restrained tube, because with more segments there is more kinematic deformation and less crushing. However, the difference between the mean forces, quantified as the ratio of the fully-locked  $P_m$  to the bottom-restrained  $P_m$ , varies with the number of segments (insert in Fig. 2.9B). The ratio first increases then decreases with the number of section, and it reached the peak for six segments. The trend of this ratio is related to the distribution of crushing in the two different locked cases, which can be explored by through the equivalent plastic strain, PEEQ, in the systems (Fig. 2.9C, D). With only two segments, the case with only the bottom restraint still provides substantial constraint to the kinematics of the tube, inducing similar panel crushing and plastic strain to those of the fully-locked tube. Thus, the fully-locked  $P_m$  is only 1.6 times as high as the bottom-restrained  $P_m$ . For the bottom-restrained tube with six segments, the top panels are much less restrained and do not experience crushing, while the fully-locked

tube can provide restraints and cause more panel crushing. Thus the ratio of  $P_m$  increases to 3. Furthermore, with ten segments in the tube, the majority of the panels in both tubes will follow the kinematic folding motions of the creases, regardless of the existence of the top restraint. The ratio of  $P_m$  drops back to 1.6, which implies that the energy absorption is not significantly improved by adding the top restraint.

### 2.3.4 Parametric study

The finite element simulations are extended to conduct a parametric study where the geometry of locked zipper tubes is varied. From the parameters used in the geometric design of zipper tubes, the number of segments  $N$ , the vertex angle  $\alpha$ , and the aspect ratio  $a/c$  (Fig 2.2. A, B) result in differences in the system performance. To enable a fair comparison within the parametric study, the total material cost and the shell thickness of the zipper tubes is kept the same for all cases. As the number of segments is changed, the size of panels (variables  $a$  and  $c$ ) changes such that the material cost remains the same. The crushing percentage ( $\delta/L_c$ ) is set to be 80% for all simulations. Changing the number of segments does not change the overall kinematics of the tubes. The vertex angle and the aspect ratio characterize the planar geometry of the Miura-ori pattern, which affects the global shape of the system. Changing the vertex angle or the aspect ratio does not affect the size of the panels (variables  $a$  and  $c$ ). The vertex angle does affect the folding kinematics of the system where tubes with higher  $\alpha$  change their shapes to essentially square-like tubes when fully deployed. The aspect ratio also alters the folding kinematics, where a larger aspect ratio defines a shorter and more dense zipper tube. The crushing characteristics of the different parametric cases are compared in terms of the energy absorption and the maximum force  $P_{\max}$  (Fig. 2.10).

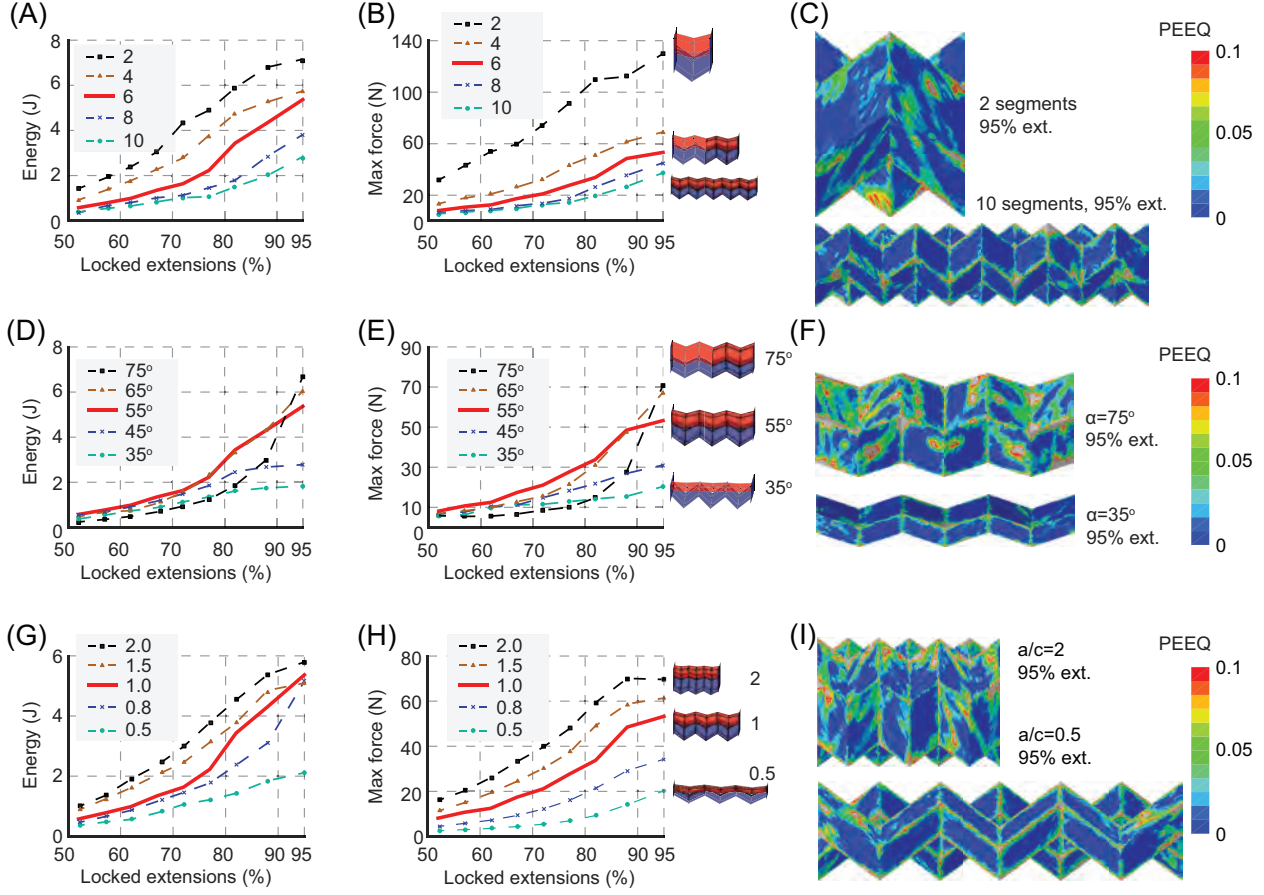


Figure 2.10: Parametric variation of tube geometry. (A) Energy absorption and (B) maximum force for tubes with different number of segments. (C) Plastic deformation for two tubes with a different number of segments (PEEQ is plotted on the undeformed shape). Distributed panel plastification is observed for tubes with only two segments, whereas most plastic deformation occurs around fold lines for tubes with ten segments. (D) Energy absorption and (E) maximum force for tubes with different vertex angles. (F) Plastic deformation for tubes with different vertex angles deployed to 95% extension (PEEQ is plotted on the undeformed shape). Distributed panel plastification is observed for tubes with a vertex angle of  $\alpha = 75^\circ$ , whereas most plastic deformation happens around fold lines for tubes with a vertex angle of  $\alpha = 35^\circ$ . (G) Energy absorption and (H) maximum force for tubes with different aspect ratios. (I) Plastic deformation for tubes with different aspect ratios deployed to 95% extension (PEEQ is plotted on the undeformed shape). Distributed panel plastification is observed for tubes with an aspect ratio of  $a/c = 2$ , whereas most plastic deformation happens around fold lines for tubes with an aspect ratio of  $a/c = 0.5$ .

### 2.3.4.1 The number of segments

When increasing the number of segments in a tube, both the absorbed energy and the maximum force decrease (Fig. 2.10A, B). The general trends are similar to those observed in the

experiments, and the force/energy characteristics with respect to deployment remain aligned for the different number of segments (lines do not overlap). To compare the efficacy of these systems as energy absorbers we compare the ratio of the amount of energy absorbed at 95% extension to the corresponding peak force ( $\delta \cdot P_m / P_{\max}$ , summarized in Table 2.1.). All these systems use the same amount of material, so if more energy absorption is desired, then the design with the fewest segments should be used (Fig. 2.10A). However, if it is also desirable to mitigate the peak crushing forces, then tubes with six segments provide the maximum energy absorbed for the lowest relative peak force (Table 2.1). These trends are a result of the strain distribution and crushing behavior of the origami tubes (see Fig. 2.10C where the PEEQ represents the equivalent plastic strain status). For the most part, we see the high strains to be happening around diagonals. Additionally, we see the high strains happening at the vertices. The only case where we see islands of high strains is when there are only two segments in the zipper tube. All the tube panels are subjected to constraints from the rigid plates. The local rotations are restrained, leading to crushing and higher strains. For the zipper tube with more segments, portions in the middle of the tube have less restriction and can experience a more controlled buckling that also involves kinematic deformation of the system. These buckling characteristics and the plasticity distributions could allow for more advanced designs of the structures, where the number of segments could be used to design the mean to maximum force ratio in the system.

Number of Segments	2	4	6	8	10
$\delta \cdot P_m / P_{\max} (10^{-1}\text{J/N})$	0.55	0.83	1	0.84	0.76
Aspect Ratio $a/c$	0.5	0.8	1.0	1.5	2.0
$\delta \cdot P_m / P_{\max} (10^{-1}\text{J/N})$	1	1.5	1	0.83	0.83

Table 2.1: The ratio of the amount of energy absorbed at 95% extension to the corresponding peak force ( $\delta \cdot P_m / P_{\max}$ ).

### 2.3.4.2 The planar geometry

Both the vertex angle  $\alpha$  and the aspect ratio  $a/c$  can change the planar geometry of the Miura-ori pattern. When varying the vertex angles the energy absorption properties with respect to the system extension show different nonlinear trends (Fig. 2.10D, E). For a tube with a vertex angle of  $\alpha = 75^\circ$  the energy absorption increases from 0.24J at 50% extension to 6.76J for a 95% extension

(28 times increase). On the other hand, the trend for a smaller vertex angle is smoother without such a drastic variability. For example, the tube with  $\alpha = 35^\circ$  has an energy absorption of 0.37J at 50% extension and only increases to about 1.82J at 95% extension (only a 4.9 times increase). The maximum forces follow these same general trends where higher vertex angles result in higher variability with extension. These results show that the vertex angle can be used to control *how tunable the system is*. The change in the energy absorption trends relate to the kinematics of the systems. When the tubes are deployed to a smaller extension (e.g. 50%) the crushing of all tubes follows the fold kinematics and little energy is absorbed. When deployed to higher extensions (above 90%) crushing the tubes with large vertex angles engages local panel deformations and distributes plasticity throughout the system, while crushing tubes with small vertex angles still follows the fold kinematics (Fig. 2.10F).

When increasing the aspect ratio  $a/c$  of the tube panels, both the absorbed energy and the maximum force increase (Fig. 2.10G, H). The ratio of the energy absorption at 95% extension to the corresponding peak force ( $\delta \cdot P_m / P_{\max}$ ) is compared to show the efficacy (Table 2.1), and the tubes with aspect ratio around 1.0 offer the highest efficacy. The change of the energy absorption and the max force is related to the global shape difference (Fig. 2.10I). The tubes with large aspect ratio are shorter and more dense (Fig. 2.10I), i.e., have more amount of material in a unit longitudinal length. When the tubes are compressed, the same crushing distance results in more material deformation in the tubes with large aspect ratio. Furthermore, for the zipper tubes with large aspect ratio, the tube panels also have more restriction from the rigid plate due to the smaller longitudinal length, causing higher strains within the tube panels (Fig. 2.10I). Thus, the energy absorption and the max force both increase with the aspect ratio based on the above two effects.

### 2.3.5 Drop tests and dynamic analyses

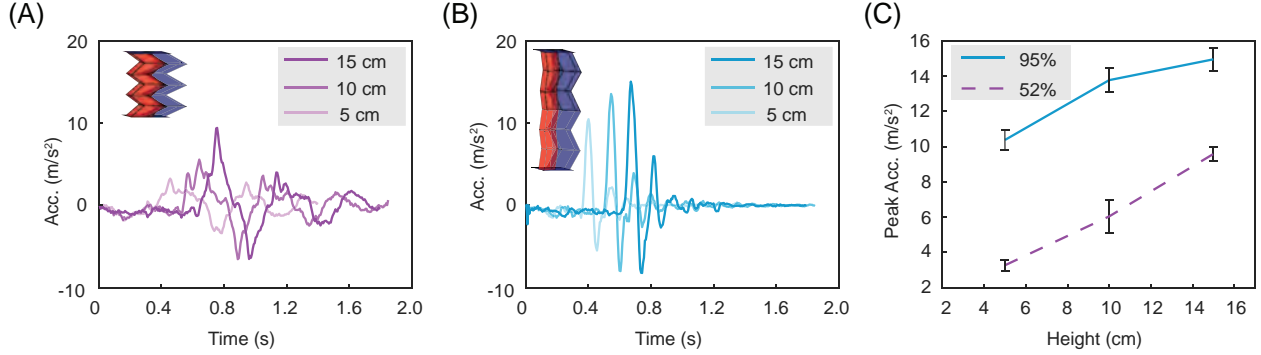


Figure 2.11: Drop tests demonstrating peak accelerations in a low-energy impact scenario. (A) Time history of acceleration for tubes with an extension of 52% and (B) tubes with an extension of 95%. (C) The peak accelerations after collision versus drop heights. The 90% confidence intervals are indicated with vertical bars and are derived from four repeated tests.

Mechanical properties such as axial stiffness and yielding forces can be extracted from the quasi-static loading response, whereas the ability of the absorber to provide buffering during impact can be characterized by exploring the acceleration time history after a free drop and collision. A small mass is attached to the top of a locked tube to provide enough impact, and the drop frame (Fig. 2.4B) is used to test the buffering capabilities. The tests are performed at three different heights and the peak acceleration versus drop height are calculated (Fig. 2.11A-C). The acceleration time history is calculated by twice differentiating the displacement data. The longer constrained zipper tubes (95% extension) result in a larger peak acceleration after the collision when compared to tubes with the same geometry but shorter extension. For the drop test from a height of  $h = 5$  cm, the peak acceleration for a zipper tube at 52% extension averages at  $3.5 \text{ m/s}^2$ , whereas the peak acceleration for tubes at 95% can reach  $10 \text{ m/s}^2$ . Similar relations can also be observed with different drop heights. The peak acceleration during a collision is correlated to the damage that can be transmitted to protected objects. A lower peak acceleration (52% extension) corresponds to better protection, and a higher peak acceleration (95% extension) means more serious damage. Although the friction in the system is not negligible, it does not affect the comparison between the tubes, as they are dropped simultaneously with the same setup (discussed in the experimental methods).

Dynamic buffering capability is also demonstrated qualitatively using drop tests with: i) two measuring cylinders containing 2 cm of colored water which are placed on locked zipper tubes with extensions of 52% and 95% (Movie S2); ii) eggs on top of a 52% locked zipper tube and the slider (Movie S3).

In this low-energy scenario, these structures with extension of 95% do not crush during the test, and their high stiffness causes the higher accelerations. On the other hand, the tubes with a 52% extension, have a substantially lower stiffness, and remain nearly elastic (even when slight crushing and nonlinearity occurs (Fig. 2.7A).

## 2.4 Locking mechanism

In this subsection, we show a locking mechanism inspired by zip ties that allows the deployment and subsequent self-locking of the zipper-coupled tubes (Fig. 2.12). On each end of the zipper-coupled tube, there is one edge that is glued to the end plate, and a parallel edge that is able to move and engage with the locking mechanism (Fig. 2.12A). As the zipper tube deploys in the x direction, the tube dimension in the y direction shrinks, and the two parallel edges move closer together. The deployment and self-locking can then be realized by allowing the two edges to approach each other, but creating locking components that prevent them from moving apart again. The zip-tie inspired mechanism can fulfill this function. Two racks of inclined ridges are bonded onto each rigid plate, and the ridges are set to be inclined toward the direction along which the parallel pair will get closer. (Fig. 2.12A). The glued edge is bonded to the rigid plate to restrain relative translations, and the lock edge serves as a ratchet. As the tube extends, the lock edge travels past each ridge without much resistance. If the lock edge moves back in the opposite direction, it will go under the ridges, and its motion will be prohibited by the inclined ridge. Thus if the tube is compressed, the locking mechanism will prevent it from folding back to a flat state.

A physical self-locking example is shown in Fig. 2.12B and Movie S4. With two built-in racks of inclined ridges on the plastic plates, the zipper-coupled tube can deploy and stay at  $\sim 70\%$  extension (Fig. 2.12B, part 2) and  $\sim 90\%$  extension (Fig. 2.12B, part 3). A mass of 500 g can be supported by the self-locking tube (Fig. 2.12B, part 3), demonstrating the strength of the zip-tie locking mechanism. Finally, by rotating the plastic plates about the glued edge, the racks of inclined ridges will detach from the tube, and the tube can come back to its initial state (Fig. 2.12B, part 4).

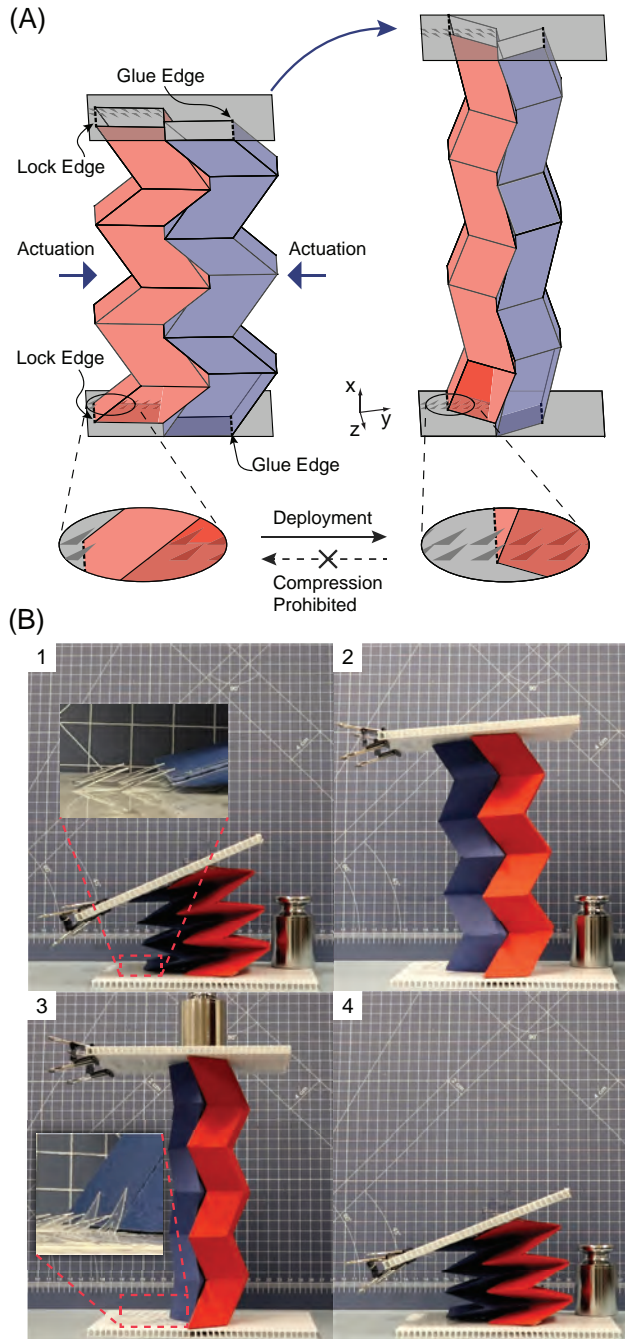


Figure 2.12: Self-locking of the zipper-coupled tube. (A) A tube at 72% extension is deployed to 95% extension by squeezing the sides. Panels on the ends are locked into one-way inclined ridges that are bonded onto the rigid plates. The lock edge is parallel to the glued edge. (B) Corresponding experimental photos of the deployment and locking. The tube is: 1) at the initial state; 2) deployed and locked at around 70% extension; 3) deployed and locked at around 90% extension, and a mass of 500g is supported on the top; 4) retracted to the initial state by releasing the locking ridges from the tube edge. The inserts show the locking ridges at the initial state (1) and a deployed state (3). See Movie S4.

## 2.5 Concluding remarks

This chapter introduces a concept for using origami tubes as deployable and adaptable energy-absorbing devices. Experimental and numerical studies of the deployable tubes demonstrate the tunable characteristics. Locking the tubes changes the system from being elastically deployable, to becoming stiff structures that require crushing to compress longitudinally (9 times stiffer for a tube at 72% extension). Axial quasi-static experiments of the tubular structures made from polyester sheets demonstrate that the stiffness, system forces, and energy absorption all increase as the system is deployed. The quantitative increase of these properties is non-linear with respect to extension of the system. Numerical simulations of the crushing are in reasonable agreement with the experimental results. Both studies show similar values for the force-displacement characteristics and the overall system trends with respect to the extension. The improvement of using the locked zipper tubes as energy absorbers is verified by comparing the crashworthy behavior with that of prismatic tubes. A numerical parametric study indicates that tubes with fewer segments (fewer panels and folds) will result in more plasticity throughout the structure resulting in higher energy absorption and peak forces. These results demonstrate the importance of effectively locking the thin sheet structure to absorb energy through crushing. Structures with six segments have an optimal balance when comparing the total energy absorption to the peak force. For these systems it is important to lock both ends of the tube, while locking only one will provide only about a third of the energy absorption. A parametric study on the design of the planar tube geometry showed that the vertex angle can control the nonlinearity of the relationship between energy absorption and extension, or in other words how tunable the system is. Another parametric study on the planar geometry suggests that the energy absorption increases with the panel aspect ratio, where a short and dense tube will crush with more plasticity. Given a low-energy impact, a set of experimental dynamic drop test show that the tubes can offer different levels of buffering when locked at different extensions. Finally, a physical model based on the zip-tie mechanism is introduced to demonstrate self-locking of the tube after deployment.

In comparison with the conventional thin-walled tube of identical material cost, the proposed zipper tube shares similar loading responses as those of other origami energy absorbers [32, 36]: lower peak force and more energy absorption. Moreover, the zipper tube also owns the potential to tune the energy-absorbing behavior by deploying to different extensions. For vehicle applications, we expect the deployable energy absorbers can work with speed sensors that detect the incoming collision. Generally, the absorbers should be deployed to a longer extension for a higher speed, to absorb as much impact energy as possible. For a relatively lower speed, the absorbers should be deployed to a shorter extension to reduce the peak force. A set of sensors, decision making methods, and control algorithms will be required to effectively implement and use the active energy

absorption.

The work presented here is a proof-of-concept for the deployable and adaptable energy-absorbing systems and is thus limited in nature. First, innovation and improvement is needed in the materials, design, and scalable fabrication of the deployable origami tubes [17]. Next, it is important to resolve methods for rapid deployment mechanism to allow real time responsive behavior. An inflatable bladder within the origami tubes [19] driven by a chemical reaction similar to an airbag could be suitable for rapid deployment and tuning. Using fabric-polyester for fabrication can increase the life-span robustness [69]. Calculation of the energy absorption per unit volume versus density would enable the comparison to other materials, using the standard Ashby map [70]. We are hoping that we can create a mechanism in the future, enabling the tunable locking and deployment of the system.

The following videos can be found in <https://shorturl.at/cfsY5>

**Movie S1.** Cyclic quasi-static test of a zipper tube with 95% extension. The video is shown 16 times faster than the actual speed.

**Movie S2.** Drop test of cylinders containing water shown at 40 times slower than the actual speed. The left tube has an extension of 52% and the right has an extension of 95%. The tube with less deployment has lower stiffness and results in almost no splash back of the water, whereas the tubes with larger deployment results in 1.5cm splash back

**Movie S3.** Drop test of raw eggs shown at 40 times slower than the actual speed. The left tube has an extension of 52% and the egg on the right sits directly on the vertical slider. The tube can protect the egg from this drop.

**Movie S4.** Self-locking of a zipper-coupled tube with the zip-tie mechanism. The tube is deployed and self locked to multiple extensions. It supports a mass of 500 g when locked at around 90% extension.

## CHAPTER 3

# Bending Stability of Corrugated Tubes with Anisotropic Frustum Shells

The flexible drinking straw, or bendy straw, can change its orientation over the tube length via local snap-throughs. While it has been mass produced for decades, the geometric influences on the bending multi-stability have not thoroughly investigated. In this chapter, to explore how the bending stability is affected by geometry, we extend and verify a elasticity-based bar and hinge model for curved-crease origami. We discuss the geometric influences from both the longitudinal and the cross-sectional aspects, and find out the energy behaviors behind the global stability. This work has been published as: [Wo, Z. and Filipov, E. T., Bending Stability of Corrugated Tubes With Anisotropic Frustum Shells, ASME. J. Appl. Mech. 89\(4\): 041005. doi:10.1115/1.4053267.](#)

### 3.1 Introduction

Snap-through instabilities of elastic shells offer a novel method to create reconfigurable structures and geometrically adaptable systems. Recent studies have explored the underlying mechanics of different elastic shell geometries [37, 71, 72, 73], and research has also harnessed their instabilities for different morphological applications [74, 75]. Among common geometries, the open-top conical frustum shell can be inverted to generate non-trivial stable configurations [76]. In their most popular implementation, open-top frusta are arranged in an opposing fashion to create a functional corrugated tube commonly known as the bendy or flexible drinking straw (Fig. 3.1). This corrugated system allows for morph-and-lock features with both axial and rotational deformations. A full inversion of the frustum can axially shorten the corrugated tube while a partial inversion can allow for global rotation. The separate frusta can undergo different inversions, allowing for versatile shape morphing over the length of the corrugated tube.

Corrugated tubes made of open-top frusta have found practical applications beyond the simple drinking straw. The same principles are used to create bain circuits [77, 78], hoses for transporting

liquids and gases [43, 44], and covers for moving equipment [79]. The ability to elongate, shorten, and adaptively bend allows this subset of corrugated tubes to conform to different shapes, move into new configurations, and to connect points in otherwise hard to navigate environments (e.g. within the human body or a car engine). Furthermore, the corrugations increase the stiffness of the tubes for external out-of-plane loads and increase the capacity for the tubes to resist orthogonal flattening or crushing. Recently, these corrugated tubes of open-top frusta have also been investigated for novel applications in engineering. The axial bi-stability of the multiple successive frusta in the tube has been used to create energy absorbing and adaptable metamaterials [20, 80], and the bending adaptivity has been proposed for use in creating versatile origami-inspired finger grippers and crawling robots [21]. Bending bi-stability of the frusta allow the tube to be reconfigured to arbitrary 3D space curves, which opens the door for transdimensional deformations [42].

Despite the long history of practical applications with bending straws [48], the underlying mechanics of these systems have not been explored in much detail, especially with respect to the bending stability. The work by Zhang explored partial inversions of single open- and closed-top frusta under lateral point loads [76]. The work evaluated critical forces and the bi-stable transitions through experiments and a series of parametric studies on the geometry of the frusta. A different study by Bende et al., explored the bending stability of two opposing frusta (a unit cell of a corrugated tube) under a downward load placed non-axially at the edge of the frusta [41]. For a limited set of geometries, the work showed that internal pre-stress or overcurvature is necessary to achieve a stable bent state. Furthermore, their work showed that cones with higher slope and/or height are needed to achieve bi-stable bending. The previous studies, however, have had several limitations. They have only explored a limited set of geometries and have not evaluated the influence of the “crease” which connects two separate conical frusta. From the experimental perspective an extensive parametric study has not been feasible for the large number of geometric parameters, as it would require a large number of samples and testing time. In the previous studies, the partial inversions were activated by non-axial point loads, to investigate the stability behavior of a single frustum rather than of a corrugated tube consisting of multiple frusta. While this loading mode was easy to achieve experimentally, it differs from the practical use of flexible bending straws which would typically experience bending moments. Finally, while the properties of circular frusta have been partially explored, cross-sectional influences on the bending stability have not been studied in previous work. Our work in this paper will give insight to these additional topics of interest.

The chapter is organized as follows. Section 3.2 describes the geometry of the corrugated tubes, the adapted bar-and-hinge method used for simulations, and the four-point bending set-up used to explore bending bi-stability. In Section 3.3, the bending stabilities of circular cross-sections are explored, and a simple mechanism is used to explain the underlying mechanics of the system. Section 3.4 evaluates the bending stability of modified cross-sections and gives insight to how

cross-section anisotropy, concavity, and non-symmetry can influence the stable configurations and energy landscape. Physical models with orthotropic bending stabilities are presented in Section 3.5. A discussion and conclusion addressing the findings, limitations, and potential extensions is presented in Section 3.6.

## 3.2 Geometry and model

### 3.2.1 Geometric parameters and cross-sections

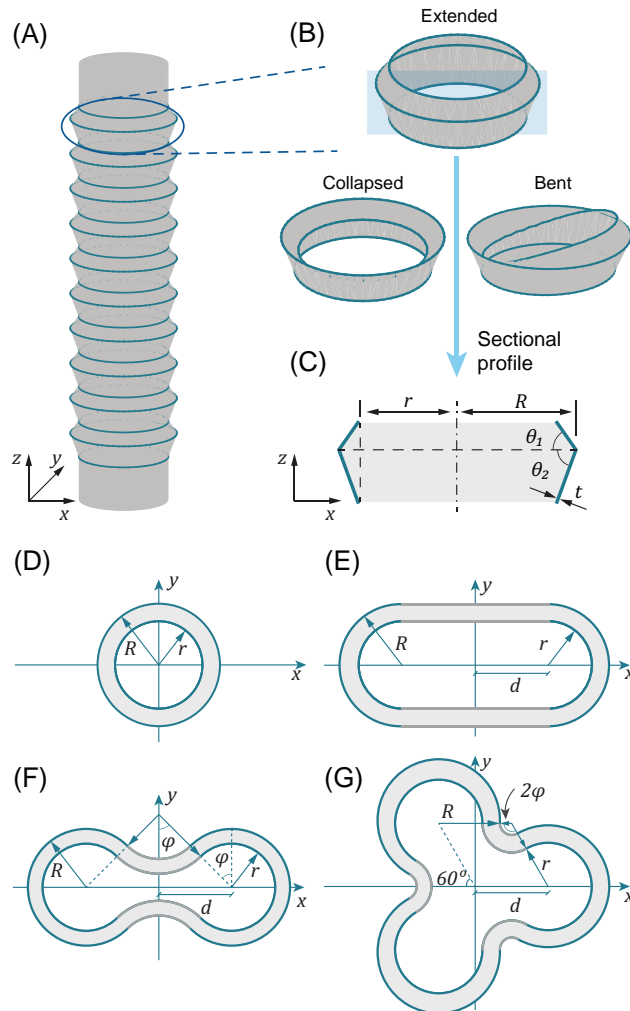


Figure 3.1: Geometry and cross-sections of the corrugated straw. (A) A straw with ten unit cells. (B) A unit cell in three configurations: extended, collapsed, and bent. (C) The longitudinal section can be defined by five independent parameters. (D) Circular cross-section. (E) The track shape with  $d/r = 1.1$  (F) The dumbbell shape with  $d/r = 1.1$ ,  $\lambda_\varphi = 1.8$ . (G) The three-leaf clover shape with  $\lambda_\varphi = 1.8$ .

A typical instance of the bendy straw is composed of repeating units, where each unit cell consists of two different frusta that are connected by a crease line (Fig. 3.1A). In certain instances, the unit cell can snap between two axial stable states (Fig. 3.1B), extended and retracted, through a full inversion of the top frustum [20, 41]. This type of axial bi-stability allows a straw to deploy, and to maintain configurations at multiple lengths [20]. Another type of possible bi-stable behavior is through a partial inversion of the top frustum, which can provide continuously-varied bending configurations for the straw, and here is referred to as bending stability [41].

The shape of the straw will depend on the longitudinal geometry of the unit cell (Fig. 3.1C) and the shape of the tube cross-section. The longitudinal shape can be defined by the following five parameters: slant angles of (1) the top ( $\theta_1$ ) and (2) the bottom ( $\theta_2$ ) frusta, the radius of (3) the outer ( $R$ ) and (4) the inner ( $r$ ) edge, and (5) the shell thickness ( $t$ ). The slope of the bottom frustum  $\theta_2$  is greater than  $\theta_1$  to avoid self-intersection during full inversion of the top frustum in axial compression [41]. Furthermore,  $r$  must be identical for all units in a multi-cell straw (Fig. 3.1A) because each unit must be connected to its adjacent unit via the inner edge. While in principle the other four parameters can be varied independently for each unit cell, we assume they are constant for the entire corrugated tube. To constrain our study to classical straw structures similar to those studied in [20, 41, 76], we set the ratio of the outer to inner radius to be  $R/r = 1.15$ , and the angle of the bottom frustum to be  $\theta_2 = 70^\circ$ . The outer radius is set to 31 mm. We then normalize the thickness with the outer radius as  $t/R$ . The normalized thickness ( $t/R$ ) and the slant angle of the top frustum are systematically varied to explore the geometric influence on stability.

In addition to the longitudinal unit-cell parameters, the shape of the cross-sections can also affect the bending stability. The circular cross-section allows for a consistent mechanical behavior in all bending directions, but does not allow for a geometrically programmable response in different directions. Therefore, the additional cross-section variations are introduced to expand the parameter space for exploring and programming bending behaviors. Top views of all four types of cross-sections are shown in Fig. 3.1D-G. From the cross-sectional perspective, a conventional circular unit cell is defined with only two radii  $R, r$  (Fig. 3.1D). A direct modification can be proposed by moving two semi-circles away from the origin horizontally by a distance  $d$ , and connecting them with straight lines of length  $2d$  (Fig. 3.1E). Mathematically, the equation for the upper part of the inner edge can be written as the following:

$$y = \begin{cases} \sqrt{r^2 - (x + d)^2} & x \in [-d - r, -d] \\ r & x \in [-d, d] \\ \sqrt{r^2 - (x - d)^2} & x \in [d, d + r] \end{cases} \quad (3.1)$$

The bottom half is the reflection of the top half over the X axis. The equation for the outer edge is

formulated by replacing  $r$  with  $R$  in the above definition, thus a gap of  $R - r$  is created consistently around the entire cross-section and the angles  $\theta_1$  and  $\theta_2$  remain uniform as well. This cross-section variant is named as the *track shape* for its overall similarity to the running track (Fig. 3.1E). The circular and the track shape cross-sections share a common feature where both are enclosed by curves on the side and there are no negative curvatures along the cross-section.

Next, to explore a cross-section with a negative curvature, we modify the track shape by squeezing the central part of the track shape. A sketch of the modified shape is shown in Fig. 3.1F, and the upper half of the cross-section is described by the following equation:

$$y = \begin{cases} \sqrt{r^2 - (x + d)^2} & x \in [-d - r, -d + r \cdot \sin \varphi] \\ \frac{d \cdot \cot \varphi +}{\sqrt{(d \cdot \csc \varphi - r)^2 - x^2}} & x \in [-d + r \cdot \sin \varphi, d - r \cdot \sin \varphi] \\ \sqrt{r^2 - (x - d)^2} & x \in [d - r \cdot \sin \varphi, d + r] \end{cases} \quad (3.2)$$

where  $\varphi$  is the angle of the negative curved region. The bottom half of the cross-section is the reflection of the top half over the X axis. Here, the size of the negatively-curved arc is defined by introducing a variable  $\lambda_\varphi$ . This variable then defines the angle  $\varphi$  of the negatively-curved region as shown in Eq. 3.3

$$\varphi = \begin{cases} \arcsin\left(\frac{d}{r}\right) / \lambda_\varphi & d < r \\ \frac{\pi}{2} / \lambda_\varphi & d \geq r \end{cases} \quad (3.3)$$

The parameter  $\lambda_\varphi$  serves a similar role to “a radius of curvature” in defining the negatively curved region in the dumbbell shape. The shape becomes a track shape when  $\lambda_\varphi \rightarrow \infty$ , and the curvature of the negatively-curved region increases as  $\lambda_\varphi$  decreases. The equation for the outer edge is formulated by replacing  $r$  with  $R$  in Eq. (3.2), and a consistent gap of  $R - r$  is created. The definitions in Eq. 3.2 and Eq. 3.3 are chosen such that we obtain a smooth transition from the negatively curved region to the adjacent semi-circles. This shape is named as *dumbbell shape* because of its similarity to a physical dumbbell.

The dumbbell shape has a unique negatively-curved part as compared to circular and track shape, but all three of these cross-sections share a common property: symmetric bending axes, i.e., bending along opposing directions yield identical responses when the bending axis is determined. Many variations can break up the symmetry and one of them is inspired by three-leaf clovers. The

$$\left\{ \begin{array}{l} x = d + r \cdot \cos \alpha, \quad y = r \cdot \sin \alpha \quad \alpha \in [0, \pi/3 + \varphi] \\ \\ x = d + \left( \frac{\sqrt{3}}{2} d \cdot \csc \beta \right) \cdot \cos \left( \varphi + \frac{\pi}{3} \right) + \left( \frac{\sqrt{3}}{2} d \cdot \csc \beta - r \right) \cdot \cos \beta \quad \beta \in [4\pi/3 - \varphi, 4\pi/3 + \varphi] \\ \\ y = \left( \frac{\sqrt{3}}{2} d \cdot \csc \beta \right) \cdot \sin \left( \varphi + \frac{\pi}{3} \right) + \left( \frac{\sqrt{3}}{2} d \cdot \csc \beta - r \right) \cdot \sin \beta \\ \\ x = -\frac{d}{2} + r \cdot \cos \gamma, \quad y = \frac{\sqrt{3}d}{2} + r \cdot \sin \gamma \quad \gamma \in [\pi/3 - \varphi, 2\pi/3] \end{array} \right. \quad (3.4)$$

*clover-like shape* (Fig. 3.1G) has the rotational symmetry of order 3 and the angle of rotation is  $120^\circ$ . The shape is constructed by rotating a  $120^\circ$  segment two times, and the base segment is expressed by the parametric equation 3.4, where  $\varphi$  is calculated using Eq. (3.3). The outer edge is then defined by substituting  $R$  into Eq. (3.4), and the gap remains  $R - r$ . This cross-section requires negative curvature such that there is a continuous curved transition between the three separate segments.

---

Parameter	Meaning
$R$	Radius of the outer edge of the circular cross-section
$r$	Radius of the inner edge of the circular cross-section
$\theta_1$	Slant angle of the top frustum in a unit cell
$\theta_2$	Slant angle of the bottom frustum in a unit cell
$t$	The frustum shell thickness
$d$	Distance between each semi circle and the centroid in the track shape
$\varphi$	Half of the opening angle of each negatively-curved region in the dumbbell shape and the clover shape
$\lambda_\varphi$	The controlling coefficient for $\varphi$

---

Table 3.1: Geometric parameters of the corrugated tube

### 3.2.2 The numerical method

The bar and hinge model is a reduced-order simulation tool that has been used to approximate the loading response of thin-sheet structures, based on their global geometry and material properties [67, 81]. The model can provide a rapid approximation of nonlinear mechanical behaviors with much less convergence issues than with conventional finite element models (discussed later in this section). The model was originally developed for analysis of straight-crease origami structures [82], and has been recently modified to simulate arbitrary sheets and origami with curved creases [83, 84]. The bar and hinge model was carefully examined under various loading modes, and the predictions are in good agreement with those of theory, FE simulation, and experiments [83, 84]. Curved crease origami is geometrically and physically similar to the open top frusta explored in this work. In the bar and hinge model, the thin-sheet structure is discretized into nodes, bars, and hinges (Fig. 3.2A). There are three different elements for the main deformation behaviors: (1) straight bars that capture in-plane stretching and shearing, (2) bending hinges that capture out-of-plane bending of the sheet, and (3) folding hinges that capture rotations of the creases that connect separate sheets. The stiffness of each of the above three elements are derived based on linear-elastic material properties and mesh geometry [84]. Here we use  $Y = 1300$  MPa,  $\nu = 0.45$  for Young's modulus and Poisson's ratio, based on typical properties of isotropic and homogeneous polypropylene (PP) [76]. The straw geometry is discretized into triangular segments based on a metric called the aspect ratio,  $\alpha$ , which describes the length to width ratio of the segments and thus controls the density of the mesh [84]. For each triangular segment, the aspect ratio  $\alpha$  is defined as the ratio of the side length perpendicular to the fold,  $H$ , to the side length roughly parallel to the fold,  $W$  (Fig. 3.2A). A larger aspect ratio  $\alpha$  results in a finer mesh discretization. As compared to the finite element method, it takes much less time to run simulations with the bar and hinge model, due to the fewer degrees of freedom. Prior work using the bar and hinge model to simulate thin sheet structures has successfully approximated the stiffness and deformation behaviors of different corrugated sheet structures [83, 84].

The folding hinges that connect the separate frusta shown in Fig. 3.2A will experience a bending during the deformation, but a precise description of their stiffness is not available yet. Thus, for a crease line of length  $L_f$ , the stiffness is approximated by the following equation based on previous works [67, 84, 85]:

$$k_f = \frac{L_f}{L^*} \cdot \frac{Yt^3}{12(1 - \nu^2)} \quad (3.5)$$

Complicated behaviors affecting the folding stiffness are simplified into a single, case-specific parameter, called the length scale factor  $L^*$ . This factor is found to be a linear function of the sheet thickness [68]. Given that the thickness  $t$  is normalized by  $R$  for a scalable analysis without

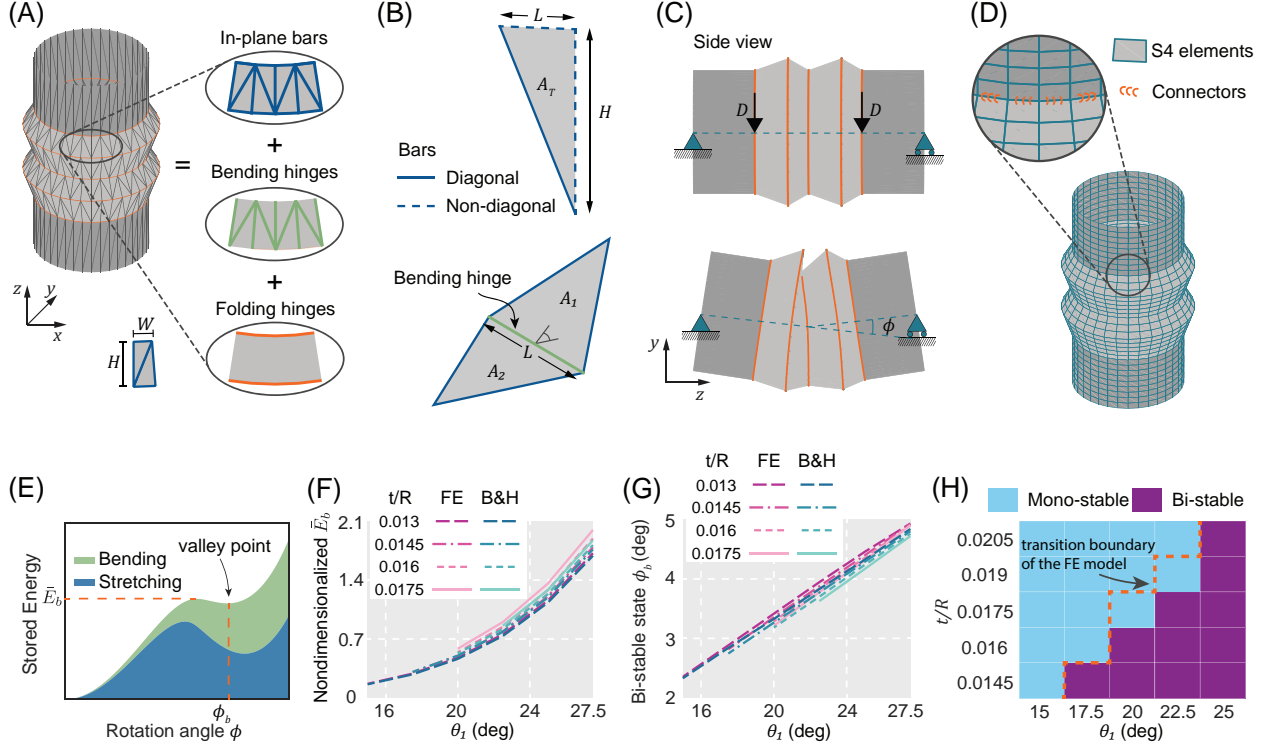


Figure 3.2: The bar and hinge model and calibration. (A) Decomposition of the bar and hinge model, where the aspect ratio  $\alpha = H/W$  defines the density of the mesh. (B) One triangular panel with bars (top), and the isometric view of a typical bending hinge that is connected to two triangular panels. (C) Four-point bending setup and a typical deformed state. (D) The finite element (FE) model consists of shell elements and connector elements. (E) A typical bi-stable energy profile when the energy of the crease folding is not considered. The energy barrier is denoted by  $E_b$ , and the stable rotation is  $\phi_b$ . (F) Comparison of energy barriers and (G) the stable rotation states between the FE model and the calibrated bar and hinge model. (H) Stability predictions for twenty five combinations of  $\theta_1$  and  $t/R$ . The FE predictions are slightly different from the predictions with bar and hinge model, but both models show the same trends.

consideration of the folds,  $L^*$  is also normalized as  $L^*/R$  for a fully scalable analysis with respect to folding stiffness. Unless mentioned specifically, in this work we define the folding hinges to have a stiffness of zero ( $L^*/R = \infty$ ) to focus the research on the geometrical influence on the stability behaviors of the thin-shell frusta.

In the bar and hinge model, panel stretching and shearing are represented by straight bars. For a typical triangular panel (Fig. 3.2B), the stiffness of each bar is defined by

$$k_s = \frac{YA_{eff}}{L} \quad (3.6)$$

where  $L$  is the length of the bar. The effective cross-sectional area of the bar,  $A_{eff}$ , represents the

cross-sectional area that is proportional to the panel dimension and the sheet thickness. Based on prior work [84] and calibration shown below, the following stiffness expressions give predictions for the frustum stretching and shearing that match finite element results:

$$A_{eff} = \begin{cases} (0.27\alpha^2 + 0.34) \cdot \frac{A_T t}{L} & \text{Diagonal bars} \\ 0.27 \cdot \frac{A_T t}{L} & \text{Non-diagonal bars} \end{cases} \quad (3.7)$$

The out-of-plane bending stiffness of sheets are lumped into discrete bending hinges. After meshing the structure with bars and hinges, a typical bending hinge is located at the interface of two triangular segments with areas  $A_1$  and  $A_2$  (Fig. 3.2C). The calibrated bending stiffness is

$$k_b = 0.043Yt \cdot \frac{L^2}{A_1 + A_2} \quad (3.8)$$

where  $L$  is the hinge length.

We use a four-point bending test to investigate the bending response of the corrugated tube, and a two-unit straw is chosen because it is the simplest system that allows interactions within units. The potential boundary effect with respect to the number of the units will be discussed in the next subsection. Two stiffer hollow sections are connected to the ends of the straw via creases (Fig. 3.2C, dark area). These sections provide a span between the loading points and the supports. These end sections are set to be  $10^6$  stiffer than the straw so their deformations are negligible in comparison. The two nodes on the left end of the tube that lie on the  $x - z$  plane are restrained in all translational directions (Fig. 3.2C), while the two nodes on the right end (also on the  $x - z$  plane) are only restrained in  $x$  and  $y$  to allow global longitudinal movement of the tube. A displacement controlled simulation is performed by prescribing a downward  $y$ -displacement to the four nodes that connect the frusta to the hollow sections and also intersect the  $x - z$  plane (Fig. 3.2C). Bending about a different axis is realized by rotating the structure about the  $z$ -axis, without changing the criterion of assigning boundary and loading conditions. Total energy is calculated for every increment of the displacement controlled simulation by summing the strain energy in the bars and the hinges. The rotational angle  $\phi$  is computed for every increment.

With the bar and hinge model, the structural stiffness can be overestimated for cases where torsional deformations are present [84]. Because torsion is involved in the bending of the straw corrugation (Fig. 3.2C), a calibration of the model is necessary to obtain reliable results. A finite element (FE) model (ABAQUS/Standard [66]) of the two-unit circular straw is built using shell elements and rotational hinges to provide high-fidelity simulation results for the calibration (Fig. 3.2D). Shells are meshed with S4 general purpose elements, where adjacent frusta are connected

via connector elements with prescribed rotational stiffness to simulate crease rotations (the same stiffness as defined in Eq. 3.5). Each end of the corrugated portion is connected to a cylindrical tube with  $10^6$  higher Young's modulus. In the FE simulation, the bending is simulated by applying the same four-point bending setup and the loading scheme is controlled by the modified Riks method [86]. Linear-elastic material properties are set to be the same as the bar and hinge model. The rotational angle  $\phi$  and the strain energy are computed in every iterations. Convergence with respect to the mesh density is examined, and a mesh size of roughly  $0.03R \times 0.03R$  is chosen because it provides a strain energy prediction that is within 0.2% of a mesh with  $0.015R \times 0.015R$  elements.

Because torsional deformations are expected in the simulations (Fig. 3.2C), an aspect ratio  $\alpha \approx 1$  is used in the mesh of the bar and hinge model as is recommended in [84]. To calibrate the bar and hinge model, the energy profile (Fig. 3.2E) is compared to the FE results to quantify the difference. In order to be consistent with the scalable analysis, the strain energy  $E$  is non-dimensionalized as  $\bar{E} = 10^6 \cdot E/(Y \cdot V^3)$ , where  $Y$  is the Young's modulus and  $V$  denotes the material cost of the corrugated part. The factor of  $10^6$  is included to make the figures that display non-dimensionalized energy more clear. For a bi-stable bending process, the energy profile has an energy barrier  $\bar{E}_b$  and the valley point that corresponds to the stable rotation  $\phi_b$ . Setting the discrepancy of energy barriers  $\bar{E}_b$  and the secondary stable state  $\phi_b$  as the minimizing objectives, the calibration returns stretching and bending stiffness as shown in Eq. (3.7) and (3.8).

With the calibration, a close match of energy barriers  $\bar{E}_b$  (Fig. 3.2F) and the second stable state  $\phi_b$  (Fig. 3.2G) are achieved for  $\theta_1$ 's in the range from  $15^\circ$  to  $27.5^\circ$  and thicknesses  $t/R = 0.013, 0.0145, 0.016, 0.0175$ . The largest relative error of the bar and hinge model for predicting energy barriers when compared to the FE results is 3.8%. The second stable state  $\phi_b$  shows a nearly-linear relationship versus  $\theta_1$ , where the largest error is reported as 3.3%. The energy barrier  $\bar{E}_b$  increases with the  $\theta_1$  (Fig. 3.2F), since more energy input is required for partially inverting a larger frustum. A corrugation with larger  $\theta_1$  achieves the second stable state at a larger magnitude of rotation. The top frustum gets taller and a larger rotation is required to trigger buckling and inversion.

In order to examine the bar and hinge model's accuracy for predicting bending stability of systems with different geometries, twenty five cases with various  $\theta_1$  and  $t/R$  are simulated and compared with the FE results. The stability results are presented in Fig. 3.2H, where the color in each grid shows the stability type of the structure (i.e. mono-stable or bi-stable). Bending stabilities of 92% of the different geometric cases are predicted to be the same with the bar and hinge model and the FE models. Although two cases near the transition boundary between mono- and bi-stability are characterized differently with the two models, the global trends for the stability behavior is the same. This stability map will be discussed in the next section, regarding the stability trends

with respect to  $\theta_1$  and shell thickness. Simulating the twenty five cases with FE took  $\sim 18$  hours, while the same simulations with the bar and hinge model took only 84 minutes. This improved computational efficiency with the bar and hinge model is necessary for the parametric variations in the following sections where we perform hundreds of variations varying the geometries of the systems. The model is still capable of accurately estimating the global behavior of the systems.

### 3.2.3 Boundary effects of the end constraints

In the four-point bending simulation, each end of the corrugated tube is connected to a much stiffer hollow cylinder to provide a span between the loading points and the supports. Although the deformations and strain energies of these hollow sections are negligible as shown in later figures, they introduce stiff constraints on the conical frusta that may alter the loading response. Therefore, corrugated tubes with more unit cells are tested (Fig. 3.3A), and a convergence study on number of units is employed to explore the boundary effect. Here, a force-controlled simulation is implemented using the Modified Generalized Displacement Control Method (MGDCM) [87]. This algorithm is constructed based on the arc length method, and it can accurately follow the equilibrium path after the tangent stiffness becomes negative.

For the four-point bending test with a force control, there will be a nearly flat moment stage between the loading points, with the center moment value denoted by  $M$  (Fig. 3.3B). When the tube deforms, the frusta will snap and the moment value will fluctuate. The relationship between  $M$  and the tube rotation  $\phi$  is illustrated in (Fig. 3.3C) where mono-stable systems will only have positive moments. The moment value of first limit point  $M_p$  is selected to compare the behavior of tubes with different numbers of units. Comparing the energy would be misleading as tubes with more units will experience more deformations and will contain more energy.

To study the convergence behavior,  $M_p$  is found for systems with different number of units, and a relative error of  $M_p$  is computed with respect to a system with  $N = 10$  units. The results show a downward trend in error with respect to the number of units  $N$  (Fig. 3.3D, note the logarithmic y-scale). When there is only one unit in the tube ( $N = 1$ ), one of the nearly-rigid cylinders is directly connected to the inverting frustum, and it undergoes non-negligible deformation when the frustum snaps. The substantial deformation due to the constraint will magnify the bending moment, and the relative error is near 100% for four combinations of different  $\theta_1$  and  $t/R$ . When there are two or more units in the tube, the relative error of  $M_p$  under various geometries is less than 3% (Fig. 3.3D, see insert). Therefore, the boundary effect from the stiff constraints will substantially change the bending response when  $N = 1$ , but it can be reasonably neglected for  $N \geq 2$ . In other sections of this work, the stability of the system is explored using corrugated tubes with  $N = 2$ , based on the balance of accuracy and computational complexity.

Finally, the stability predictions for the same twenty five cases as in Fig. 3.2H, are shown for tube with  $N = 10$  in Fig. 3.3E. For all but two cases on the boundary, the stability type is consistently predicted, regardless of the number of units.

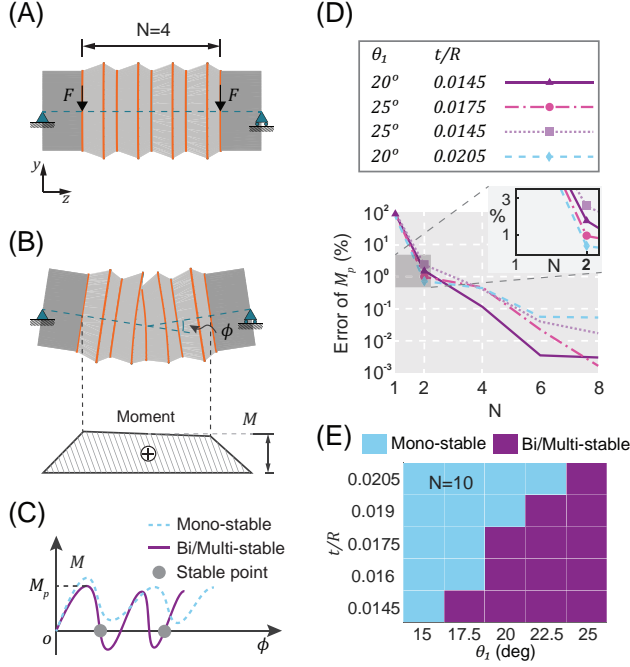


Figure 3.3: Boundary effects of the four-point bending simulation. (A) Four-point bending setup of a corrugated tube with  $N = 4$  unit cells. (B) A typical deformed state and the corresponding moment diagram. The corrugated part is strained by a nearly flat moment stage, where the center moment is of magnitude  $M$ . (C) As the tube rotates, the moment  $M$  will fluctuate to the negative region only for bi/multi-stable cases. The first peak  $M_p$  is selected to explore convergence of the behavior with respect to the number of units. (D) Relative errors of  $M_p$  between tubes with  $N$  units and a tube with ten units. For four tube geometries with  $N = 2$ , the relative errors are less than 3% (the insert). (E) Stability predictions for corrugated tubes of  $N = 10$  unit cells. The predictions are nearly identical to those with  $N = 2$  unit cells, and both show the same trends.

### 3.3 Bending stability of circular cross-sections

#### 3.3.1 Influences of thickness, frusta angle, and crease stiffness

This section focuses on how the bending stability of a corrugation with a circular cross-section can be affected by geometric parameters defining the tube and the stiffness of the crease connecting separate frusta. Figure 3.2C shows that partial inversion of the frustum of a unit cell can be triggered with a certain magnitude of prescribed displacement. The top frustum is heavily deformed, whereas the shape of the bottom frustum stays relatively unchanged, suggest that bending

responses can be affected by the geometry of the top frustum (see Fig. 3.1B, C), i.e., the slant angle  $\theta_1$ . Given a two-unit structure with a circular cross-section ( $\theta_1 = 22.5^\circ$ ,  $t/R = 0.0175$ ), the second stable state is achieved when the tube is rotated by  $\phi_b \approx 3.6^\circ$  (Fig. 3.4A, part 1). The total energy decreases after it reaches the energy barrier  $\bar{E}_b$ , indicating the existence of a second stable state. The bending energy (local bending of the frusta) increases monotonically through the process, while the stretching energy shows a “snap-through” profile, suggesting that some stretching energy is released during the partial inversion. Thus, the stretching of the frusta is essential in having a bi-stable system. The secondary stable state disappears for a smaller  $\theta_1$  (Fig. 3.4A, part 2). In this case, the release of stretching energy becomes smaller than the increase in bending energy, and there is no longer a snap-through.

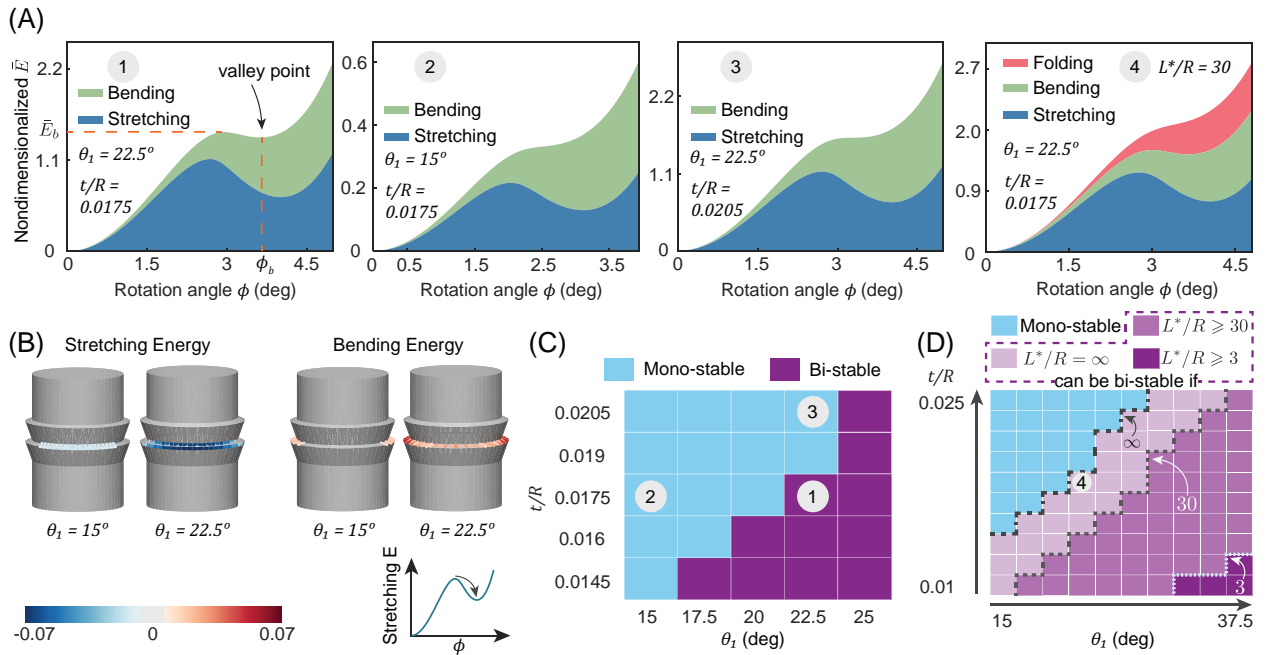


Figure 3.4: Effects of frustum slant angle  $\theta_1$ , shell thickness, and crease stiffness on the bending stability. (A) Energy profiles with different combinations of the above three parameters. The first three cases have zero crease stiffness, while the crease stiffness of case 4 is defined by  $L^*/R = 30$ . (B) Energy redistributions from the peak point to the valley point of the stretching energy curve. The redistribution is presented by plotting the change of energy in bars and bending hinges. The sheet thicknesses are  $t/R = 0.0175$ . The color scale indicates the magnitude of energy change, and the compressive side of the straw is shown. (C) The stability map for twenty five cases of varied thicknesses and slant angles, with zero-stiffness folding hinges. Each grid shows the stability type with different colors for the corresponding case. (D) An expanded stability map with various crease stiffness defined by Eq. 3.5, where the transition boundaries of tubes with  $L^*/R = \infty$ , 30, 3 are marked with dashed lines.

The effects of  $\theta_1$  can be better understood by exploring how energy is redistributed during the

partial inversion process. For case 1 and case 2 in Fig. 3.4A, the change of energy between the peak point to the valley point of the stretching energy curve are shown in Fig. 3.4B. The side shown in Fig. 3.4B is the compression side of the corrugated straw. A straw with a larger  $\theta_1$  has a longer and steeper conical frustum when other parameters are fixed. Compared to the frustum with smaller  $\theta_1$ , such a frustum is heavily deformed, and the panels are stretched to a greater extent. Therefore, the case with  $\theta_1 = 22.5^\circ$  releases much more stretching energy (-2.53 mJ) around the partially-inverted frustum, compared to the case with  $\theta_1 = 15^\circ$  (only -0.44 mJ). In both cases, the redistributions show global increase of bending energy. While the larger  $\theta_1$  induces more gain of bending energy (Fig. 3.4B), the difference of the bending energy gain (2.27 mJ versus 0.86 mJ) is not big enough to counteract the release of stretching energy, so the case with larger  $\theta_1$  is bi-stable.

Another parameter that can affect bending stability is the shell thickness. The ratio of stretching to bending energy decreases as we increase the sheet thickness, because the bending energy scales with  $t^3$ , while the stretching energy is proportional to  $t$ . Furthermore, stretching and bending have counteracting effects on the stability, where only stretching energy contributes to the bi-stable behavior. Thus, when we increase the thickness from  $t/R = 0.0175$  to 0.0205, the total energy becomes monotonically increasing (Fig. 3.4A, part 3 versus part 1). The stability of straws with other combinations of angle and thickness are shown in (Fig. 3.4C) and are characterized as bi-stable and mono-stable. Twenty five cases of straws were investigated, where the frustum angle ranges as  $\theta_1 \in \{15^\circ, 17.5^\circ, 20^\circ, 22.5^\circ, 25^\circ\}$ , and the non-dimensionalized thickness ranges as  $t/R \in \{0.0145, 0.016, 0.0175, 0.019, 0.0205\}$ . The sheet thickness is normalized by the outer radius  $R$ , to make the analysis scalable. The bi-stable domain grows with an increase of  $\theta_1$  and shrinks with an increase of  $t$ , implying that a thinner corrugation with larger slant angle  $\theta_1$  favors bi-stable bending.

The stiffness of the crease lines which connect separate frusta can also affect the bending stability of the system. In part 4 of Fig. 3.4A, a normalized crease stiffness of  $L^*/R = 30$  is added to the structure with  $\theta_1 = 22.5^\circ$ , and  $t/R = 0.0175$  (equivalent geometry to structure with no folding stiffness in Fig. 3.4A, part 1). The energy associated with folding of the crease increases monotonically during the partial inversion process, and makes the system mono-stable. The effect of different crease stiffness on the bending stability of structures with different geometries is shown in Fig. 3.4D. These expanded stability maps show one hundred combinations of  $\theta_1$  and  $t/R$  with three different length scale factors that define the folding stiffness in Eq. 3.5:  $L^*/R = \infty, 30, 3$ . The folding stiffness is zero when  $L^*/R = \infty$ , and the corresponding bi-stable domain reaches the maximum size. The bi-stable domain shrinks as  $L^*/R$  decreases to 30 (meaning a finite folding stiffness). Moreover, only four cases are bi-stable when  $L^*/R = 3$  (a larger folding stiffness). Thus, for a corrugation with a reasonable folding stiffness, bending can only be bi-stable with significantly thinner shells and larger slant angles  $\theta_1$ . In other words, crease stiffness in the cor-

rugation resists bi-stable bending. These results also support the findings on limited geometries in [41]. Those systems had a finite crease stiffness, and only obtained bending stability due to pre-stress. Here we show that with sufficient low folding crease stiffness, bending bi-stability is still possible by tuning the geometry.

### 3.3.2 Verifying geometric and stiffness effects with a simple mechanism model

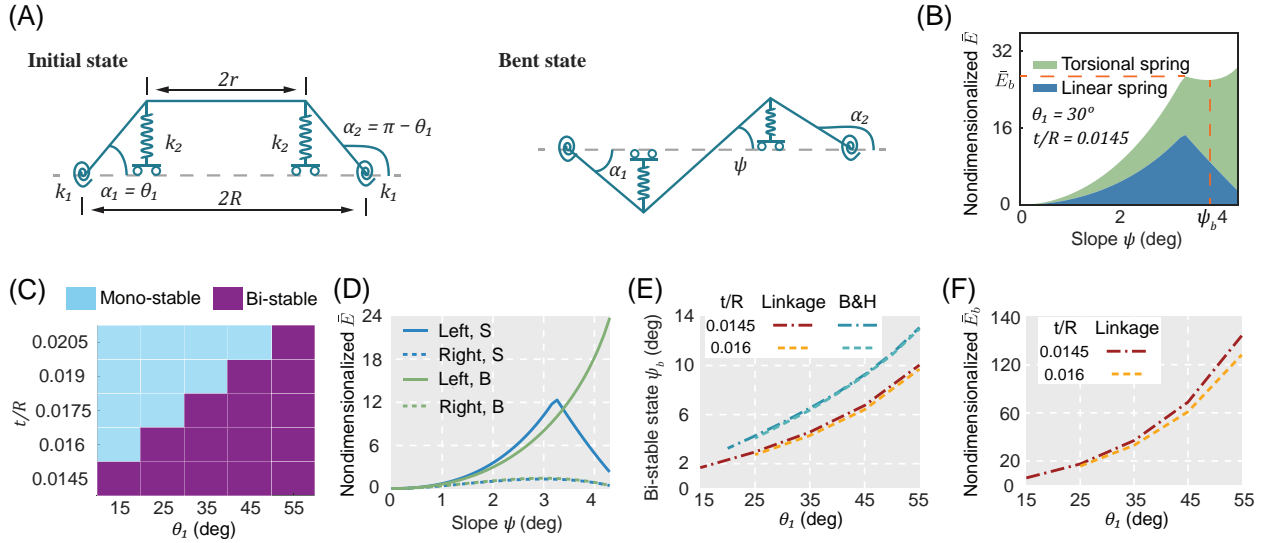


Figure 3.5: Four-bar linkage model that can capture key geometric influences on bending stability. (A) The linkage model in its original configuration, and the bent state via partial inversion of cranks. (B) A typical bi-stable energy profile, where the slant angle is  $\theta_1 = 30^\circ$  and  $t/R = 0.0145$ . (C) Stability map that captures the trend that bi-stable bending is possible with lower thickness or higher slant angle. (D) Energy during the inversion of the left (or compressive) side of the mechanism dominates the total strain energy. S indicates the stretching of the translational springs while B indicates bending of the rotational springs. (E) Bi-stable configurations  $\psi_b$  and (F) Energy barriers  $\bar{E}_b$  both increase with  $\theta_1$ , and only experience a minor influence from the thickness. These trends are consistent with those of the bar and hinge, and FE models.

In this section, we will verify the bending stability behaviors with a simplified mechanism model. The bar and hinge and FE model found that the following features affect bending stability. Bending bi-stability is only possible with partial inversion of the top frustum. The top frustum occupies a larger portion of the entire structure when  $\theta_1$  increases, and there is a higher percentage of released energy. Stretching energy is the driving component for a bi-stable strain energy profile, and it is proportional to the shell thickness  $t$ . In contrast, bending energy increases monotonically during the partial inversion, detracting from possible bi-stability, and the bending energy scales

with  $t^3$ . Therefore, decreasing the thickness  $t$  results in a second stable configuration to be possible for bending. Finally, the contribution of the creases is similar to that of the sheet bending, and creases with higher stiffness will result in less bi-stable structures.

Figure 3.5A shows the simplified planar four-bar linkage model at its initial state. The model consists of a horizontal rigid bar of length  $2r$ , and two crank links with initial angles of  $\alpha_1 = \theta_1$  and  $\alpha_2 = \pi - \theta_1$ . This frustum bending is modeled with two torsional springs (stiffness  $k_1$ ) at the left and right ground supports (Fig. 3.5A). The springs are at a strain-free angle at the initial state, and their stiffness will be formulated to scale with  $t^3$ , to represent relative scaling of bending of the thin sheet. Ground supports are distanced from each other by  $2R$ , corresponding to the span of the outer edge (Fig. 3.1C). Our model is inspired by that shown in [41], however in our implementation, two translational springs are introduced to capture the stretching energy during the inversion. These springs are grounded via roller supports, and their top ends are connected to the top bar and cranks together. Stiffness of the translational spring is denoted by  $k_2$  that will be formulated as a linear function of the shell thickness. The translational springs are strain-free at the length given by the initial configuration of the linkage model. As the mechanism approaches the inversion, the lengths of the springs go to zero (maximum strain energy), and after inversion, the length of the springs increase again (releasing strain energy). The initial state of the full mechanism is a stress-free stable configuration, corresponding to the extended state of a unit cell (Fig. 3.1B). A bent state through partial inversion of the crank links (Fig. 3.5A), refers to the bent state of the straw structure in Fig. 3.1B. However, in the bent state, the springs will contain some strain energy, thus the stability needs to be confirmed.

To search for a bent stable state, the slope  $\psi$  of the top bar is incrementally increased to study the energy of the mechanism. The slope  $\psi$  is smaller than the rotational angle  $\phi$  of the bar and hinge model because  $\phi$  summarizes deformations from all frusta in the two-units structure. For a given  $\psi$ , the model configuration can be calculated by the following geometric constraints:

$$\begin{aligned} 2R + W \cdot \cos \alpha_2 &= W \cdot \cos \alpha_1 + 2r \cdot \cos \psi \\ W \cdot \sin \alpha_1 + 2r \cdot \sin \psi &= W \cdot \sin \alpha_2 \end{aligned} \tag{3.9}$$

where the  $W = (R - r)/\cos \theta_1$  is the crank length. The corresponding strain energy in the mechanism is:

$$\begin{aligned} E = &\frac{1}{2}k_1 \cdot [(\alpha_1 - \theta_1)^2 + (\pi - \theta_1 - \alpha_2)^2] + \\ &\frac{1}{2}k_2 \cdot [(W \cdot |\sin \alpha_1| - W \cdot \sin \theta_1)^2 + \\ &(W \cdot |\sin \alpha_2| - W \cdot \sin \theta_1)^2] \end{aligned} \tag{3.10}$$

The relationship of  $E$  versus  $\psi$  can thus be plotted to investigate the stability of the system, as well as characteristic values including energy barriers  $\bar{E}_b$  and the stable state  $\psi_b$  (Fig. 3.5B). The parameter space of the linkage model is  $\{R, r, k_1, k_2\}$ , and  $\theta_1$  as the initial value of  $\alpha_1$ . The ratio for  $R/r$  are the same as with the other analyses, and  $\theta_1$  is varied in a broader range, from  $15^\circ$  to  $55^\circ$ . The stiffness of the translational springs is set to be  $k_2 = kt$  as a linear function of the shell thickness, where  $k$  takes into account the material property and the frustum dimensions that are irrelevant to  $t$ . While the choice of  $k$  affects the energy magnitude, it does not affect the stability prediction, the bi-stable configuration, nor the trend of the energy barrier, thus  $k$  can be arbitrary number for our formulation. The torsional stiffness  $k_1$  is determined by  $k_2 = k_1/(\xi \cdot t^2)$ , where the  $t^2$  complements dimensional difference between bending energy and stretching energy. The coefficient  $\xi$  determines the relative stiffness of stretching to bending.

The energy is non-dimensionalized as  $\bar{E} = E/(kt^3)$ , so the stiffness parameter  $k$  can be eliminated from the energy expression. A typical bi-stable energy profile with tuned stiffness coefficient is shown in Fig. 3.5B. The energy barrier  $E_b$  and the stable configuration  $\psi_b$  are obtained accordingly. The coefficient  $\xi$  is chosen to be 75 to match the transition boundary in the stability map (Fig. 3.5C) to that of the bar and hinge model. While the stability map does not match Fig. 3.4C exactly, the trends of stability with respect to  $\theta_1$  and  $t$  are captured consistently. The second stable state is possible with a higher slant angle  $\theta_1$  or a lower shell thickness  $t$ .

On the side where the top bar moves down (the left side in Fig. 3.5A), the crank is inverted during the bending process. The translational spring is firstly compressed to zero length, and then released to a longer length afterwards. Correspondingly, the energy in the translational spring first increases then decreases, undergoing a bi-stable transition (Fig. 3.5D). On the same side, the torsional spring is rotated as the slope  $\psi$  increases, resulting in a monotonic increase in the bending energy within the system. The other translational and torsional springs gain and release a minor amount of energy compared to those on the inversion side (Fig. 3.5D). Therefore, the total bending energy is monotonically increasing, and stretching is the driving factor behind the bi-stable profile. Furthermore, these results show that the compression side of the frustum dominates the behavior and determines whether the structure will be bistable. The resulting behavior matches that observed from the FE and bar and hinge simulations, and the findings are further backed up in section 3.4.1.

The influence of  $\theta_1$  can also be better investigated with the simplified model. The length of the translational springs is  $W \cdot \sin \theta_1 = (R - r) \cdot \tan \theta_1$ , which increases faster than the traveling range of the torsional springs (proportional to the  $\theta_1$ ). Therefore, with larger  $\theta_1$ , there is a larger contribution from the translational springs, which increase the relative amount of stretching energy and help achieve the bent stable state. The effect that a lower thickness increases bending bi-stability can also be observed with the simple mechanism model. As the thickness  $t$  is reduced the stretching energy (which is bi-stable) has a larger relative contribution to the total energy than the

bending energy (which increases monotonically). The effect of thickness is also evident from Eq. (3.10), since  $k_1/k_2$  grows quadratically with the thickness ( $k_1/(k_2 \cdot t^2)$  is set to be a constant).

The energy barrier  $\bar{E}_b$  and stable state  $\psi_b$  both increase with  $\theta_1$  (Fig. 3.5E, F), matching the observation from the bar and hinge model (Fig. 3.2F, G). The linkage becomes taller when  $\theta_1$  increases while the width of the top bar is fixed, requiring a larger rotation to reach the stable configuration (Fig. 3.5E). Furthermore, the taller linkage generates longer translational springs, pushing up the energy barriers  $E_b$  (Fig. 3.5F). However, these changes are negligible compared to the effect of  $\theta_1$ . The stable state  $\psi_b$  is smaller than those reported for the bar and hinge model (Fig. 3.5E), because the linkage only represents a single inverted frustum from the two-units corrugation (Fig. 3.2C). The energy barrier cannot be directly compared with the bar and hinge model because the arbitrary parameter  $k$  includes geometric effects not captured by the linkage, and the non-dimensionalization also needs to be different for the two models. Nonetheless, the energy and stable equilibria trends for  $\theta_1$  and  $t$  are captured consistently by the linkage model.

## 3.4 Cross-sectional influence on the bending stability

### 3.4.1 From a circular to an orthotropic cross-section

In order to analyze the effect of the corrugation cross-section on the bending stability, three different variations of cross-sectional shapes are proposed in Sect. 3.2.1. These include a track shape where the circular cross-section is elongated, a further modification to include sides with negative curvature, and an asymmetric cross-section resembling a three-leaf clover. The first cross-section variation that we investigated is the track shape, created by pulling two semi-circles away from the centroid and re-connecting them with straight lines. The parameter  $d$  is the distance between each semi-circle and the centroid. Starting with  $d = 0$  (a circular cross-section), an orthotropic cross-section can be formed by adopting  $d > 0$ . The structure can then be bent about the two perpendicular axes to give different stability characteristics. For the orthotropic case, bending about the Y axis is referred to as “strong axis bending”, while bending about the X axis is “weak axis bending” (Fig. 3.6A). While the circular straw can be bi-stable when bent about any axis, in Section 3.4.4 we will show that for orthotropic shapes, only the strong and weak axes have bi-stable states.

We investigate the bending stability as we increase  $d$  and change the cross-section from isotropic to more orthotropic. Here, two different values of  $d$  are chosen to represent track shapes of different properties:  $d/r = 0.18$  corresponds to a close-to-isotropic shape, while  $d/r = 0.75$  is a cross-section with clear orthotropy. The stability map consisting of 25 models with diverse combinations of  $t$  and  $\theta_1$  show how the bending stability changes with orthotropy. For the strong-axis bending

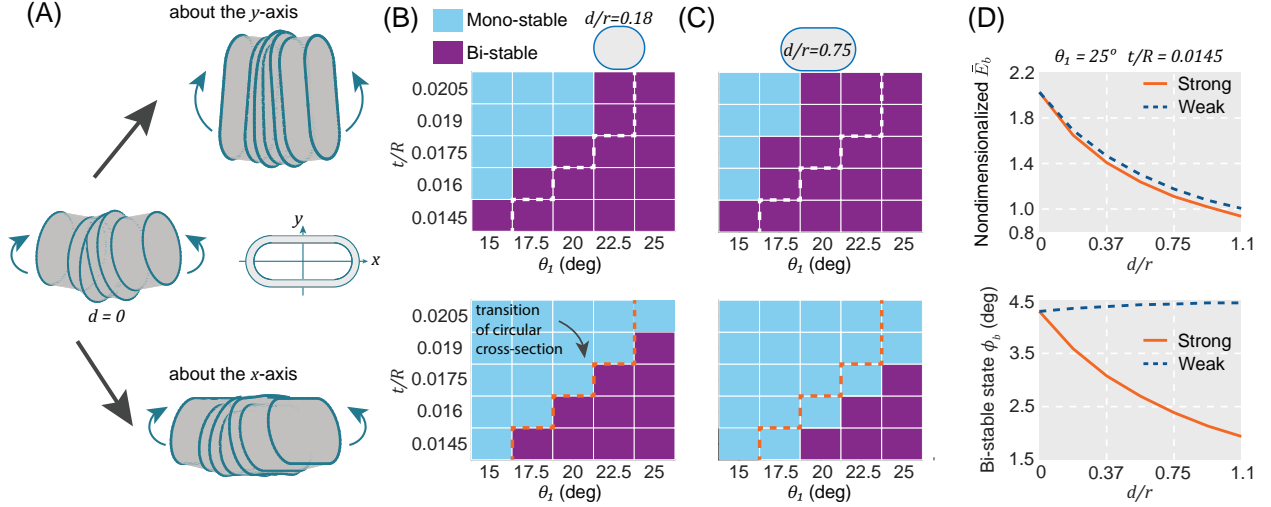


Figure 3.6: Orthotropic bending stabilities of the track shape. (A) Isotropic bending with circular cross-sections turns into orthotropic bending about the strong and weak axis with the track shape. (B) The stability map of the track shape with  $d/r = 0.18$  and (C)  $d/r = 0.75$ . The top row corresponds to the strong-axis bending, and the bottom row corresponds to the weak-axis bending. Transition boundary of the circular cross-section from mono-stable domain to the bi-stable domain is marked with dashed lines. (D) As the distance  $d$  increases, the energy barrier  $E_b$  decreases in both bending directions; the second stable state  $\phi_b$  of the weak-axis bending stays roughly the same, whereas that of the strong-axis bending is decreased.

of the track shape with  $d/r = 0.18$ , the transition boundary from mono-stability to bi-stability moves towards the left and top corner (Fig. 3.6B, top). Compared to circular cross-sections, more combinations of  $t$  and  $\theta_1$  acquire the second stable state by bending about the strong-axis of track shapes. However, bending about the weak axis is bi-stable with less combinations of  $\theta_1$  and  $t$  (Fig. 3.6B, the bottom plot). Those trends are reinforced by increasing the orthotropy with  $d/r = 0.75$  (Fig. 3.6C), where strong-axis bending offers more bi-stable configurations while weak-axis bending offers less. For instance, the model of  $t/R = 0.0175$ ,  $\theta_1 = 20^\circ$  is bi-stable in the strong-axis bending process and mono-stable in weak-axis bending. In summary, when morphing circular cross-sections to the track shape, strong-axis bending will possess a larger domain of bi-stable parameters  $t$  and  $\theta_1$ , whereas the bi-stable domain of the weak-axis bending will decrease.

In addition to the orthotropic stabilities, the energy barriers  $E_b$  and the second stable state  $\phi_b$  also change as the cross-section becomes more orthotropic (Fig. 3.6D). We study the model of  $t/R = 0.0145$ ,  $\theta_1 = 25^\circ$  which remains bi-stable in both bending directions. The energy barrier is the highest at  $d = 0$  (a circular cross-section), and gradually decreases with the distance  $d$  in both bending directions. Compared to the circular cross-section, the strong-axis bending ( $d/r = 1.1$ ) requires less energy input to trigger the second stable state. Energy input to activate bending bi-

stability in the weak-axis direction is about 7% higher as compared to the strong-axis direction. As the cross-section becomes more orthotropic ( $d/r$  rises from 0 to 1.1), the second stable state drops from  $4.3^\circ$  to  $1.9^\circ$  for the strong-axis bending, whereas the weak-axis bending increases only slightly from  $4.3^\circ$  to  $4.45^\circ$ . The decrease in the strong-axis stable state is intuitive. The partial inversion shortens the compressed side of the tube by a finite amount, and this shortening results in smaller rotations for deeper cross-sections (increased  $d/r$ ).

### 3.4.2 Cross-sections with negative curvature

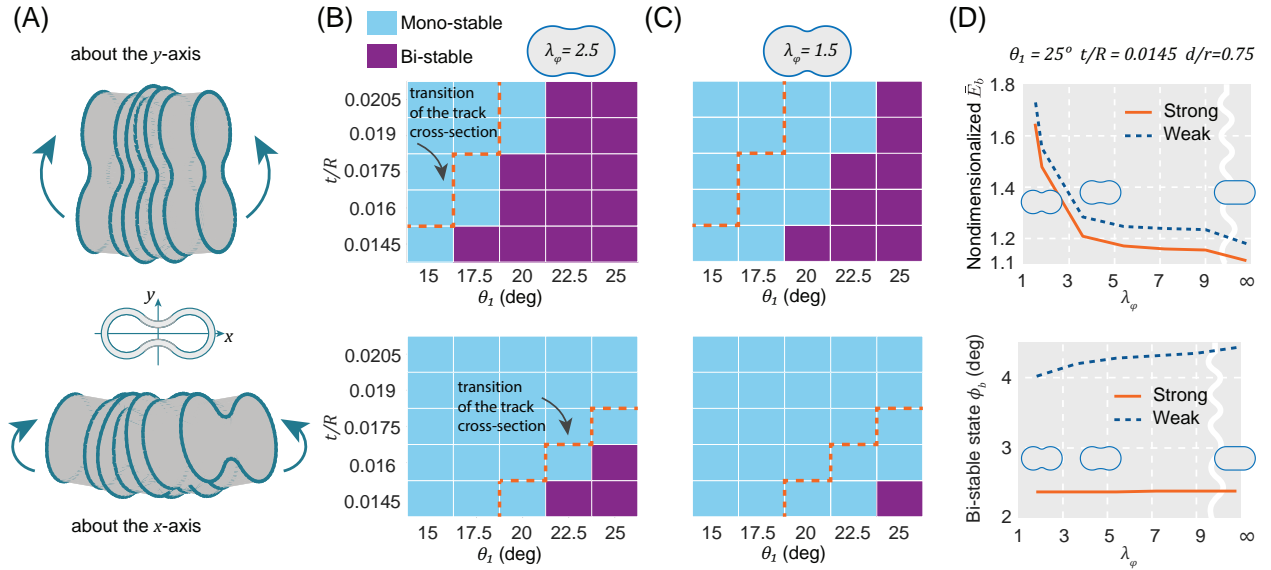


Figure 3.7: Bending stabilities for cross-sections that have negative curvature. (A) The strong-axis and weak-axis bending with the dumbbell shape. (B) The stability map of the dumbbell shape with  $\lambda_\varphi = 2.5$  and (C)  $\lambda_\varphi = 1.5$ . Transition boundary of the track shape of the same distance  $d$  is marked with dashed lines. (D) The dumbbell shape morphs to the track shape as the controlling parameter  $\lambda_\varphi$  increases towards  $\infty$ . For both bending directions, energy barriers  $E_b$  decrease during the process, and the stable rotation  $\phi_b$  stays at the same level.

In Section 3.4.1, we showed that by changing the cross-section into the track shape, the structure can achieve stable rotations with less energy input. The track shape brings orthotropy to the bending of the structure, but the curvature of the cross-section stays non-negative everywhere. Therefore, to explore the influence of cross-section negative curvature, we study the dumbbell shape (Fig. 3.1F) in bending about both X and Y axes (Fig. 3.7A). The negative curvature region is configured by the parameter  $\lambda_\varphi$ . Starting from  $\lambda_\varphi \rightarrow \infty$  (the track shape), the shape does not change linearly with the  $\lambda_\varphi$ . When  $\lambda_\varphi = 2.5$ , the shape has only a small negatively-curved region, but the stability behavior changes substantially with a large portion of the bi-stable domain flipping

into mono-stable for both bending directions (Fig. 3.7B). The transition boundary of both bending axes moves towards the right and bottom corner as  $\lambda_\varphi$  further decreases, and the mono-stable parameter domain is increased when  $\lambda_\varphi = 1.5$  (Fig. 3.7C). Thus, introducing negative curvature into the cross-section prevents the structure from bi-stable bending in both directions. The structure with larger negative curvature region (smaller  $\lambda_\varphi$ ) requires smaller shell thicknesses or larger slant angle  $\theta_1$  to be bi-stable. The stability trend for simple orthotropic shapes observed in Section 3.4.1 remains valid, where the strong axis bending has a larger bi-stable domain.

Energy barriers also increase with the negative curvature in the cross-section, i.e., decrease with the controlling parameter  $\lambda_\varphi$  (Fig. 3.7D). For the strong-axis bending, the track shape of  $d/r = 0.75$  only needs  $\bar{E}_b = 1.11$  to activate the second stable state, whereas the dumbbell shape with  $\lambda_\varphi = 1.5$  requires  $\bar{E}_b = 1.65$ , showing a 50% increase. The weak-axis bending also needs more energy input for the same comparison. The higher energy requirement is due to increased bending in the negatively-curved region as will be discussed in Section 3.4.3. While the energy requirement for bi-stable bending is higher, models with the dumbbell shape achieve the bent stable state at a similar rotational angle  $\phi_b$  as the track shape. For the strong-axis bending, the stable rotation stays at the same level when the cross-section transitions from the track shape to the dumbbell shape. Stable rotation of the weak-axis bending drops slightly from  $4.4^\circ$  to  $4^\circ$ .

### 3.4.3 Cross-sectional effects on the energy distributions

The cross-sectional influence on the bending stability can be explained by examining the energy redistribution within the structure, as it undergoes a bi-stable transition. In Fig. 3.4B, we showed that a corrugation with larger  $\theta_1$  can release much more stretching energy during the partial inversion, making the total energy to be bi-stable. Both the simulation and the linkage model suggest that the compression side dominates the energy behaviors. Figure 3.8 shows the energy redistributions around the compression side, from the peak point to the valley point of the stretching energy curve. The redistributions of stretching and bending energy are plotted for three different cases: the strong-axis bending of the track shape (A and D); the weak-axis bending of the track shape (B and E); and the strong-axis bending of the dumbbell shape (C and F). Among all three cases, only the strong-axis bending of the track shape is bi-stable. When comparing strong- to weak-axis bending (Fig. 3.8A to B), there is a much larger release of stretching energy in the strong-axis case (-1.84 mJ versus -0.87 mJ). In the strong-axis bending, material on the compression side has a high confinement within the curved region, which leads to the much higher energy change (Fig. 3.8A). In the weak-axis bending, there is less confinement, and stretching energy is only released near the curved region. The amount of bending energy redistribution does not change much between the strong and weak directions (1.68 mJ versus 1.43 mJ), and thus the weak direction becomes

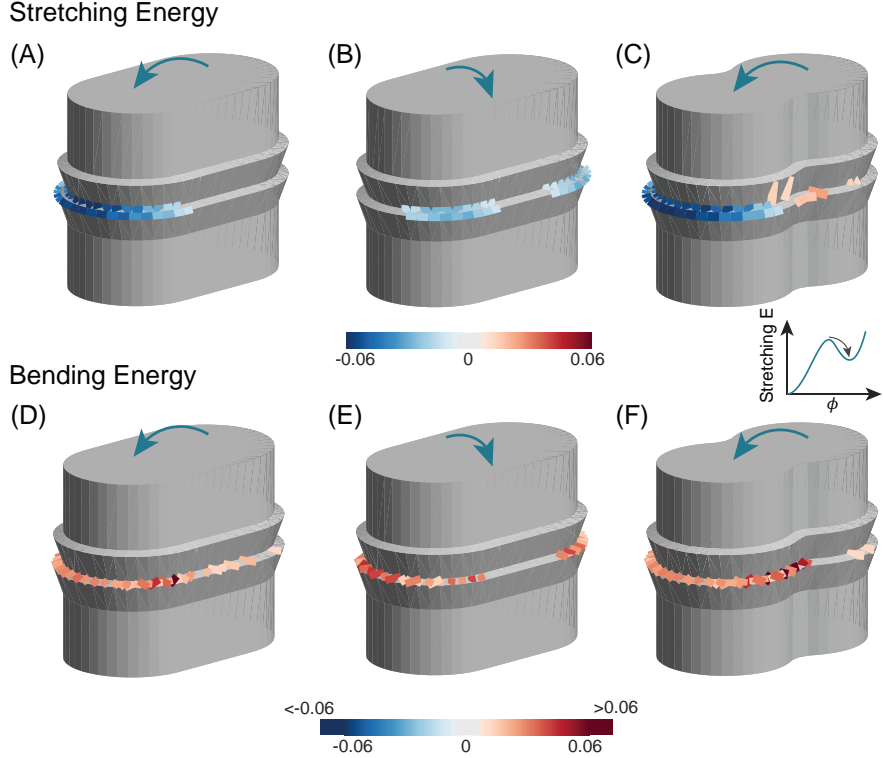


Figure 3.8: Redistributions of stretching (top row) and bending energy (bottom row) from the peak point to the valley point of the stretching energy curve. From the left to the right: strong-axis bending of the track shape, weak-axis bending of the track shape, and strong-axis bending of the dumbbell shape. The outer radius  $R$  is fixed to be 31 mm, and the other parameters are:  $d/r = 0.75$ ,  $\theta_1 = 20^\circ$ ,  $t/R = 0.019$ , and  $\lambda_\varphi = 1.5$ . The color scale indicates the magnitude of the energy change. The limits of the color scale of the bending energy are trimmed to be the same as the stretching energy, and any magnitude that exceeds the range is plotted using the threshold color. The energy is shown for exaggerated bar and hinge elements, with elements near zero energy staying hidden.

mono-stable.

As shown in Fig. 3.7, negative curvature in the cross-sections resists bi-stable bending. For cross-sections with negative curvature, while the bars on the positively-curved region have confinement and release energy, the bars around the concave area (middle of the cross-section) will gain some stretching energy during the partial inversion (Fig. 3.8C). Thus the release of stretching energy in the cross-section with negative curvature gets slightly lower (-1.74 mJ) due to the gain near the concave area. The concave area also shows a higher increase in bending energy, as compared to the track shape (Fig. 3.8F versus D). Because there is less stretching energy released and more bending energy gained (2.3 mJ), negatively-curved cross-sections are more likely to be mono-stable.

### 3.4.4 Energy landscapes for the orthotropic shapes

For a specific bending axis, the directional valley point of the energy profile (Fig. 3.4A) is identified as the second stable configuration  $\phi_b$ . Unlike the circular cross-section, the two orthotropic shapes exhibit non-uniform energy profiles for different bending directions. The valley point (Fig. 3.4A) of a specific direction can be unconditionally stable only if the valley energy is the local minima among those of the neighboring directions, and such a direction is the so called *stable bending direction*. Therefore, stable bending directions can be identified by locating local minima of the energy function for bending directions and rotations  $\phi$ . Models with the track shape and dumbbell shape are bent along all directions that are denoted by polar axes (Fig. 3.9A, B), and bending axes are perpendicular to the associated directions. The cross-sections with  $d/r = 0.9$ ,  $\theta_1 = 30^\circ$  and  $t/R = 0.01$  are selected so that all directional energy landscapes are bi-stable. The negative curvature controlling coefficient for the dumbbell shape is set to be  $\lambda_\varphi = 1.8$ .

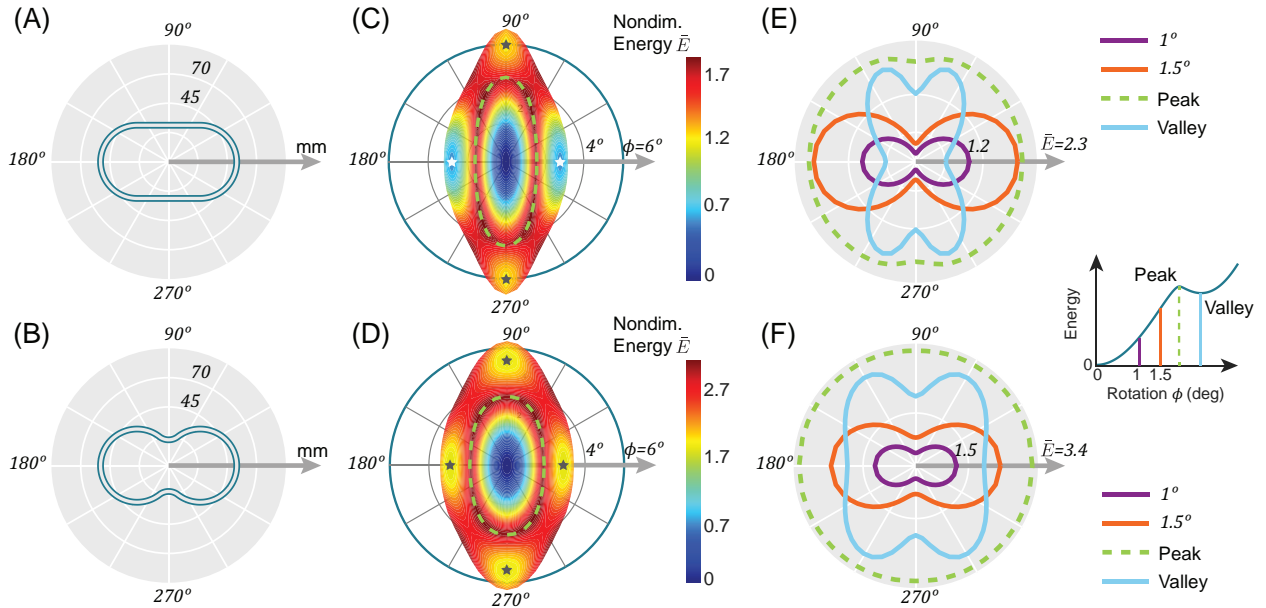


Figure 3.9: Energy behavior of bending the orthotropic cross-sections in different directions. (A) The track-shape cross-section and (B) the dumbbell-shape cross-section are bent along all the directions in the XY-plane. (C) Energy landscapes of the track shape and (D) the dumbbell shape, where the distance from the centroid represents rotation  $\phi$ . Four local minima of energy are marked with pentagrams, and the rotations at which the peak energy is achieved are denoted with the green dashed lines. (E) Strain energy magnitude for the track shape and (F) the dumbbell shape at specific rotations:  $\phi = 1^\circ, 1.5^\circ$ , and the peak and valley of the directional energy profiles. The peak energy is nearly-identical for all directions, while valley energies show four local minima.

For both shapes, strain energies for all bending directions are plotted in a polar coordinate system (Fig. 3.9C, D). The distance from the centroid represents the rotation  $\phi$  in degrees, and

the magnitude of energy is distinguished by colors. Among all the bending directions, valley points of the strong-axis ( $0^\circ$  or  $180^\circ$ ) and the weak-axis ( $90^\circ$  or  $270^\circ$ ) possess the smallest strain energy in their neighborhood. Therefore, the structure is unconditionally stable in these four bent configurations. If the structure is bent about one of the non-primary directions (e.g.,  $45^\circ$ ), it will still pass over a peak load, and will ultimately settle in one of the four bent stable states (Fig. 3.9 C, D).

The four stable configurations can also be found by plotting the energy magnitude for the different directions at specific rotational angles (Fig. 3.9E,F). Distance from the centroid in Fig. 3.9E, F represents the magnitude of energy, and different lines represent different levels of rotation. For rotational angles of  $\phi = 1^\circ, 1.5^\circ$  which are before the peak point, the strong axis gives the largest strain energy for the rotation, corresponding to the highest bending rigidity. At valley points, the strain energies of the strong axis and of the weak axis are lower than those of their nearby axes, suggesting again that these two axes give the unconditionally stable states. The peak energy (energy barrier  $\bar{E}_b$ ) for all directions is plotted with a green dashed line, and the overall shapes are close to circular. For the track shape, the shortest distance from points on the peak energy curve to the centroid is  $\bar{E}_b = 1.89$ , and the largest distance is  $\bar{E}_b = 2.0$ , only 5.8% different. For the dumbbell shape, the largest difference among all energy barriers is only 1.3%. The computed circularities of both peak-energy distribution curves are greater than 0.99 (1 for a circle), implying a high isotropy of the peak energies, despite the orthotropic bending behaviors. This means that roughly the same amount energy input is needed to activate bi-stable bending in all directions, regardless of the direction in which the system is loaded.

### 3.4.5 Non-symmetric bending

Orthotropic bending is possible with the track shape, and dumbbell shape cross-sections, where bending along opposing directions returns identical responses. Therefore, a clover-like shape is introduced as a cross-sectional geometry to explore non-symmetric bending (Fig. 3.1G). To identify stable bending directions, a two-unit corrugation with the clover cross-sections is examined by bending along all directions (Fig. 3.10A). The structure is defined by choosing  $\theta_1 = 40^\circ$ ,  $t/R = 0.01$  and  $d/r = 1.5$ ,  $\lambda_\varphi = 1.5$  to ensure all directional energies have bi-stable profiles. A tube with the clover shape cross-section is expected to exhibit different behaviors when bending along the  $0^\circ$  or the  $180^\circ$  directions, while the behavior of bending along  $90^\circ$  and  $270^\circ$  directions should be identical.

Strain energies for all bending directions are plotted against rotational angles  $\phi$  (Fig. 3.10B). The distance from the centroid represents the rotation  $\phi$  in degrees, and the energy magnitude is differentiated by the different colors. The strain energy contours shows a rotational symmetry of

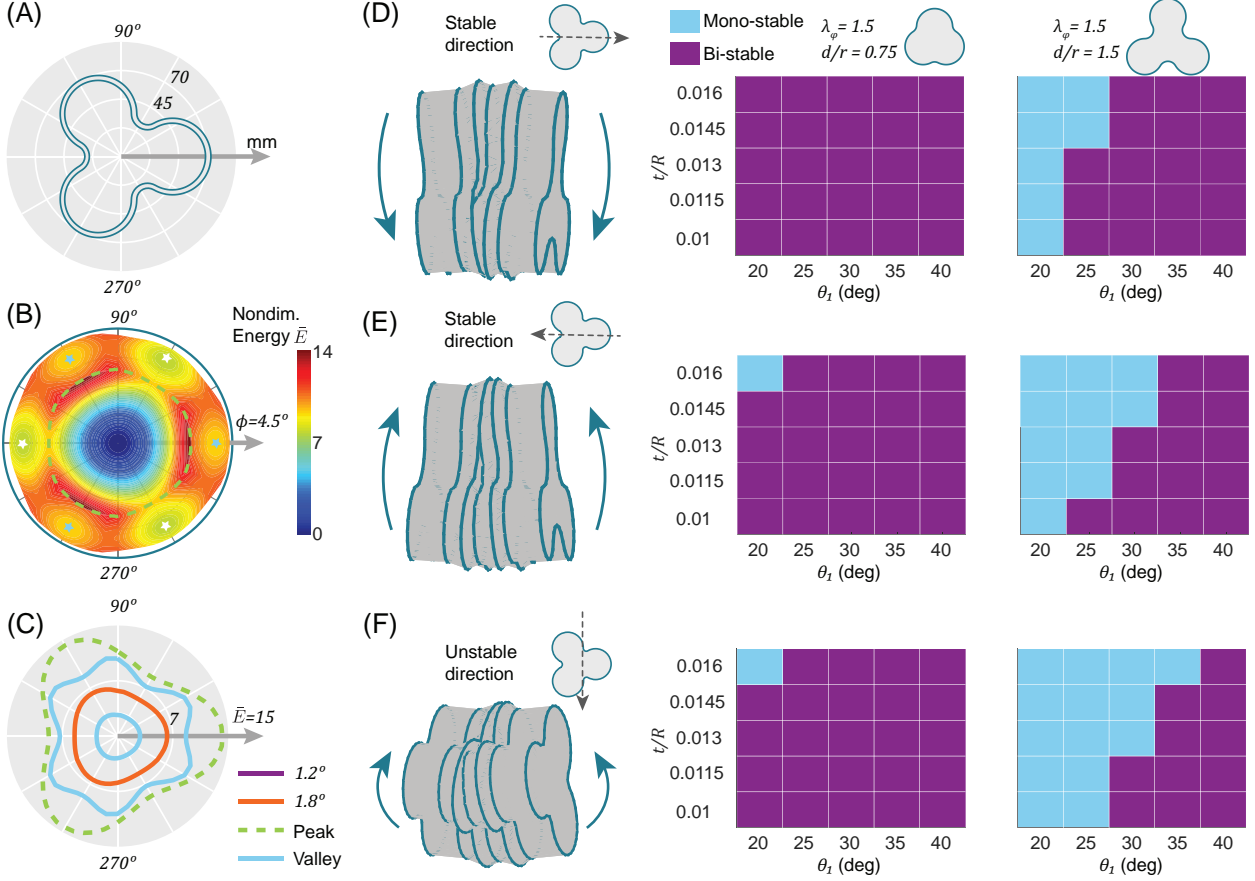


Figure 3.10: Energy behaviors and stabilities of the clover cross-section. (A) The two-units structure with cross-sections of the clover shape is bent along all directions in the XY-plane. (B) Energy landscape has six local minima and they are marked with pentagrams. Peak-energy rotations are denoted with the dashed line. (C) Strain energy magnitude at specific rotations:  $\phi = 1.2^\circ$ ,  $1.8^\circ$ , and the peak and the valley of directional energy profiles. (D) Stability map for the clover shape with  $\lambda_\varphi = 1.5$  and different  $d/r$  ratios, when bending along two unique stable directions  $0^\circ$ , (E)  $180^\circ$ , and (F) the unstable direction  $90^\circ$ .

order 3, inherited from the symmetry of the clover shape. Bending along  $0^\circ$  and  $180^\circ$  direction are both bi-stable, but the  $0^\circ$ -bending has a higher energy barrier and valley energy (Fig. 3.10B). Valley points of the above two bending directions are also local minima of the strain energy function, suggesting that these are unconditional stable states. Thus the  $0^\circ$  and  $180^\circ$  directions are two stable bending directions, and rotational symmetry gives additional groups of stable directions:  $120^\circ$ ,  $300^\circ$  and  $60^\circ$ ,  $240^\circ$ . The other bending directions, for example  $90^\circ$  or  $270^\circ$ , do not have a local minima, and unrestricted bending in those directions would lead the structure to settle into one of the two nearby unconditionally stable states (e.g.,  $60^\circ$  or  $120^\circ$  for the  $90^\circ$  bending).

The stabilities and symmetry of the bending directions can also be recognized by plotting the strain energies at specific deformation states (Fig. 3.10C). For specific rotations of  $\phi = 1.2^\circ$ ,  $1.8^\circ$

which are before the peak energy, directional strain energy grows with the bending depth. Bending along the stable directions of  $60^\circ, 180^\circ, 300^\circ$ , one has to overcome the smallest peak energy of  $\bar{E}_b = 9.4$ . The opposite directions have the largest peak energy of  $\bar{E}_b = 14.4$ , which is 53% larger. Comparing to the nearly-isotropic energy barriers of the track and dumbbell variants, the clover shape shows a bigger difference among directional energy barriers. Strain energy of stable directions  $60^\circ, 180^\circ, 300^\circ$  slightly decrease to  $\bar{E}_b = 7.85$  (only a 16.5% decrease) at the valley, while these of their opposite directions drop by 30% to  $\bar{E}_b = 9.36$ . The valley energy curve in Fig. 3.10C also confirms that there are six stable directions, where the valley energies are local minima within their neighborhood.

Following the identification of stable bending directions, we explore the effects of the clover cross-section on the bending bi-stability with respect to geometric parameters: slant angle  $\theta_1$  and shell thickness  $t/R$ . We define the clover cross-section with a controlling coefficient  $\lambda_\varphi = 1.5$ , and we evaluated two values of the  $d/r$  ratio. We then explore the behavior for three directions of bending including: the  $0^\circ$  (Fig. 3.10D) and the  $60^\circ$  (Fig. 3.10E) directions which we know provide unconditionally stable states, and the  $90^\circ$  (Fig. 3.10F) direction which can have a bi-stable energy curve, but not an unconditional stable state. For the range of  $\theta_1 \in \{20^\circ, 25^\circ, 30^\circ, 35^\circ, 40^\circ\}$  and thicknesses  $t/R \in \{0.01, 0.0115, 0.013, 0.0145, 0.016\}$ , all cases are bi-stable for bending in the  $0^\circ$  direction when  $d/r = 0.75$ . When the ratio  $d/r$  is increased to 1.5, there are a few less bi-stable bending cases for this direction (Fig. 3.10D). Bending in the direction of  $180^\circ$ , however, shows smaller domains of bi-stable parameters for both  $d/r$  ratios (Fig. 3.10E). These results show that, without switching the bending axis, some structures can be bi-stable in one direction of bending, and mono-stable if the bending direction is reversed (e.g.  $\theta_1 = 25^\circ$  and  $t/r = 0.13$ ). Bending in the perpendicular direction ( $90^\circ$ ), which is unstable based on the directional energy analysis, is more sensitive to the distance ratio  $d/r$  (Fig. 3.10F). Among all twenty five combinations of  $\theta_1, t$ , almost all cases have a bi-stable energy curve with a smaller distance ratio  $d/r = 0.75$ . However, the number of bi-stable combinations drops significantly as the distance ratio increases to  $d/r = 1.5$ . For all three directions, increasing  $d/r$  ratios is a negative factor on the bending bi-stability, and the bi-stable domain shrinks with an increase in the  $d/r$  ratio. The result here is similar to that of the orthotropic shape with negative curvature. While the distance of the clover leafs increases, the shape with  $d/r = 1.5$  has more negative curvature in the cross-section which leads to less bi-stability.

### 3.5 Physical models with folding stiffness

This section describes physical models with the conventional circular and the track cross-sectional shapes made from paper sheets that serve as proof of concepts for some of the bending

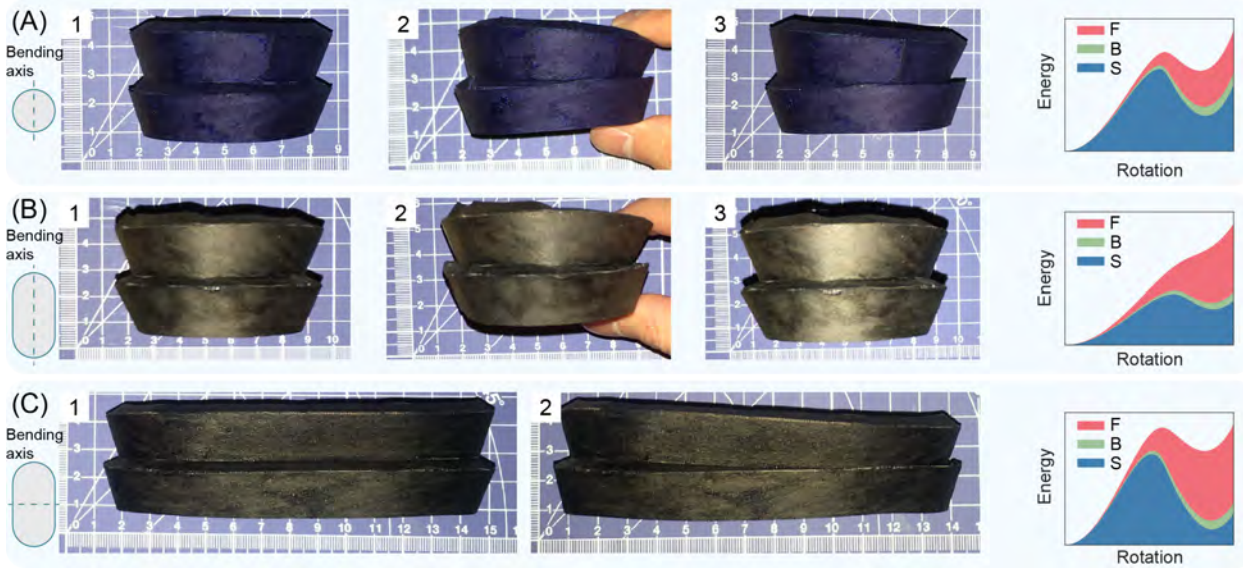


Figure 3.11: Physical models with non-zero folding stiffness and simulated results of the bar and hinge model with  $L^*/R = 3$ . (A) The paper model with circular cross-sections can stay at the bent state. (B) The model with the track-shape cross-sections bent about the weak-axis and (C) the strong-axis. The weak-axis bending is mono-stable while the strong-axis bending stays at the second stable configuration. Their stabilities are predicted correctly using the same stiffness parameter as the circular case.

bi-stability behaviors (Fig. 3.11). Each of the specimens is created to have two unit cells to capture the interactions between cells (Fig. 3.2C). For each frustum, the planar projection is input into a CAD software and a paper sheet is cut using a laser cutter (Universal Laser VLS6.60). Each planar cut of the frustum has extra tabs for connecting them to the adjacent frustum to form a single unit cell. The same  $R/r$  ratio is used as in Sect. 3.2.1, where  $R = 31$  mm and  $r = 27$  mm are used for the paper models. The top frustum angle  $\theta_1$  is chosen as  $30^\circ$ , and  $d/r = 0.9$  is selected for the track shape. The paper sheets are 0.25 mm (0.01 in) thick, and the normalized thickness is  $t/R = 0.008$ . The bar and hinge model is employed to investigate strain energy profiles.

The folding stiffness of the creases connecting frusta cannot be treated as zero, since the connection tabs have a finite value of crease stiffness. After calibration with respect to bending stabilities,  $L^*/R = 3$  is chosen to generate consistent predictions for all three bending cases in Fig. 3.11.

Here, three bending cases are studied: 1) circular cross-section; 2) the weak-axis bending of the track shape, and 3) the strong-axis bending the track shape. Starting from the initial state at which all unit cells are extended, these models are deformed by applying compression on one side of the system by hand (Fig. 3.11). After releasing the applied pressure, the model with circular cross-sections can stay at the deformed state, implying a bi-stable bending behavior (Fig. 3.11A). The weak-axis bending of the track shape of  $d/r = 0.9$  returns to the initial configuration and is

mono-stable (Fig. 3.11B), whereas the strong-axis bending can maintain the bi-stable deformed configuration (Fig. 3.11C). The corresponding energy profiles for the three bending cases simulated with the bar and hinge model predict the stability consistently, using a  $L^*/R = 3$  to model folding stiffness (Fig. 3.11). These results confirm that for certain track shape geometries strong-axis bending can retain bending bi-stability, while the system becomes mono-stable for weak-axis bending.

Fabrication using paper models can introduce secondary effects that influence the bending stability and which are currently not explored with the bar and hinge simulation. Bending flat sheets to curved surfaces will introduce pre-stress that was previously found to be relevant to the bending stability [41]. The fabrication of the paper models may also introduce local defects, or introduce plasticity within the system. While our physical models demonstrate the effect of the geometry, we have not been able to investigate the influence of these secondary effects. We expect future research can give more insight to how such physical properties of the frusta effect the bending stability.

### 3.6 Concluding remarks

Thin-walled corrugated tubes made from open top frusta can allow for multi-stable global bending through partial inversions of their constituent cells. The capability to bend adaptively allows the tubes to conform into different configurations and to connect points in harsh environments. However, the bending bi-stability is not guaranteed for all corrugated tube designs. In this work, we investigate how the bending stability is affected by the cross-sectional geometry of the tubes and the different parameters that define the frusta.

We introduce and use a simplified bar and hinge model to capture the global behavior of different corrugated tubes. This model provides rapid and reasonably accurate predictions of the behavior with few convergence issues, which makes it well suited for the extensive parametric studies performed in this work. The bar and hinge model is calibrated and verified with respect to a more detailed, but much slower FE model. To understand and verify the most notable bending stability behaviors, we also explore representing the frusta using a simple four-bar linkage model where the sheet stretching and bending are represented intuitively. Finally, a physical paper model demonstrates how the bending stability of the corrugated tubes can be programmed by the cross-sectional geometry.

For tubes with a circular cross-section, we find that a stable bending state can be achieved with higher conical angles of the top frustum, thinner shells, and a lower stiffness of the creases that connect separate frusta. All three measures increase the relative amount of stretching energy to bending and folding energy. Stretching energy is the only one that has a bi-stable profile, and is

the driving component for achieving stable bent states of the tube.

Next, we investigate how the cross-sectional shape affects the bending stability. We first modify the circular cross-section by moving two semicircles away to create a track shape, and then we create a dumbbell shape by squeezing the sides of the track shape. These doubly symmetric shapes can only achieve bent stable states in the two orthogonal directions. We show that bending bi-stability becomes more common for the strong axis bending as we increase the depth of the cross-sections. When the track shapes are bent about the strong axis, the inverted region is curved and more confined so more stretching energy is released to cause a bistable bending. In contrast, for weak axis bending the inverted region is elongated with less stretching and reduced bi-stability. This anisotropic behavior of the track shape is confirmed with simple paper prototypes. Increasing the concavity of the cross-section in the dumbbell shape leads to more mono-stable behavior for both directions of bending. The bending energy which increases monotonically becomes concentrated around the negatively-curved region, and counteracts the release of stretching energy to make the strain energy profile mono-stable. To further explore anisotropic bending, we evaluate a clover cross-section that can have six stable bending directions with different stability behaviors when bending in opposing directions.

This chapter gives an understanding to the geometry driven bending stability of thin-walled corrugated tubes and can inform future design of these systems to achieve desired multi-stable behaviors. We have characterized the stable bending angles which can be used to design reconfiguring multi-unit corrugated tubes that bend into desired complex shapes. The orthotropic cross-sections have distinct directional stabilities, which allow for programmable bending with potentially two, three, four, or six stable bending directions that depend on the cross-section design. These systems can be used for tubes with predictable bending paths or robotic components that bend and re-orient in a desired fashion. The geometric design also influences the energy barriers for bi-stable bending, which can be used to design systems that only snap into a bent configuration after a specific force or moment is applied. Corrugated tubes with anisotropic cross-sections offer numerous areas for further research. For example, appropriate fabrication methods for such systems should be explored, and the strength of these tubes for orthogonal loads should be characterized. Given that the corrugated tubes can store fluids, it would also be interesting to investigate how internal pressure changes the stability behavior. The models and concepts introduced in this chapter can be of use to this future research.

## CHAPTER 4

# Tunable Mechanics of the Multi-stable Corrugated Tube with Conical Kresling Pattern

In this chapter, we identify and investigate a unique mechanism based on the buckling of valley creases. This local instability leads to global shape-morphing (referred as "pop-upas well as stiffness tuning. Using a calibrated bar and hinge model, we characterize the bi-stable pop-up deformation and quantify the subsequent stiffness increase.

## 4.1 Introduction

Structural stiffness is of great importance in many engineering applications, and the capability to manipulate the stiffness through a non-destructive way can offer tunable stiffness for novel application in mechanical metamaterials and adaptable structures [88]. Already, stiffness manipulation has been used for applications which are otherwise not achievable through conventional structures, such as the tunable robotic fish that can swim significantly faster [89], a tunable vibration isolator [51], the precise movement of octopus arms based on the localized stiffness tuning [90], minimally invasive surgery using a jamming mechanism with tunable stiffness [91], and a quadcopter frame that can soften during accidental collisions [92]. Among various means of creating tunable stiffness, multi-stable structures naturally offer different stiffness associated with the different stable configurations [19, 93, 94, 95]. The recoverable deformation between stable states is often enabled by elastic buckling of confined beams and thin shells [61, 96, 97, 98, 99]. Such local buckling behaviors help the multi-stable structures to find valuable applications, including reusable energy absorber [61, 100], fast-encapsulating mechanism of flytraps [98], and reversible planar-to-3D transformation [101].

In addition to conceptual designs that have not been mass produced, there is a simple yet effective multi-stable mechanism that has been used in everyday life for decades: the *flexible drinking straw* [48, 102]. The functional portion of the bendy straw is a corrugated cylindrical shell, which

is composed of identical unit cells that are serially interconnected [20, 46]. Each unit cell consists of two opposing frusta that are connected by a crease line (Fig. 4.1A, the insert). In their most common realization, the bendy straw can morph and lock in both axial and bending deformations (Fig. 4.1(A)), allowing for continuous and variable change of orientations over the tube length. Those functions allow the corrugated tube to conform to different shapes [42], and transport fluids and gases [43, 44]. By utilizing their unique shape-morphing and multi-stable features, researchers have deliberately created programmable and reusable energy absorbers [20, 80] and a reconfigurable wire that can fit arbitrary 3D paths [42]. Owing to the wide spectrum of suitable applications, various research has been performed to better understand the underlying mechanics, including the influences of geometry [46], the effects of pre-stress on the multi-stability [41], critical force of the constituent frustum [76, 102], and the dynamics of pneumatic straws [103]. However, the curved surface makes it difficult to fabricate the exact shape as desired, and the conventional molding process for straw-like tubes introduces an uncertain amount of pre-stress [41]. Bernardes and Viollet thus introduced an origami design of the bendy straw that can be constructed without the casting process [104].

Origami, the ancient art of folding paper sheets into complex 3D geometries, has emerged as a predictable and programmable way to create multi-stable structures with tunable properties [1, 11, 30, 105, 106, 107, 108]. The Kresling origami [109] and its derivatives, have been extensively applied into the design of tubular mechanisms for the multi-stability, shape-morphing, and tunable stiffness. Multiple axial stable states allow the Kresling module to be a mechanical memory storage device [50], and the adjustable stiffness can create a tunable vibration isolator [51]. By synthesizing the above three features, the Kresling origami demonstrated its use in achieving complex robotic motions with simple actuation sources, such as the multi-directional deformations [22, 40], crawling robots [33, 110, 111], and a reconfigurable robotic arm with joint-link duality [52]. However, while Kresling-based designs can easily switch between different stable states via twisting motions, typically these tubes cannot bear axial loads. From the mechanics perspective, topology of the panels and creases are determined by the geometry and cannot be changed by deforming among different axial states. The deployment and retraction are guided by antisymmetric twisting motions with identical energy barriers, which implies that the deploying force will simultaneously increase with the load-bearing capacity. Zhai et al. [8] created a Kresling-inspired truss that can bear much higher uniaxial load, while the deployment is flexible. However, such design requires bar members with asymmetric tension/compression behavior and it can only be realized in the form of truss structures rather than origami.

In this chapter, we propose a versatile origami design of corrugated tubes consisting of conical Kresling units that shows drastically different multi-stability with different geometries. More importantly, these systems can be reconfigured into shapes with high load-bearing capacity. The

corrugated tube is inspired by the bendy straw, but instead, the circular frusta are replaced by conical Kresling units to allow for easy fabrication to expand the space of programmable parameters. By tuning the geometry, the tube can behave either like a straw with axial and bending multi-stability, or as a tube that can switch among multiple stable states via a twisting motion. Furthermore, for the latter category, we revealed that another stable state, the *pop-up*, can be achieved through local snap-through buckling of valley creases. When the valley creases are buckled, the Kresling module is turned into a pop-up dome shape with a topologically different arrangement of the panels and creases. As a result, crease folding and the twisting motion both become prohibited. The Kresling module gains high stiffness because the in-plane deformations of panels will be substantially involved in global deformations. Thus, axial and Bending rigidity of the origami corrugated tube are both significantly increased by triggering the pop-up stable state of the Kresling units. This chapter introduces and investigates the properties of the pop-up stability and is organized as follows: In Section 4.2, we introduce the geometric parameters of the Kresling corrugated tube and show different stability behaviors. Using a reduced-order numerical model, we capture and predict the multi-stability of inversion and twisting, as well as the pop-up (Section 4.3). We then present the underlying energy behaviors to understand why the pop-up process can be bi-stable. The shape change is quantified, and the subsequent tuning of the deformation mode is predicted and demonstrated. Section 4.4 investigates the influence of pop-up on the axial and bending stiffness. The pop-up and stiffness tuning are directly related to the origami pattern, and we perform parametric studies to explore how these behaviors are affected by geometric design. The pop-up multi-stability and the tunable stiffness are both demonstrated by paper prototypes. Finally, Section 4.5 provides a discussion on the main findings from this work and presents three conceptual applications based on the tunable properties.

## 4.2 Geometry, global multi-stability, and numerical model

The origami corrugated tube is inspired by the flexible drinking straw (Fig. 4.1A) and the Kresling origami pattern. A typical bendy straw is composed of identical units, where each unit (Fig. 4.1A, the insert) consists of two frusta that are connected by a curved crease. A full inversion of the frustum can axially shorten the corrugated tube (Fig. 4.1A, the right photo), while a partial inversion enables global rotation (Fig. 4.1A, the middle photo). Our design started by mimicking the constituent circular frustum with a origami frustum (Fig. 4.1B), which is constructed using the conical Kresling pattern [29, 112, 113, 114]. By eliminating the need to achieve a curved surface, the complicated molding process and associated pre-stress can be avoided. Here, we do not focus on realizing the straw-like behavior using the origami design, although it can be replicated with appropriate geometries (Fig. 4.1C). Instead, for another set of geometries, we find a "pop-up"

stable state which offers tunable stiffness in both the axial and bending directions. This feature, to the best extent of our knowledge, has not been identified and analyzed in the existing literatures.

### 4.2.1 Geometry definition

The basic unit of the corrugated system presented in this chapter is a single cell that is composed of two origami frusta (Fig. 4.1B). The circular cross-sections are approximated by regular polygons, and the curved shells are broken into flat panels connected by creases. For a single frustum (Fig. 4.1B), the crease pattern is inspired by a triangulated cone pattern that is reported to have multi-stability via twisting motions [29]. The frustum geometry is defined by five independent parameters: the radius of the circumscribed circle of the outer ( $R$ ) and the inner ( $r$ ) edges, the number of sides of the polygon ( $N$ ), the relative twisting angle between the inner and outer polygons ( $\tau$ ), and the slant angle of the frustum ( $\theta_1$ ). In this chapter, we choose the number of sides to be  $N = 6$  (hexagons), and the ratio  $R/r$  to be fixed at 1.55. The two angles  $\theta_1$  and  $\tau$ , will be systematically varied to explore the geometric influences on the pop-up stability and the subsequent stiffness change.

### 4.2.2 Different types of multi-stability

Two origami frusta are connected by creases to form a single unit cell, and a corrugated tube can be created by serially interconnecting several identical unit cells. With different frustum geometries, the origami tubes show different categories of multi-stable behavior. When the frustum is shallow and less twisted, i.e.,  $\theta_1$  and  $\tau$  are small, the tube can undergo a bi-stable inversion (Fig. 4.1B). We fabricate a prototype of a five-unit tube, using  $\theta_1 = 30^\circ$ ,  $\tau = 0^\circ$  and  $\theta_1 = 70^\circ$ ,  $\tau = 0^\circ$  for the top and bottom frusta in the unit cell, respectively. Those values are adapted from the measurements of commercial bendy straw [20], and the resulting corrugated tube can bend and shorten like a straw (Fig. 4.1C, the bottom row). This multi-stable axial inversion and bending can be predicted (Fig. 4.1C, the top row), using the reduced-order simulation tool that will be introduced in the following subsection.

On the other hand, when the frustum is steeper and more twisted, i.e.,  $\theta_1$  and  $\tau$  are greater, the origami frustum can collapse through a bi-stable twisting motion. As shown by the left part of Fig. 4.1D, a frustum with  $\theta_1 = 65^\circ$ ,  $\tau = 50^\circ$  is collapsed to a more compact state via a twisting motion. Notice that, for a frustum in a corrugated tube, there exist two unique effects that cannot be captured by a single stand-alone frustum: i) the confinement from neighboring frusta and ii) the folding of creases that connect separate frusta. Therefore, extra strips of the same material are connected to the edges of the origami frustum to supplement those mechanical effects (photograph in Fig. 4.1D). During the twisting collapse, the folding of creases contributes to the

axial displacement, while the in-plane deformations of the panels generate an energy barrier that separates two stable states [49]. The bi-stable twisting motion can be captured and predicted using an elastic truss model, in which the bars are arranged in the same manner as the crease network.

In addition to the crease folding and the in-plane panel deformations, another mechanism of deformable origami could be considered: the out-of-plane panel bending [67]. For instance, the panel bending is involved in the pop-through defects that create tunable stiffness in the Miura-ori tessellation [11]. Here we adopt a similar strategy to trigger a pop-up state that gains high stiffness. By applying forces and popping the valley creases (Fig. 4.1D), the frustum pops into a different mechanically stable state, which is referred as the *pop-up* state in the following discussions. The localized snap-through buckling of valley creases is reversible because it does not involve plastic deformations of the panels (Section 4.3). After the pop-up, the frustum becomes stiffer by several orders of magnitude (Section 4.4), as the flexible twisting motion is prohibited in the topologically different crease network. The tunable stiffness, combining with the shape-morphing capability, make the corrugated system a suitable candidate for several applications in different areas (Section 4.5).

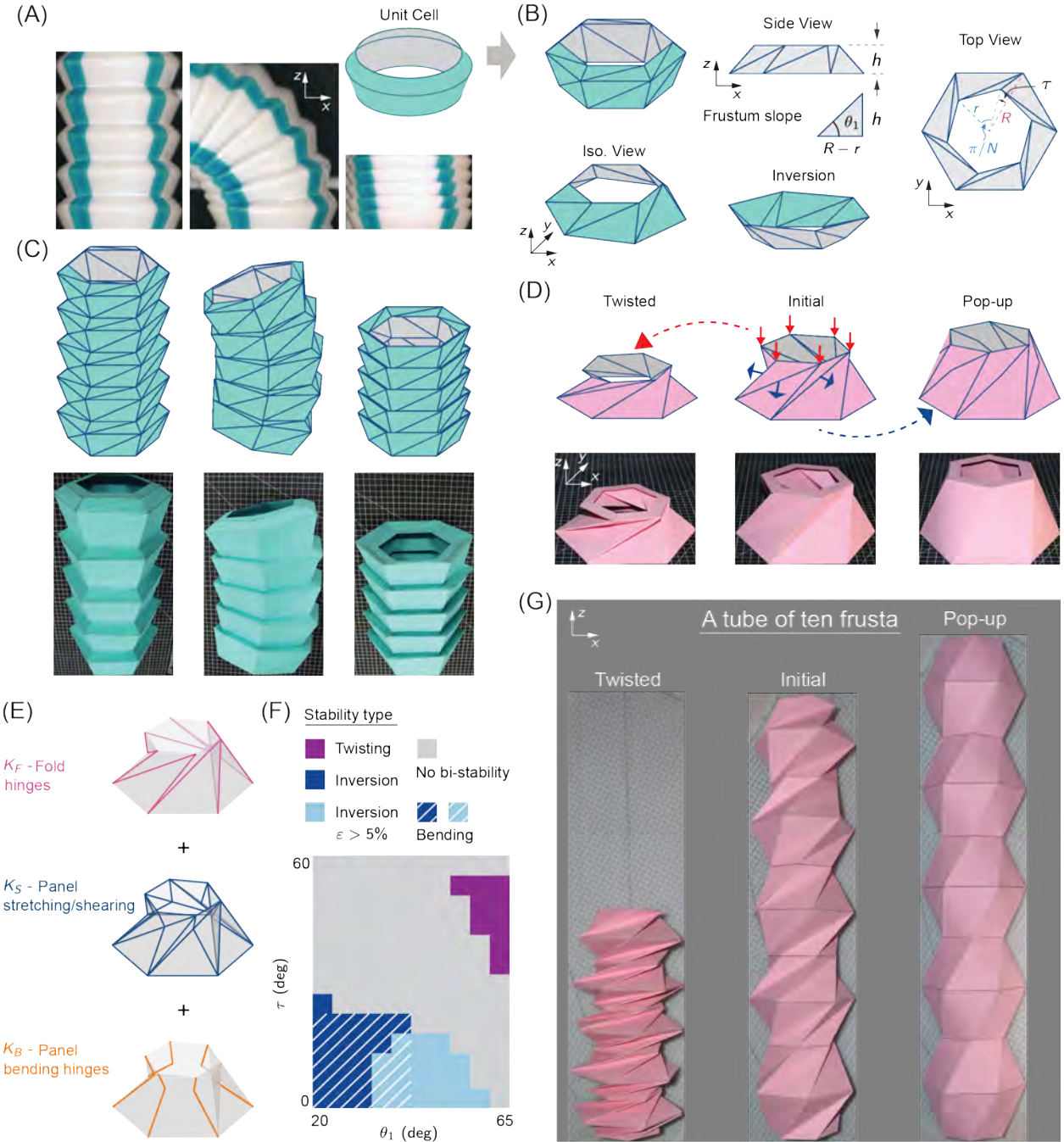


Figure 4.1: Geometry of the Kresling cone and the corrugated tube. (A) A multi-stable straw in its three stable states. (B) An origami unit can be decomposed into Kresling frusta, for which the geometry can be described by the planar views. (C) A Kresling corrugated tube in its extended, bent, and collapsed states, illustrated by computer models (top row) and paper prototypes (bottom row). The two angles are  $\theta_1 = 30^\circ$ ,  $\tau = 0^\circ$  (top frusta) and  $\theta_1 = 70^\circ$ ,  $\tau = 0^\circ$  (bottom frusta). (D) Three stable states of the Kresling frustum ( $\theta_1 = 65^\circ$ ,  $\tau = 50^\circ$ ) shown by computer models (top row) and paper prototypes (bottom row). (E) Three components of the bar and hinge model shown on the single frustum. (F) The numerical predictions of stability for different geometry of the Kresling tube. (G) A ten-frusta corrugated tube showing three types of stable states ( $\theta_1 = 65^\circ$ ,  $\tau = 50^\circ$ ).

### 4.2.3 Numerical model and predictions

We use a bar and hinge model (Fig. 4.1E) to simulate the pop-up process, quantify the shape change, and to investigate the intrinsic tunable properties. The model treats deformable origami structures as pin-jointed truss structures with hinges. Recent advancements allow the model to simulate in-plane deformations and out-of-plane bending, as well as the crease folding, in both straight-crease origami [67, 81, 82] and curved-crease origami [84]. Based on elasticity, the simulation tool is capable of approximating nonlinear large-displacement responses rapidly and reliably, with much less convergence issues than the finite-element (FE) model. It has been carefully verified for various structures, and the predictions are in good agreement with those of analytical formulation, FE simulation, and experiments [46, 84, 115].

In the bar and hinge model, the folding of creases is represented by torsional springs defined along the crease lines, as illustrated in Fig. 4.1E. The out-of-plane bending of panels is also represented using torsional springs that span across the panels, where the exact location will be discussed in Section 4.3. For this triangulated frustum (Fig. 4.1B), the in-plane deformations are captured by bars that outline the perimeter and along the same direction as the bending hinges. For a more in-depth discussion of the formulation and the usage of the model, please refer to [67, 82].

The stiffness matrix of the system is comprised of contributions of the above three components, as well as a penalty term for preventing the contact between adjacent panels [82]. The stiffness of each of the three components is derived based on linear elasticity and the geometry. Here, we use a representative material with Young's modulus  $E = 1.3 \times 10^9$ , Poisson's ratio  $\nu = 0.3$ , and a normalized thickness  $t/R = 4 \times 10^{-3}$ . We use arbitrary units and parameters of realistic relative magnitudes to discover the fundamental pop-up stability and the stiffness change. More details regarding the stiffness formulation, as well as the calibration with respect to finite-element results, can be found in Section 4.2.4.

In order to understand the relationship between the geometry and the category of the multi-stable behaviors, we perform a parametric study with respect to the slant angle  $\theta_1$  and the twisting angle  $\tau$ . In other words, under a specific geometry, we explore whether a tube will exhibit the straw-like multi-stability of bending and inversion, or the twisting multi-stability. As compared to the finite-element method, the running time of the bar and hinge model is several orders of magnitude lower, making it an efficient yet sufficiently precise tool for exploring the parameters in a wide range. Here, we show the stability predictions for evenly-distributed  $\theta_1 \in [20^\circ, 65^\circ]$  and  $\tau \in [0^\circ, 60^\circ]$ , with a gap of five degrees (Fig. 4.1F). The numerical results match the conceptual observations of the paper prototypes, in which a combination of small  $\tau$  and  $\theta_1$  can provide a bi-stable inversion. Under an axial load, the origami frustum will be inverted to a nearly-mirrored configuration (Fig. 4.1B, bottom left) when  $\tau$  is small (Fig. 4.1F, bottom). More realistically, this inversion can only be observed with paper prototypes when  $\theta_1$  is also small because the strains

increase with  $\theta_1$ . To demonstrate a realistic range where the paper prototypes only experience minor damage, i.e., the peak strain is less than 5% (the dark blue region). Regarding the bending simulation, we fix  $\theta_1 = 70^\circ$  and  $\tau = 0^\circ$  for the bottom frustum of a unit, and only vary the two angles for the top frustum. We use a four-point bending test to check the bending stability of the corrugated tube [46], and a multi-stable bending can only occur with small  $\theta_1$  and  $\tau$  as well (Fig. 4.1F). The parameters of the bottom frustum can also have limited influence on the bending stability, but it will not change the trend with respect to the parameters of the top frustum [42, 46].

As  $\theta_1$  and  $\tau$  increase, the axial response will change from inversion to twisting, and a combination of large  $\theta_1$  and  $\tau$  generate bi-stability (Fig. 4.1F, top right). All other cases in-between will undergo a mono-stable twisting deformation, and the adjacent panels will come into contact before the strain energy reaches a local minimum.

A corrugated tube is constructed when the origami frusta shown in Fig. 4.1D are serially interconnected (Fig. 4.1G). Let  $m$  denote the number of frusta, there are up to  $3^m$  different states of the tube since each frustum has three stable states. However, we focus on three representative stable states of the tube as shown in Fig. 4.1G: from left to right: when all frusta stay at the twisted state, the initial state, and the pop-up state. Those states have different bending stiffness that will be discussed in Section 4.4.

## 4.2.4 Stiffness of the bar and hinge model

### 4.2.4.1 Definition of stiffness parameters in the bar and hinge model

In this work, we use a bar and hinge model to simulate the pop-up deformation and the subsequent behaviors. Mechanical stiffness and deformations of the origami structure are represented using a combination of three elements (Fig. 4.2). The in-plane stiffness for stretching and shearing deformations are represented by space bar elements (Fig. 4.2B). The out-of-plane bending stiffness of the sheet is lumped into discrete hinges that are placed along the diagonal of the quadrilateral (Fig. 4.2C). Another type of hinge element, called the folding hinge, is placed along the crease to capture stiffness related to folding the crease (Fig. 4.2D). Each of those elements is assigned a stiffness that has been calibrated to the elastic material properties (Young's modulus  $E$  and Poisson's ratio  $\nu$ ), the sheet thickness  $t$ , as well as the panel geometries [67, 82, 84, 116].

The in-plane stretching stiffness is represented by the space bar stiffness  $K_S = EA/L$ , where  $A$  is the bar cross-sectional area and  $L$  is the bar length. Formulations of bar cross-sectional areas for different polygonal panels have been established in the literature [67, 116]. Our modeling strategy, however, involves subdivision of triangular panels in the conical Kresling, which require new bar area definitions for accuracy. Based on previous work, we modified the bar area definition such that the local (in-plane stretching and shearing) and global (axial compression of a conical Kresling)

behavior matches the result of finite-element simulation (Section 4.2.4.2). For a triangular panel of thickness  $t$  and polygonal area  $S$ , we assign an area  $A_i$  for bar No.  $i$  belonging to this panel (Fig. 4.2B):

$$A_i = \frac{0.36St}{(1-\nu)\sum w_i} \cdot \left(\frac{h_i}{w_i}\right)^{1/3} \quad (4.1)$$

where  $w_i$ ,  $h_i$  is the length and height corresponding to bar  $i$ . For a bar that intersects two triangles, its area is calculated by adding up the above values come from involved triangular panels.

The panel bending stiffness  $K_B$  depends on the material properties as well as the panel geometry. For a bending hinge of length  $L_B$ , the stiffness definition is modified from previous work [67] in an effort to match the finite-element result of axial compression:

$$K_B = 0.23 \cdot \frac{Et^3}{12(1-\nu^2)} \cdot \left(\frac{L_B}{t}\right)^{1/3} \quad (4.2)$$

The folding stiffness can be affected by case-specific factors and a precise description has not been established yet. As shown in Fig. 4.2D, for a crease line of length  $L_F$ , the stiffness is approximated by the following equation based on previous work [67, 68]:

$$K_F = \frac{L_F}{L^*} \cdot \frac{Et^3}{12(1-\nu^2)} \quad (4.3)$$

Complicated and localized effects such as the material anisotropy, fabrication process, and bending history, are simplified and reduced into a single parameter, called the length scale factor  $L^*$ . This factor is typically believed to be proportional to the sheet thickness [68]. Given that in our work the thickness  $t$  is normalized by the radius  $R$  to enable a scalable analysis,  $L^*$  is also normalized as  $L^*/R$  for a fully scalable analysis. In this work, we set  $L^*/R = 3$  unless specifically mentioned. Using a sensitivity analysis in the next section, we show that the value of  $L^*$  does not affect the qualitative results of the pop-up stability and the stiffness tuning.

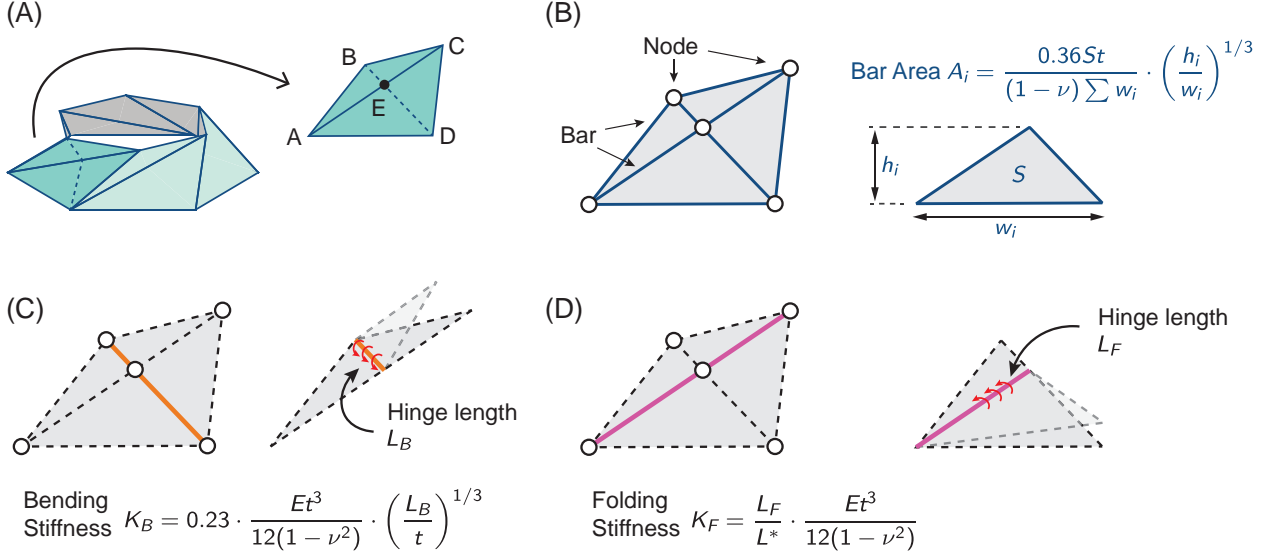


Figure 4.2: Stiffness definition of the bar and hinge model. (A) A frustum is discretized into bars and hinges. (B) The in-plane bars and the area definition. (C) The hinges for capturing the out-of-plane bending of the panels. (D) The hinges for representing the folding of the creases.

#### 4.2.4.2 Finite-element verifications

We perform finite-element simulations (ABAQUS/Standard [66]) on triangular panels and the origami frusta to verify the bar and hinge model. To examine the in-plane performance of the bar and hinge model, different triangular panels are stretched and sheared and compared to a similar simulation with a discretized FE model (Fig. 4.3A, B, D, and E). By varying the aspect ratio and the skew angle  $\beta$  (Fig. 4.3A), the comparison can be made for triangular panels of various shapes. Figure 4.3C and F show the comparison, where the stiffness are normalized by the maximum value within each parametric range. For both of the characteristic deformation modes, the truss stiffness qualitatively match with the FE stiffness, while the error varies with the triangular shape. For less skewed triangles the bar and hinge model tends to underestimate the axial stiffness but overestimate the shear stiffness. For more skewed triangles ( $\sim \beta > 90^\circ$ ), the bar and hinge model is reasonably accurate for both stretching and shear deformations.

While the accuracy of the truss model for in-plane deformations does vary, typically the global response of most origami structures is determined by the geometry-dominated competition of kinematics and stiffness, not the localized material strains [81]. Thus, the global stiffness and the geometric influences could be predicted with reasonable accuracy even if the in-plane stiffness is only crudely approximated. In order to demonstrate this feature, we build a finite-element model of the origami frustum to provide a high-fidelity benchmark for the results (Fig. 4.3G). Panels are meshed with S3 general purpose elements, where adjacent panels are connected via connector

elements with prescribed stiffness to simulate crease rotations (the same stiffness as defined in Eq. (4.3)). Linear-elastic material properties are set to be the same as the bar and hinge model. Convergence with respect to the mesh density is examined, and a mesh size of roughly  $0.03R \times 0.03R$  can provide a stiffness estimation that is within 0.5% of a mesh with  $0.01R \times 0.01R$  elements. Aiming to minimize the discrepancy of the global axial stiffness, the calibration of the model returns the stretching and bending stiffness definitions as shown in Eq. (4.1)(4.2).

With the calibration, a close match of the axial stiffness is achieved for various geometries. In Fig. 4.3H, we show the comparison for three categories of frusta. From left to right are frusta that would undergo twisting collapse, large-strain inversion, and small-strain inversion if the prescribed displacement is big enough. In each category, we vary either the twisting angle  $\tau$  or the slant angle  $\theta_1$  to enable a parametric comparison. The axial stiffness of the bar and hinge models are in good agreement with those of the FE models. Furthermore, we compare the large-displacement response between the bar and hinge model and the FE model. Specifically, the critical force and the associated axial displacement (Fig. 4.3I), are computed using both numerical models. The results are listed in Fig. 4.3J, and a good agreement is also achieved for the representative case from each of the above categories.

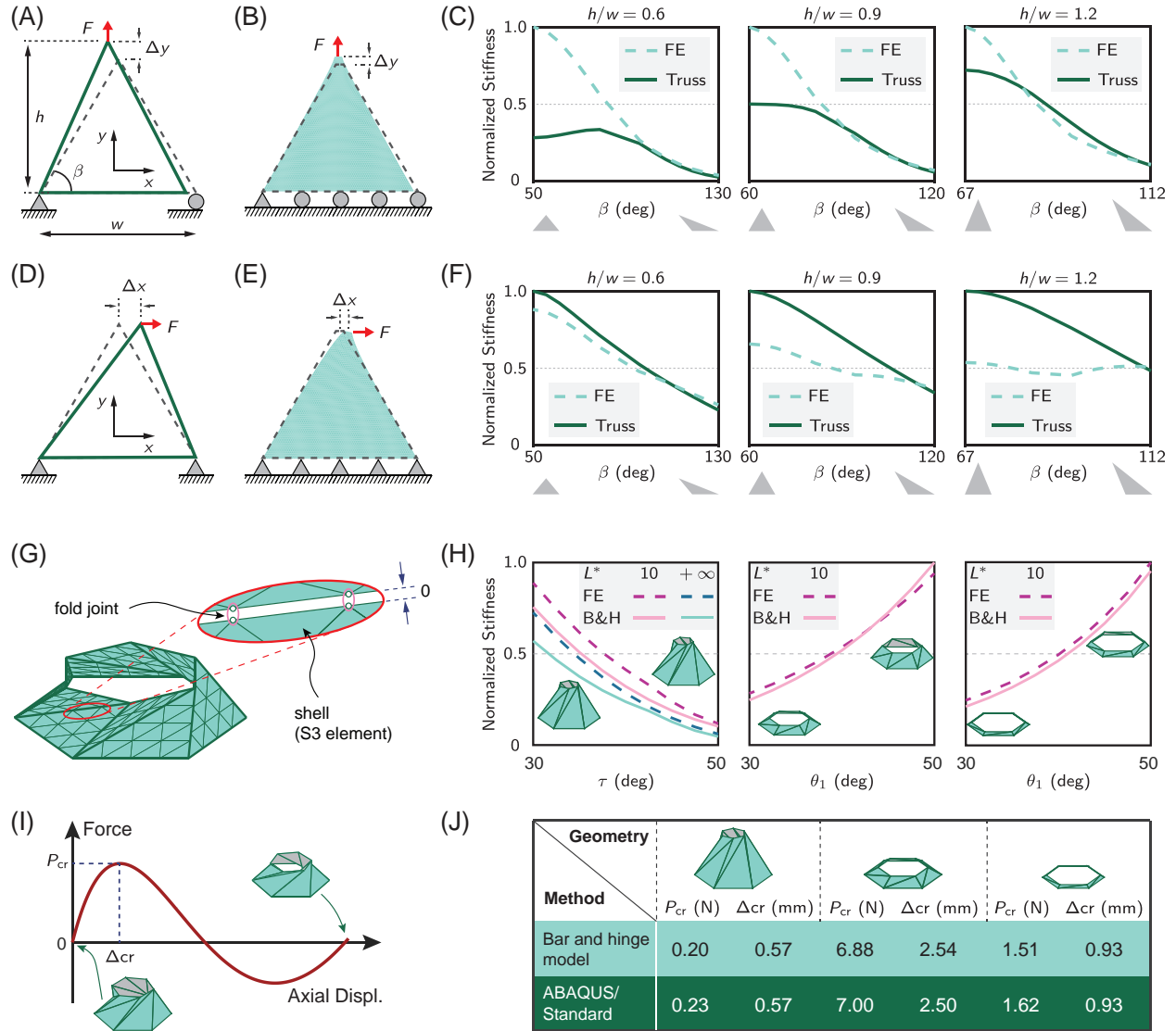


Figure 4.3: Comparison of the numerical predictions between the finite-element (FE) model and the bar and hinge model. In-plane deformations of triangular panels are simulated as stretching and shearing using the bar and hinge model (A, D) and the FE model (B, E), respectively. The normalized stiffness of stretching and shearing are shown in (C) and (F) for triangles of various shapes. (G) Finite-element model of the Kresling frustum shown with a representative sketch of the meshing scheme, while a finer mesh is used for the actual analyses. The zoom-in plot shows the details of the connections between adjacent panels. (H) Predictions of the axial stiffness of the frustum with the bar and hinge model and the FE model. (I) A sample bi-stable axial loading response of the frustum, where the critical force and the corresponding axial displacement are denoted by  $P_{cr}$  and  $\Delta_{cr}$ , respectively. (J) Predictions of  $P_{cr}$  and  $\Delta_{cr}$  with the bar and hinge model and the FE model.

## 4.3 The pop-up deformation

In paper prototypes, we observe that the origami frustum can deform into and stay at a pop-up state (Fig. 4.1D). Using the bar and hinge model described in Section 4.2, we capture this bi-stability of the pop-up and understand the underlying energy behaviors. We then vary the two angles  $\theta_1$  and  $\tau$  to investigate the geometric influences on the stability and the shape change. A mode tuning of deformation, as well as a global bending deformation due to partial pop-up, will be discussed in Section 4.3.2.

### 4.3.1 Pop-up and the resulting shape change

For modeling the pop-up with the bar and hinge model, we need to determine the location of the bending hinges. Due to restriction of bending by adjacent panels, a parallelogram panel in an origami will bend along the short diagonal [117, 118, 119, 120], especially in large deformations. Here, we observe a similar phenomenon for the triangular panels during the pop-up deformation (Fig. 4.4A). For the two adjacent triangular panels that are connected by a valley crease, there are two vertices that are not located on the connecting crease. After the pop-up (from (i) to (ii)), we draw a dashed line that connects those two vertices (Fig. 4.4A, part (ii)). The two triangular panels bend with a single curvature over the dashed line (part (iii)), and such bending can be simplified and represented by the concentrated torsion of a hinge, within the bar and hinge model.

The simulation of the pop-up deformation with the bar and hinge model is shown in Fig. 4.4B for a frustum with  $\theta_1 = 50^\circ$ ,  $\tau = 35^\circ$ . In the planar pattern (Fig. 4.1B), each side of the frustum corresponds to a quadrilateral ABCD (Fig. 4.4B), in which one diagonal corresponds to the valley crease. We define bending hinges along the other diagonal to be able to capture the pop-up (Fig. 4.4B, process (1)). The quadrilateral is thus divided into four triangles that intersect at a node E, and these intersecting nodes will be loaded with outward concentrated forces to trigger the snap-through buckling (Fig. 4.4B, process (2)). Under an appropriate loading magnitude, the frustum will pop into a dome-like shape (Fig. 4.4B, process (3)).

The pop-up state is a stable state, which indicates that the strain energy reaches a local minimum. This underlying energy behavior is captured in the bar and hinge simulation (Fig. 4.4C). There are three sources of strain energy that correspond to different mechanical deformations. The stretching strain energy first increases then decreases, while the bending and folding strain energies show monotonically increasing trends during the pop-up (Fig. 4.4C). Effectively, the total energy has a valley point that corresponds to the pop-up state. This bi-stable energy behavior is similar to the bi-stable bending of corrugated straws [46], where the in-plane strain energy is the only driving factor for bi-stability.

The pop-up deformation occurs without significant panel stretching as shown by the simulation

results in Fig. 4.4D, where the peak bar strains remain less than 1.5% during the pop-up. Because of these low strains, our physical prototypes do not experience visible damage after undergoing multiple cycles of the pop-up, i.e., remaining within the linear regime for construction paper [121]. Given that the deformation mode is axially symmetric, we only show the bar strains of one parallelogram, using the naming conventions of Fig. 4.4B. The bar strains are plotted versus the normalized displacement  $\Delta_E/R$  of the intersecting node. At the pop-up state, the in-plane strain energy is negligible, as compared to the crease folding and sheet bending energies (Fig. 4.4C, E).

From these analyses, we know that a pop-up deformation is bi-stable when the stretching energy dominates the process. Based on classical plate theory, the stretching energy is a linear function of the shell thickness  $t$ , while the bending energy is proportional to  $t^3$ . In the bar and hinge model, the folding energy and sheet bending energy are also both modeled as cubic functions of  $t$  (see 4.2.4.1). Therefore, for the same geometry, the pop-up of frustum can be bi-stable with thinner sheets and mono-stable with thicker sheets. This relationship is confirmed by the parametric study shown in Fig. 4.4F. Using a normalized thickness  $t/R = 4 \times 10^{-3}$ , the pop-up process is bi-stable for most geometries (the light pink and dark pink region). When the sheet thickness is roughly quadrupled, the bi-stable region shrinks to the top right corner (the dark pink region). Fig. 4.4F (part i) shows the energy behavior and bar strains for the frustum as in Fig. 4.4B, C, D, but with higher thickness. During this mono-stable deformation, the bar strains show similar profiles as those of the thinner counterpart. However, the folding and bending energies occupy a greater portion, and there is no valley point in the total energy. A pop-up process can still be mono-stable with thin sheets ( $t/R = 4 \times 10^{-3}$ ), and part ii of Fig. 4.4F shows an example where the frustum geometry is  $\theta_1 = 25^\circ$ ,  $\tau = 20^\circ$ . With the new geometry, the initial state is less twisted. The change in bar strains is similar, whereas the strain magnitude is significantly decreased from  $\sim 1.4\%$  to  $\sim 0.3\%$ . The stretching energy becomes less important and cannot counteract the increasing trends of the bending and folding energy. Therefore, the pop-up process is mono-stable.

The pop-up deformation converts a twisted Kresling frustum to a dome-like shape that has a different slant angle  $\theta_1$ , twisting angle  $\tau$ , and enclosed volume (Fig. 4.1D). These geometric changes are quantified using the simulation results (Fig. 4.4G). The frustum becomes a convex shape as the valley creases pop out, thus the enclosed volume is always increased. For most cases, the volume is elevated only slightly, while an extremely shallow and twisted frusta will see an sharp increase in enclosed volume by around seven times (Fig. 4.4G, the top-left corner of the first contour plot). After the pop-up, the frustum will become less twisted, as compared to the initial state. In other words, the relative twisting angle between the two polygons become smaller. As the initial  $\tau$  increases, the difference becomes more significant (Fig. 4.4G, the second contour plot). On the other hand, the slant angle, will become larger after the pop-up, i.e., the frustum becomes steeper (Fig. 4.4G, the third contour plot). Thus, a shallower and more twisted frustum gains a

larger increase of the slant angle. As a summary, frusta with smaller  $\theta_1$  and  $\tau$  angles can result in more tunable systems that experience larger geometric shape change from the pop-up deformation.

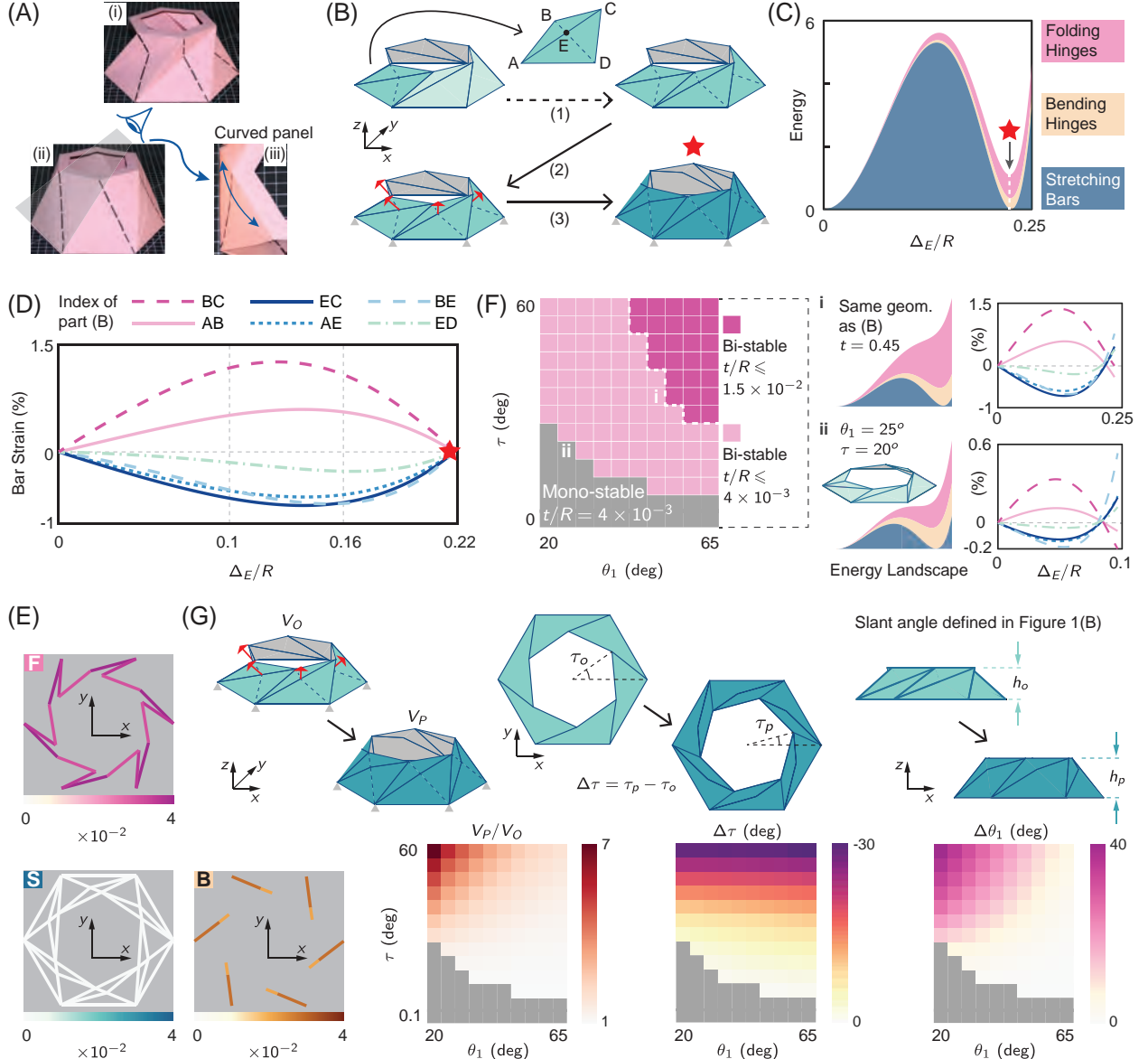


Figure 4.4: Pop-through of valley creases converts the cone to a dome-like shape. (A) A paper cone in its initial state (i) and pop-up state (ii). The zoom-in photo (iii) shows the panel curvature after pop-up. (B) By placing a node on the valley crease, the pop-up process can be simulated by the bar and hinge model. (C) The energy landscape of a bi-stable pop-up process. (D) The bar strains experienced during the pop-up process. (E) The energy distribution at the pop-up state. The folding, stretching, and bending energy plots are counterclockwise arranged. (F) Left: Numerical predictions of the pop-up stability with respect to the geometric parameters and the sheet thickness; Right: underlying energy behaviors of two mono-stable cases. (G) Shape change from the initial state to the pop-up state, including the enclosed volume (Left), the twisting angle (Middle), and the slant angle (Right).

### 4.3.2 Tunable deformation

We observe two phenomena that connect the pop-up with the multi-stable inversion and bending behaviors in Section 4.2. As we showed in Fig. 4.1E, under an axial load, shallow and less twisted frusta can be inverted to a flipped configuration, while those that are steep and more twisted frustum experience a bi-stable twisting deformation. Those frusta in-between will undergo a mono-stable twisting deformation, and the adjacent panels will come into contact to prevent further axial displacement. Here, we set  $\theta_1 = 35^\circ$ ,  $\tau = 35^\circ$ , and while such a geometry does not have the classified twisting and inversion bi-stabilities, it can experience a bi-stable pop-up deformation. The mono-stable twisting deformation and the bi-stable pop-up deformation can be captured by both the bar and hinge model (Fig. 4.5A) and the paper prototype (Fig. 4.5B). After pop-up, when an axial load is applied to the top edge, the frustum can now also be inverted to a flipped configuration (Fig. 4.5A, B, bottom row). Therefore, with certain geometries, a frustum can have two deformation modes under axial load: a mono-stable twisting or a bi-stable inversion after pop-up.

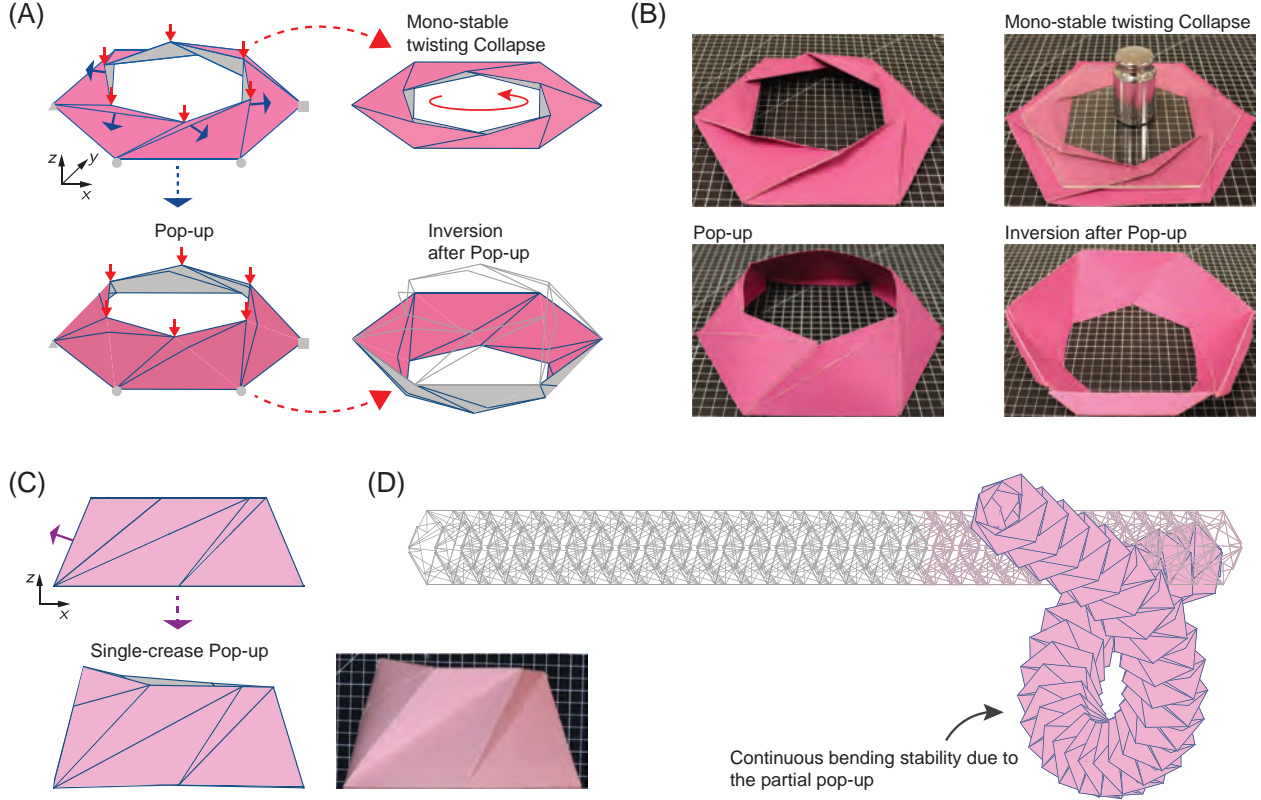


Figure 4.5: Pop-through of valley creases enables the switching of deformation modes. (A) Under vertical loading, many Kresling frusta geometries are mono-stable and collapse via a twisting motion from their initial states. However, they can also be axially inverted after experiencing a pop-up deformation. (B) The axial mode switch demonstrated with a paper prototype. (C) By pop-through of only one crease, the Kresling frustum reaches a tilted state, which allows for continuously-changing orientations and bending-like multi-stability over the tube length, as shown in (D).

Besides the axial deformation, the bending stability can also be tuned by the pop-up. When we apply forces to all valley creases, a frustum is popped into a dome-like shape, where the top edge is still parallel to the bottom edge (Fig. 4.1D). However, the top edge becomes tilted with respect to the bottom edge when only one valley crease is popped (Fig. 4.5C). A relative rotation is thus created within a frustum, and a corrugated tube consisting of multiple tilted frusta will result in a globally rotated configuration. Here, we set  $\theta_1 = 65^\circ$ ,  $\tau = 50^\circ$  so this corrugated tube typically remains mono-stable for bending and cannot snap into different bent states like a bendy straw (Fig. 4.1C, E). However, we simulate a corrugated tube consisting of sixty interconnected frusta, where each frustum is tilted by popping only one valley crease (Fig. 4.5D). This tube, which otherwise has no stable state under a bending moment, now turns into and stays at a knot-like shape.

## 4.4 Tunable stiffness

The pop-up deformation not only provides the change of shape and stability, but it also allows for the stiffness tuning in the axial and bending directions. We observe the tunable stiffness with the paper prototypes, then quantify the stiffness tuning using the bar and hinge model. The following subsections describe the multi-step analysis used to explore stiffness tuning, as well as the underlying mechanics and geometric influence on these tunable behaviors.

### 4.4.1 Tunable axial stiffness

The conical Kresling allows for tunable stiffness where the pop-up state is significantly stiffer than the initial state. A frustum with a large twisting angle  $\tau$  is flexible in its initial state that allows motion and deployment, but is stiff after reaching the pop-up state. Figure 4.6A shows that, under the axial load from a plastic panel that weighs  $\sim 20$  g, a frustum ( $\sim 2.8$  g) collapses to a nearly-flat configuration via a twisting motion (from (i) to (ii)). However, after the pop-up (from (i) to (iii)), it supports a mass of more than 1.5 kg without any visible deformation (iv).

This tunable axial stiffness can be captured using the bar and hinge model, and Fig. 4.6B illustrates the multi-step analysis for computing the axial stiffness. During pop-up step (step (1)), all the bottom nodes are fully restrained, and the valley creases are popped out by forces applied at the intersecting nodes (defined in Section 4.3.1). Next, the bottom nodes are released to slide (step (2)), and the pop-up frustum will settle into a slightly different configuration. Finally, using displacement control, the pop-up frustum is axially loaded to compute the stiffness (step (3)). Let  $\Delta$  denote the axial displacement, then both the initial and pop-up states are compressed by  $\Delta = 1.3 \times 10^{-3}R$ . This displacement is small compared to the frustum dimensions so nonlinear behaviors can be neglected.

After the pop-up, the axial stiffness is increased by more than four orders of magnitude ( $K_P/K_O \approx 1.2 \times 10^4$ ) for the geometry of  $\theta_1 = 50^\circ, \tau = 60^\circ$ , as shown in Fig. 4.6C. The rationale behind this drastic increase can be understood from the perspective of the fundamental mechanisms of the Kresling origami. The change of the energy distribution is plotted in Fig. 4.6D and E for the axial compression of the initial state and the pop-up state, respectively. For the initial state, the change of bending energy and in-plane energy in the panels are negligible, as compared to the crease folding energy (Fig. 4.6D). During axial compression in this initial state, the stiffness may vary due to the materials and fabrication process [68, 122, 123, 124], but will remain flexible because no crease folding occurs. When popping the frustum into the pop-up state, the crease network is rearranged to be topologically different. As a consequence, the axial deformation mode requires stretching and shearing of the thin panels and thus a significantly higher amount of *energy change* (Fig. 4.6E). Here, the crease folding and the panel bending energies are barely changed

during the axial compression, while the in-plane energy of the panels increases substantially. Thus, the pop-up state is substantially stiffer than the initial state. Using a sensitivity analysis in Section 4.4.3.1, we show that the value of the folding stiffness does not affect this conclusion.

The stiffness tunability strongly depends on the geometry of conical Kresling, specifically, the slant angle  $\theta_1$  and twisting angle  $\tau$ . The ratio of the pop-up stiffness to the initial stiffness is computed for those geometries that show bi-stable pop-up deformation (Fig. 4.6F). The parametric results indicate that, increasing the initial twisting angle  $\tau$ , or decreasing the slant angle  $\theta_1$ , can lead to a higher stiffness ratio. In other words, a shallower and more twisted frustum offers more prominent stiffness tuning. This finding is correlated to the shape change in the pop-up (Fig. 4.4G), i.e., the stiffness sees a higher increase as the shape changes more.

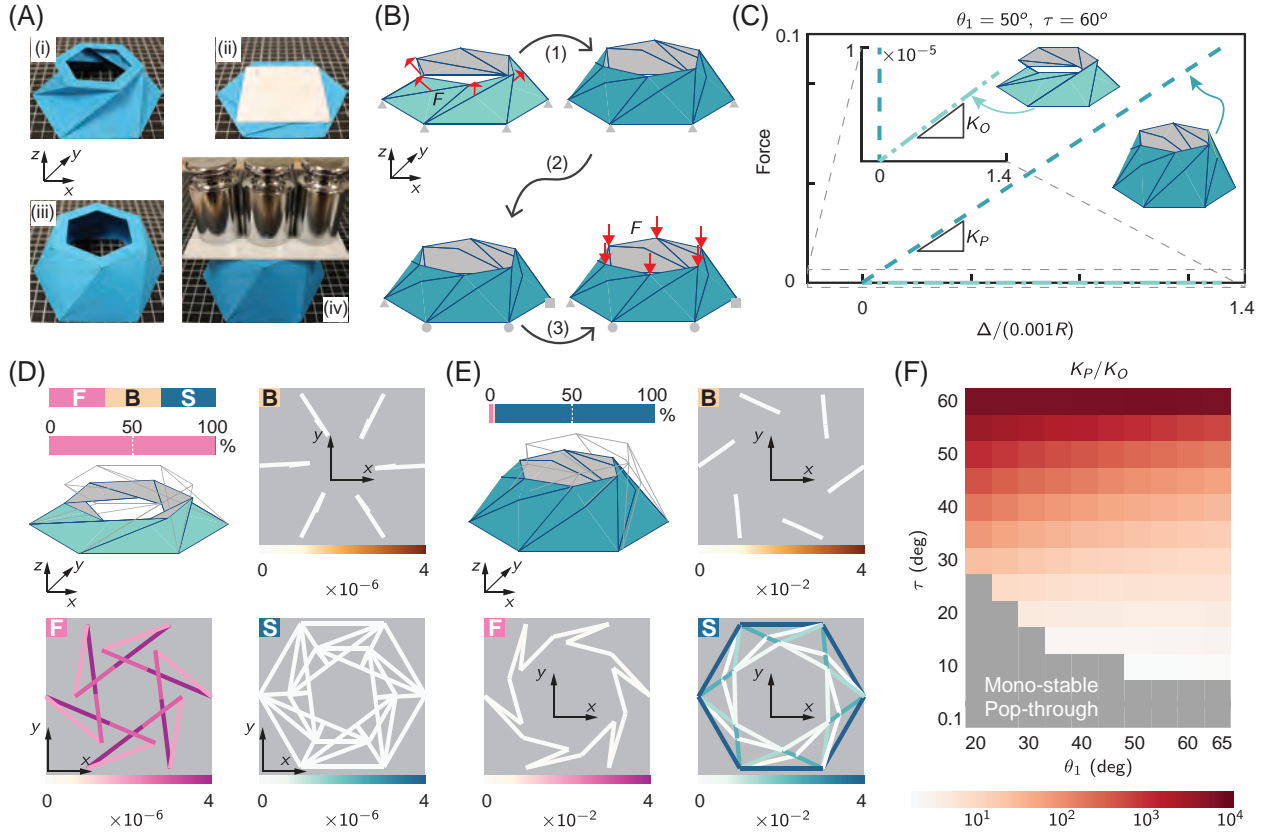


Figure 4.6: The conical Kresling has a tunable axial stiffness. (A) The paper frustum can be collapsed by a thin plastic panel when it is in the initial state, but can support three calibration weights of 1.5 kg when in a pop-up state. (B) The simulation setup using the bar and hinge model. (C) Numerical predictions of the axial force-displacement ( $\Delta$ ) curves of the initial frustum and the pop-up frustum show that the structure stiffer by more than ten thousand times. (D) The change of energy in different bending, folding, and stretching elements during the vertical loading for the initial frustum and (E) the pop-up frustum. (F) The ratio of the pop-up stiffness to the initial stiffness for different geometric parameters.

#### 4.4.1.1 Experimental proof-of-concept verification

**Sample fabrication** In this work, we fabricated physical models with different construction papers, and the normalized thickness is fixed at  $t/R = 4 \times 10^{-3}$ . For the axial compression tests, the specimens are fabricated from paper sheets with a thickness of 0.25 mm, and the outer radius  $R$  is set to be 62 mm. For illustrating the multi-stable behaviors, however, we fabricate larger paper prototypes ( $R = 93$  mm) using thicker paper sheets (0.37 mm). For each frustum, the planar crease pattern is input into a CAD software and then cut into a paper sheet using a laser cutter (Universal Laser VLS6.60). The patterned sheet is then manually folded into the frustum shape. Each planar cut of the frustum has extra tabs for connecting them to neighboring units. For a stand-alone frustum, strips are attached to a hexagonal top and bottom edge that offers a similar confinement as that provided by an adjacent frustum.

We recognize that these physical models are made of paper and as such embody complexity that is not captured in our models, e.g., anisotropy [125]. However, the physical specimens are used primarily as a proof-of-concept verification to show that the types of multi-stable behavior observed in the simulations also occur in physical models with the same geometric parameters.

**Axial compression test** The stiffness tuning is experimentally quantified using axial compression tests, and the frusta are loaded using a Mark-10 testing stand (ESM1500G) and a force gauge (M5-50). As shown in Fig. 4.6, the global compression strain (compression/frustum height) is controlled below 1% to avoid nonlinear effects. Each specimen is compressed at a strain rate of 1 mm/min. We observe that the axial compression response stabilizes after 20 load-unload cycles, thus every specimen is compressed 20 times prior to data collection.

Here, we fabricate origami frusta of four geometries ( $\theta_1 \in \{50^\circ, 65^\circ\}$ ,  $\tau \in \{35^\circ, 50^\circ\}$ ), and compress each specimen from the initial state and the pop-up state (Fig. 4.7A). We run seven tests for each of the specimens, and Fig. 4.7B shows the average and the range of the loading responses. The compression distance is set to be small as compared to the frustum dimension, thus the loading responses are approximately linear. Based on linear regression of the experimental data, we compute the initial and pop-up stiffness, as well as the stiffness ratio (Fig. 4.6C). The experimentally-derived stiffness ratios are in good agreement with those of the bar and hinge model, and the largest relative error among the four geometries is 8.8%.

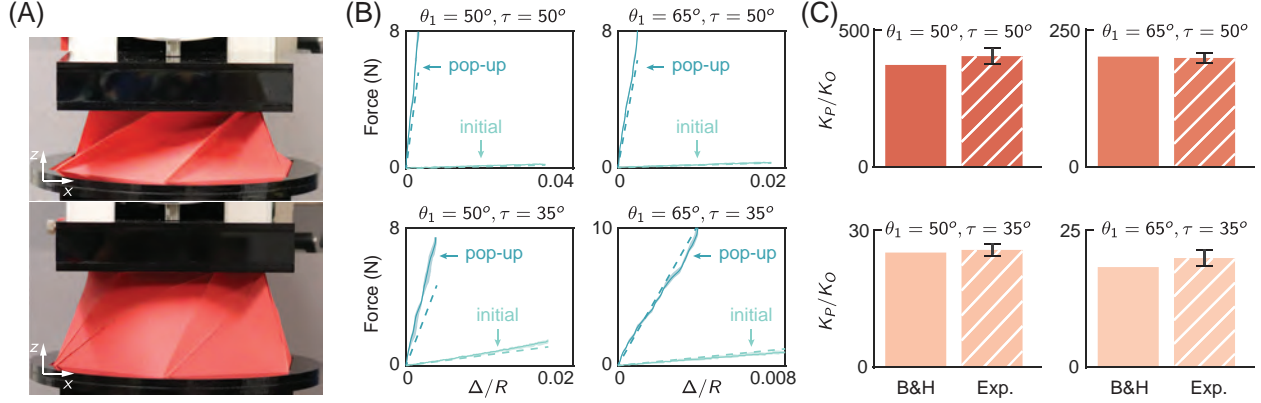


Figure 4.7: The tunable axial stiffness is verified by experimental tests. (A) A paper frustum being quasi-statically compressed in its initial state (top) and pop-up state (bottom). (B) The axial loading responses of paper frusta with four geometries. The solid lines are the averaged responses, and the shaded region denote the range of experimental data. The dashed lines denote the bar and hinge predictions when the Young’s modulus equals to 3.5 GPa. (C) Comparison of the stiffness ratio between the bar and hinge model and the experimental results. The bars show one standard error for seven tests.

#### 4.4.2 Tunable bending stiffness

A corrugated tube made of conical Kresling frusta will be multi-stable, where the number of stable states grow exponentially with the number of frusta. As shown in Fig. 4.1G, we focus on three representative state: where all frusta are configured to the twisted, initial, or pop-up states. In this section, we use eigenvalue analyses to compare the global bending stiffness, and cantilever tests to explore the bending isotropy.

To compare the tube bending stiffness at the three representative state, we perform an eigen analysis, where each eigenmode represents a unique deformation mode of the structure, and the associated eigenvalue is proportional to the total energy (kinetic and strain energy). A higher eigenvalue indicates a higher excitation energy and thus a higher stiffness for the corresponding mode. No boundary constraints are applied on the structure so the first six eigenmodes represent rigid body motions. We omit these modes and start the numbering at the seventh mode, i.e.,  $\lambda_3$  would be  $\lambda_9$  if those rigid-body modes are counted.

We set the tube geometry as  $\theta_1 = 65^\circ$ , and  $\tau = 50^\circ$ , and the global bending eigenmodes for each state are shown in Fig. 4.8A. We select the first global bending mode, which effectively represents the most flexible way to bend the tube. By varying the initial twisting angle  $\tau$ , the eigenvalue corresponding to global bending is plotted for all three states (Fig. 4.8B). All eigenvalues are normalized by the maximum within the range of  $\tau \in [35^\circ, 55^\circ]$ . Frusta on the ends are reinforced

to the limit the localized eigenmodes, and as shown in Section 4.4.3.2, these end reinforcements do not affect the global bending characteristics. Figure 4.8B shows that the eigenvalue for global bending is highest for the pop-up state, it is intermediate for the initial state, and is lowest for the twisted state.

The bending eigenvalues of both the initial state and the pop-up state decrease when the twisting angle  $\tau$  increases. On the other hand, the bending eigenvalues for the twisted state shows an increasing trend versus  $\tau$ . These opposing trends allow for designs where the bending stiffness can be highly tuned. For example, a tube with  $\tau = 40^\circ$  will have normalized eigenvalues of 0.97, 0.30, 0.01 for the pop-up, initial, and twisted states respectively, while a tube with  $\tau = 55^\circ$  will have normalized eigenvalues of 0.86, 0.19, 0.14 for the same three states.

We next use a cantilever test to explore the bending isotropy of the corrugated Kresling tube. The corrugated tube can find a suitable application as a reconfigurable cantilever with tunable stiffness. At the supported end, all nodes are fully fixed, whereas a total force of 1 is distributed on the other end of the tube (Fig. 4.8C). The cantilever stiffness is calculated as  $K = 1/\delta$ , where  $\delta$  is the maximum tip displacement. Based on the cantilever stiffness, we compute an equivalent section modulus (the second moment of area,  $I$ ) for different directions orthogonal to the Z axis (Fig. 4.8D). Here, we use a fixed radius  $R$  of 31 mm. Using the section modulus for the bending comparison eliminates the effects of the tube length, thus giving a fair comparison among all three states. A convergence study shows that a tube with twelve frusta provides the equivalent section modulus that is within 0.1% of a tube with twenty frusta (see Section 4.4.3.3). By deploying and popping a tube from the twisted state, the section modulus can be increased by around fifty times.

Interestingly and beneficially, the section modulus is highly isotropic (Fig. 4.8D). Although the frusta are hexagonal, there are relative twists between the adjacent frusta that makes the cross-sections of the tube look like a circular shape, as depicted by the Y-Z plane view (Fig. 4.8C). As a consequence, the tube is nearly-isotropic when used as a cantilever, meaning the loading response is consistent for all directions.

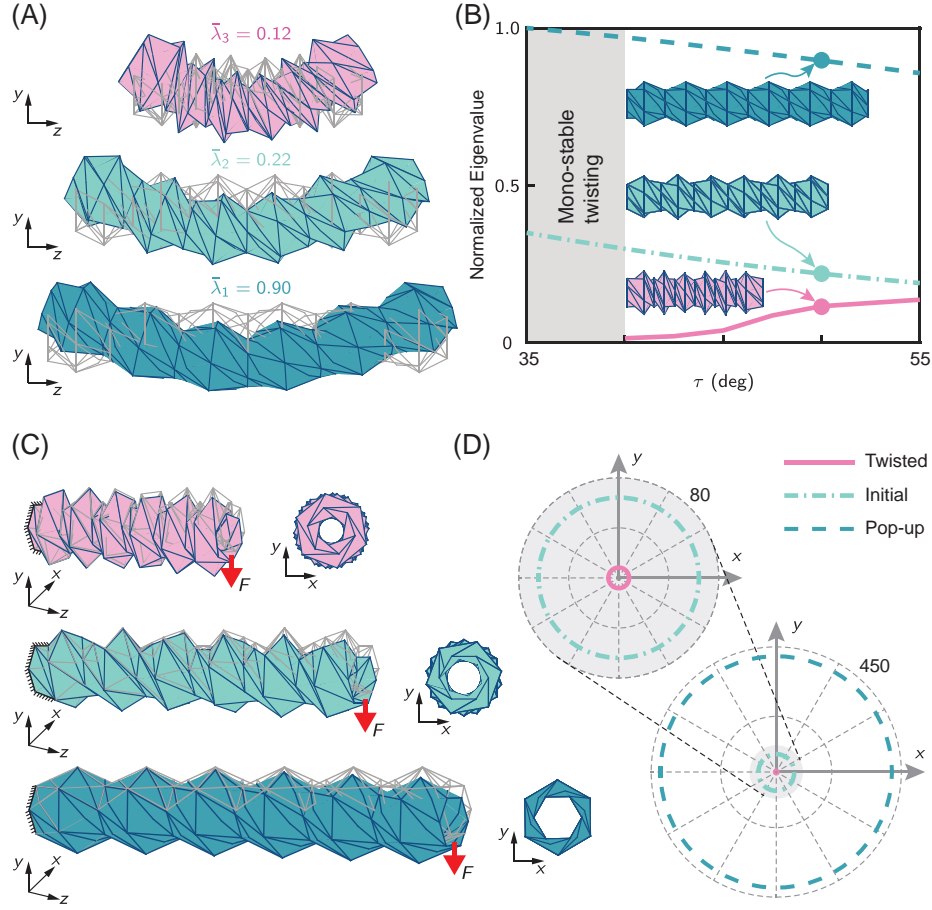


Figure 4.8: Multi-stability of twisting and pop-up leads to tunable bending stiffness of the Kresling corrugated tube. (A) Deformation eigenmodes that correspond to the global bending of the twelve-frustum tube at its twisted state (top), initial state (middle), and pop-up state (bottom). (B) The normalized bending eigenvalue ( $\bar{\lambda}$ ) vs. the initial twisting angle for the three stable states. (C) Deformation of the corrugated tube when used as cantilevers at different stable configurations. The left end is fixed, and a uniform load is applied on the right end. The deformed shapes are scaled so the maximum displacement for each case is equal to the difference of the inner and the outer radius. (D) The equivalent section modulus ( $\text{mm}^4$ ) based on the cantilever test for loads in the X-Y plane represented as a polar plot at the three stable states, respectively. Here, the outer radius  $R$  is set to be 31 mm, and the section modulus is shown as distance from origin.

#### 4.4.3 Sensitivity of the analyses

##### 4.4.3.1 Sensitivity of the stiffness tuning

In Section 4.4.1 of the main text, we show the axial stiffness of the frustum can be increased after the pop-up, with the magnitude increase primarily affected by the twisting angle  $\tau$ . A more twisted frustum will provide more significant stiffness tuning. Those results are collected with a

user-defined crease stiffness  $L^*/R = 3$ , where in reality the actual  $L^*$  can vary depending on the type of origami structures. To investigate the effects of the case-specific  $L^*$  on the stiffness tuning, we perform a parametric study for three levels of crease stiffness (Fig. 4.9). With stiffer creases, the bi-stable region shrinks, and the axial stiffness becomes less tunable (i.e., the stiffness ratios are smaller). This behavior is expected because folding energy has a negative impact on achieving bi-stable pop-up (Fig. 4.4C). Moreover, the axial stiffness of the initial state is mainly affected by the crease folding, whereas the stiffness of the pop-up state is dominated by panels stretching and shearing. Therefore, stiffer creases only stiffen the initial state while have little effect on the pop-up state. The overall stiffness ratios thus become smaller. On the other hand, with softer creases, the bi-stable region expands and the stiffness ratios are greater. However, the value of crease stiffness does not change the trend of stiffness tuning of the overall findings reported earlier. A more twisted frustum still causes a more significant stiffness change, no matter what the crease stiffness is.

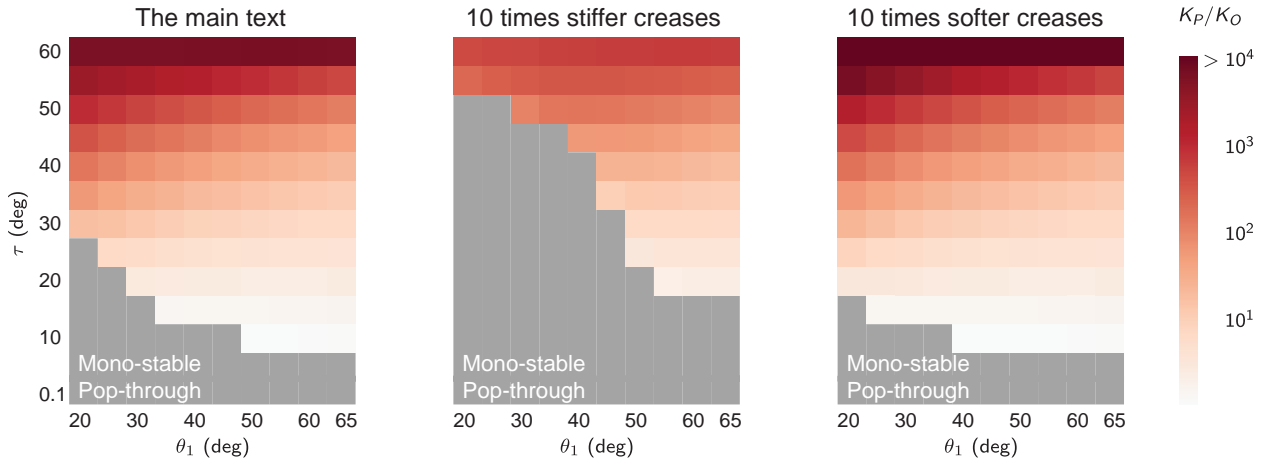


Figure 4.9: Sensitivity of the axial stiffness tuning with respect to the crease stiffness.

#### 4.4.3.2 Reinforcement of the tube ends

In Section 4.4.2, we study the global bending stiffness of tubes made of the Kresling frusta. In our study, we reinforce the end frusta of the tube to avoid eigenmodes that only involve local deformations. Specifically, we reinforce and stiffen the creases within the end frustum by  $10^4$  times to restrict the local deformations. This subsection verifies that this reinforcement does not substantially alter the global bending stiffness. Figure 4.10 shows the global bending eigenmodes and the normalized eigenvalues for both reinforced and unreinforced tubes at the three stable states. The eigenvalues are normalized by the maximum value within the range of  $\tau \in [35^\circ, 55^\circ]$  (see Fig. 4.8). Due to the reinforcement, the end frusta will not be popped or compressed when simulating the global bending of the pop-up tube and the twisted tube, respectively. With the reinforcement,

the global bending is always mode # 3 for the twisted tube, # 2 for the initial tube, and # 1 for the pop-up tube (Fig. 4.10A). The modes before the global bending correspond to flexible axial deformations.

In Fig. 4.10B, we present the global bending eigenmodes for the corresponding tubes without the reinforcement. Notice that, now the global bending modes are 3, 5, 4 for the three states. Without the ends reinforcement, there exist some low-energy eigenmodes that only involve local deformations at the ends. In fact, the mode number of the global bending can vary for different geometries because of these local deformations. One must visually identify the bending eigenmode case by case, and manually collect the associated eigenvalue for the parametric analysis. The reinforcement at the ends allow us to automate this process, without bringing substantial differences into the eigenvalues. The relative error for the initial tube is lower than 0.5%, while the other states observe errors between 5% and 8%. For the reinforced tube, the twisted state is longer than the unreinforced counterpart because the end frusta are not compressed. As a consequence, the bending eigenvalue is smaller. On the other hand, for the pop-up state, the reinforced tube is shorter, and the bending eigenvalue is slightly greater than that of the unreinforced pop-up tube.

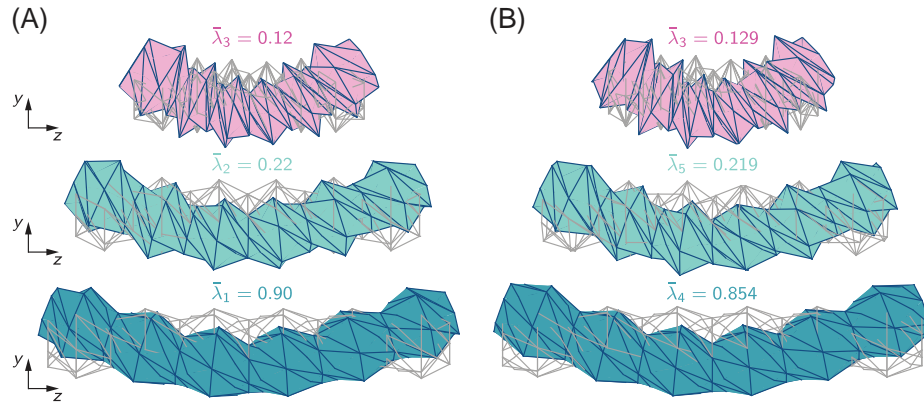


Figure 4.10: Reinforcing the ends of the tube prevents localized deformation modes but does not lead to a significant change in the bending eigenvalues. The deformation modes of global bending, as well as the normalized eigenvalues, are shown for tubes with (A) reinforced ends and (B) unreinforced ends. For the reinforced cases, the end frusta will not be popped or axially compressed. All eigenvalues are normalized by the maximum eigenvalue of the reinforced tube within the range of  $\tau \in [35^\circ, 55^\circ]$ .

#### 4.4.3.3 Convergence of the equivalent section modulus with respect to the number of frusta used

In Section 4.4.2, the corrugated tubes are loaded as cantilevers at the three stable states. We calculate the equivalent section modulus based on this cantilever loading scenario, using a tube

consisting of twelve identical frusta. Here, we show that, in the cantilever test, the twelve-frustum tube provides estimates of the section modulus that are within 1% of a twenty-frustum tube (Fig. 4.11). This claim holds for all three stable states.

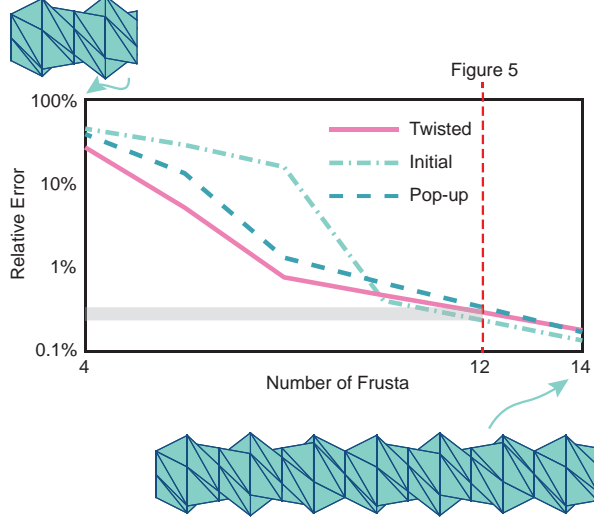


Figure 4.11: The estimated equivalent section modulus converges with the number of frusta. A tube with twenty frusta is used as a point of comparison to find the relative error. For the cantilever tests that are presented in Fig. 4.8, the relative errors are below 1%.

## 4.5 Discussion

### 4.5.1 Findings

Using the reduced-order model and paper prototypes, we explored and demonstrated the robust shape-morphing and stiffness tuning. In particular, the paper has demonstrated the following characteristics of the system.

**Geometrically governed multi-stability.** Each unit frustum of the Kresling tube can have a different multi-stable behavior that is governed by the pattern geometry, namely the twisting angle  $\tau$  and the slant angle  $\theta_1$ . Kresling tubes with a high twisting angle and a high slant angle possesses a twisting type bi-stability, while tubes with low twisting and slant angles can experience an inversion type bi-stability. A subset of Kresling geometries that collapse via a twisting motions can also bend into a partially inverted state similar to the bending of a flexible drinking straw.

**Pop-up bi-stability.** The pop-up bi-stability occurs when the valley folds on the side of the Kresling frustum are pushed out, and the two panels become bent across a diagonal roughly perpendicular to the valley fold. An exploration on the geometric properties reveals that a more twisted

frustum and one that is made of thinner sheets is likely to be bi-stable for the pop-up deformation. When a Kresling frustum has pop-up deformations around the full perimeter, it can be axially inverted to a mirrored stable state. When only a single side of the frustum is popped out, the system undergoes a global bending-type deformation similar to a bent straw. As such, the pop-up bi-stability further enhances the range of deformed multi-stable configurations.

**Pop-up for stiffness tuning.** The pop-up bi-stability allows for tuning of both the axial and bending stiffness of the tube. As the pop-up distorts the frustum, the crease network is rearranged, and the flexible twisting motion becomes prohibited. The axial compression of a pop-up frustum thus primarily engages panel stretching rather than the crease folding, leading to a stiffness increase by up-to-four orders of magnitude. By varying the frustum geometry, we find that a shallower and more twisted frustum provides a more significant change in stiffness due to the pop-up. For certain geometries, the bending stiffness can be further tuned as the frustum can enter a twisted stable state that is more flexible than the initial state.

The advanced tunability allows the system to serve as an adaptable component in more complicated scenarios. Next, we propose three conceptual applications of the system, corresponding to its tunable axial stiffness, shape-morphing, and the tunable bending stiffness.

#### 4.5.2 Conceptual applications

**Tunable energy absorber.** When popped into the dome-like shape, the origami frustum gains a substantial higher resistance to axial compression. As compared to the initial state, the pop-up frustum is expected to generate significantly higher reaction forces during the quasi-static crushing and dissipates much more energy. A tunable energy absorber can be created, without using additional mechanisms to lock the system into a stiff and functional state [45]. We employ a finite-element model (ABAQUS/Explicit [66]) to simulate the crushing response, using the elastoplastic properties of a mild steel [36] and a twisting geometry ( $\theta_1 = 55^\circ$ ,  $\tau = 60^\circ$ ). We also set the outer radius  $R = 31$  mm.

Under an axial compression, the initial frustum crushes to a nearly-flat configuration via a twisting motion that is guided by the crease pattern (Fig. 4.12A). The panels are barely stretched, sheared, or bent, and the majority of the axial resistance comes from the flexible folding at the creases. The reaction force curve increase linearly with the crushing distance and remains relatively low. The pop-up frustum, however, crushes similar to a conventional prismatic crash-box type energy absorber [36] and generates substantial higher reaction forces. When the pop-up frustum is compressed, the crushing results in more panel deformations and material yielding (the inserts of Fig. 4.12A). The pop-up crushes with a substantially higher force plateau and absorbs significantly more impact energy (for this tube design, a roughly tenfold increase).

**Deployable traffic cone.** Given the conical shape and large geometric reconfigurability, the Kresling frustum can be used to construct practical structures such as a traffic cone that allows for compact storage. As shown in Fig. 4.12B, three frusta with shrinking radii are axially stacked to mimic a cone. The frustum geometry is set to be  $\theta_1 = 65^\circ$ ,  $\tau = 40^\circ$  such that the twisted state is nearly-flat when collapsed. By pulling up, the cone deploys and all frusta switch back to their initial state. In this state, the structure remains flexible and can be readily collapsed back. As an alternative, the valley creases can be pushed into the pop-up state which increases the axial load-bearing capacity and ensures that the structure will not collapse back to a stowed state. The traffic cone is reusable since the deployment and the pop-up will not engage plastic deformations.

**Reconfigurable robotic arm.** Another potential application of the system is to create robotic arms with localized tuning of bending stiffness. Soft robotic arms can maneuver effectively in complicated environments because they can undergo large bending deformations without failure [126]. However, continuum system made of soft material have infinite degrees of freedom (DOFs), causing overly flexible systems and increased complexity of achieving accurate motion control [52]. On the other hand, traditional robotic arms made of rigid links and flexible joints allow for precise movement but poor conformability. Utilizing the pop-up deformation which tunes the bending stiffness, one can build a reconfigurable robotic arm that switches between a compliant mode and a joint-link mode [52]. Here we illustrate the idea using a tube of twenty four frusta (Fig. 4.12C). When every frustum is configured to be in a twisted state, the tube is flexible allowing for compliant deformations that can conform to a circular shape. The structure can then be transformed into a joint-link mechanism where some frusta stay in the twisted state to serve as a flexible joint, while others are popped up to form rigid links. This concept for a reconfigurable robotic arm can allow for versatile maneuverability and transformation into a more controllable joint-link system.

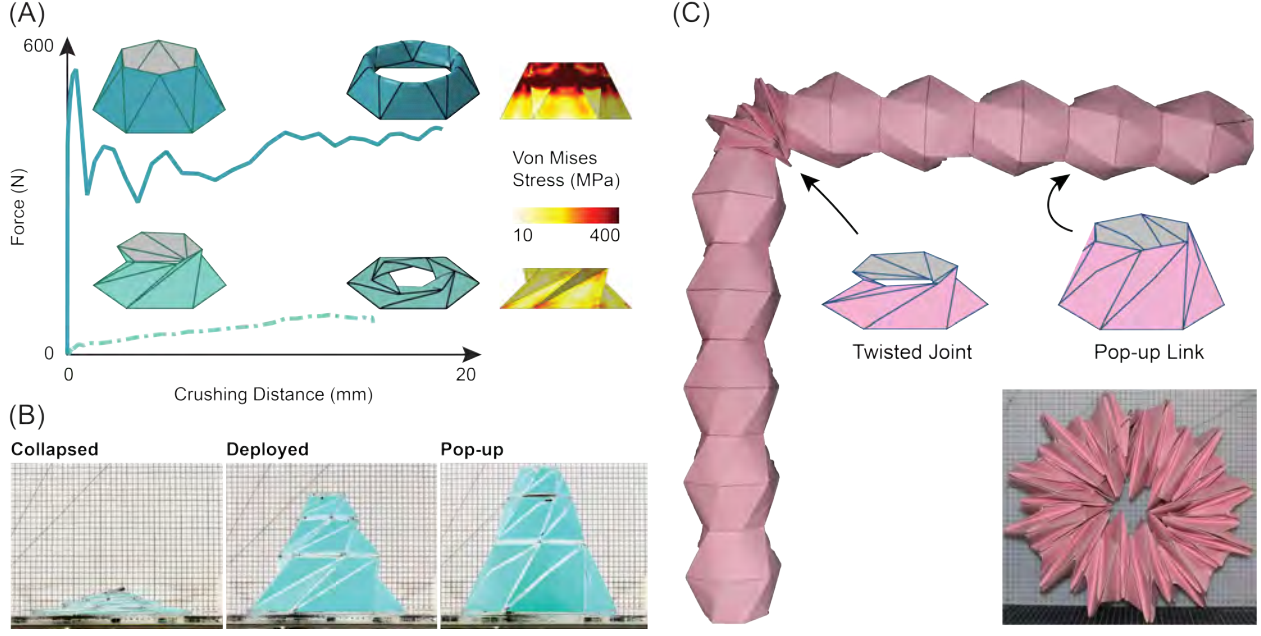


Figure 4.12: Conceptual applications of Kresling corrugated tubes. (A) Tunable and deployable energy absorption system. The axial loading response is shown for the initial and pop-up frustum states, with the corresponding Von Mises stresses at the final crushed states. (B) Kresling frusta with decreasing radii are axially stacked to construct a deployable traffic cone that allows compact storage. (C) The different frusta of a reconfigurable robotic arm, can deform between the compliant mode and the stiff joint-link mode.

## 4.6 Concluding remarks

In this chapter, we explored corrugated tubes made of conical Kresling origami. These offer a wide range of multi-stable deformations and tunable stiffness characteristics. By applying concentrated forces to buckle the valley creases outward, an initially twisted unit can be “popped into” a unique dome-like state. We use an elasticity-based model to investigate the pop-up behavior, its shape-morphing characteristics, and the stiffness tuning that it offers. Proof-of-concept prototypes were fabricated from construction paper and are used to demonstrate the predicted bi-stability, as well as the subsequent stiffness change. Finally, we propose and discuss three potential applications, corresponding to the axial tunable response, the shape-morphing, and the tunable bending stiffness.

This work focuses on the identification of stability, understanding of the underlying mechanics, and quantification of the associated stiffness tuning. Future work on the system could explore the practical realization and usage of the tunability. For example, the tube could be appropriately sealed and pneumatically actuated to achieve state transitions. Moreover, studies could explore

modifications to the design where panels on one side of the polygonal frustum are made of thinner sheets such that they pop out at a lower pressure threshold. As shown in Fig. 4.5, the single-side pop out enables multi-stable rotation of the tube. By strategically placing the thinner side along the tube length, the tube can rotate towards various directions at different pressure levels. Additional studies could explore realization of these origami at a large scale where the thickness of panels would need to be accommodated, and creases would need to undergo large strains without failure. Finally, the pop-up stable state is likely not limited to the Kresling origami. A statistical model from a topological perspective would explore the relationship between different crease patterns and this type of pop-up behavior.

## CHAPTER 5

# Conclusion

The goal of this thesis is to harness buckling in origami tubes for beneficial properties. To explore the novel mechanical functionalities, I investigate three origami tube designs that experience different improvements brought by buckling. This thesis discusses three representative application of the buckling phenomenon in tubular origami structures. In this work, I propose a deployable tubular energy absorber with a self-locking mechanism. Through finite element simulations and experimental tests, I evaluate the tunable energy-absorbing performance and find out the optimal design for various scenarios. I extend, verify, and utilize the bar and hinge model for curved-crease origami to model of thin-walled corrugated tubes. Based on the reduced-order model, I systematically explore the geometric influences on the bending multi-stability. I identify the unique mechanism of buckling valley creases and quantify the subsequent stiffness tuning. I use multi-step structural analyses and eigenvalues to characterize the tunable mechanics of the conical Kresling tube. The findings presented in the thesis are a starting point to bridge the buckling phenomenon and practical applications of origami tubes, by providing demonstration of buckling benefits, understanding the underlying energy behaviors, and pointing out directions of potential applications. Future developments on fabrication, sensing, and actuation techniques can allow researchers to create practical applications that can actively tune their behaviors. In this chapter, Section 5.1 summarizes the main findings and key contributions of the thesis, and Section 5.2 outlines potential routes to further conduct research.

## 5.1 Contributions and impacts

The motivation of the thesis is to explore benefits brought by structural instability to origami tubes. In Chapter 1, I first discuss a wide spectrum of potential applications of origami structures, focusing on the recent advancements on uncovering the unique mechanics and creating novel applications of origami tubes. As a subcategory of thin-walled structures, their surfaces can experience structural instabilities that unlock numerous features, such as improved energy-absorbing perfor-

mance, multi-stability, and tunable mechanics.

Chapter 2 introduces a deployable energy absorber based on the zipper-coupled origami tube that can be deployed to and locked at various configurations without involving panel deformations. By locking both ends of the tube, the system will behave drastically different at different deployment ratios. When it is half-deployed, the tube can be elastically compressed as the locking barely constraints the kinematic folding motion. When it is deployed to a longer extension, the tube become a stiff structure that requires buckling and plastic yielding to compress longitudinally. Therefore, more impact energy can be absorbed, while the peak reaction force is also increased. In comparison with the conventional tube, the proposed zipper tube shows lower peak force and more energy absorption. Through a series of parametric studies, I find that a tube with fewer segments and greater panel aspect ratios can crush with more plasticity and absorb more energy, and the vertex angle controls how tunable the system is. Finally, I demonstrate the self-locking of the tube with a zip-tie mechanism.

In Chapter 3, I focus the understanding of geometric influences on the multi-stability of thin-walled corrugated tubes with curved creases. To explore the geometry-driven bending stabilities, I extend and verify a reduced-order bar and hinge model that was designed for capturing the elastic response of curved-crease origami structures [84]. The model provides rapid and accurate predictions with less convergence issues , and it is calibrated with respect to a high-fidelity FE model. I find that, for a corrugated tube with circular cross-sections, a stable bending state requires thinner shells, steeper cones, and a lower stiffness of the connecting creases. By varying the cross-sections, I find the bending bi-stability is favored by deep and convex cross sections. All these measures increase the relative amount of stretching energy to bending and folding energy.

Chapter 4 presents an origami design of corrugated tubes that shows tunable stiffness via a unique pop-up mechanism. By buckling the valley creases, a twisted Kresling unit can be popped into a dome-like stable shape, which can be stiffer than the initial state by several orders of magnitude. I use an elasticity-based bar and hinge model to quantify the shape-morphing and the subsequent stiffness tuning. After the pop-up, the crease network is distorted, and the flexible twisting motion will be prohibited. As a result, the global deformation will require more panel stretching rather than the crease folding, leading to a substantial increase of stiffness. A parametric study shows that a shallower and more twisted Kresling unit offers more significant stiffness tuning. Based on the shape-morphing and tunable stiffness, I propose three potential applications, including a tunable energy absorber, a deployable traffic cone, and an adaptable robotic arm.

## 5.2 Suggestions for future work

The multi-stability and tunable properties that are presented in previous chapters, although complete, inspire research directions that can be either pursued in the near future, or envisioned in the long term.

### 5.2.1 Continuing work from the thesis

There are several research aims that can be immediately pursued to expand the application scope and to deepen our understanding of the buckling mechanics of origami tubes.

#### 5.2.1.1 The influence of imperfection on the buckling-induced functions

While numerical simulation is a powerful tool to understand the underlying mechanics, experimental tests are still crucial for validating the results and demonstrating the practical use. From the geometry perspective, the physical parameters of the testing sample can deviate from the desired values due to unavoidable errors of the fabrications process. Such imperfections may change the mechanical properties of the fabricated samples, e.g., the foldability and stiffness of the Miura-ori sheet [127]. However, only few previous studies have been performed regarding the influences of imperfection on the buckling-induced behaviors in origami tubes. In other words, how robust are the multi-stability and the associated tunable properties? It would be worthwhile to introduce random geometric imperfections in the numerical model to explore the change of the mechanics. For instance, if the panel dimension or the vertex angle varies in the zipper-coupled tube, how much would the energy absorption be different? Additionally, if there is a small fracture around the crease lines of the Kresling cone (which is likely to be true for a paper prototype), how different would the pop-up stability map be? Systematic answers to these questions would help us to understand the practical performance of origami tubes with buckling.

#### 5.2.1.2 Crease buckling for other origami patterns

In Chapter 4, I identify and investigate the bi-stable pop-up mechanism in the Kresling cone. By buckling the valley creases outwards, the Kresling cone will be converted into a dome-like shape and gain a substantial increase in stiffness. Such pop-up mechanism is unlikely to be limited to the conical Kresling geometry. One can extend the research on bi-stable pop-up of creases to other origami structures to explore: i) the existence of multi-stability, ii) the shape-morphing, and iii) the property change.

### 5.2.1.3 Tunable properties beyond the mechanical stage

With the shape-morphing and stiffness tuning of the pop-up mechanism, I propose three conceptual applications that focus on the mechanical properties. The shape-morphing would also enable tunable properties in other engineering disciplines. For instance, origami-based antennas can adapt their electromagnetic behaviors by morphing their shapes [128]. Future work along such direction could push multidisciplinary origami applications.

## 5.2.2 Long-term future work

In the previous chapters, I demonstrated the multi-stability and tunable properties through numerical simulations and experimental prototypes. In practical applications, origami-inspired smart systems are expected to actively change their properties in response to external stimuli. Several research directions can thus be inspired by the need of filling the gap between experimental demonstration and commercial implementation.

### 5.2.2.1 Fluidic actuation and tuning

Origami-inspired structures can often be reconfigured to change their shapes and to realize various functions, and I have investigated the tunable properties in Chapter 2 and 4. Those prototypes are manually actuated to demonstrate the tunability, while practical applications require advanced actuation methods to actively changes their shapes and associated functions. As inspired by the continuity benefit of origami tubes, one can use fluidic pressure to initiate a prescribed global shape change and the subsequent property tuning. Unlike a cable-driven system that is composed of external motors and wires, the actuating fluids can be consolidated into the system so that there is no distinction between actuators and structures. As a result, pneumatic actuation will perform functions beyond the scope of forcing shape changes and be able to tune the system behavior. Here, I list three research topics for exploiting the great potential brought by pressurization in origami.

**Tailoring multi-stability** Since the actuating fluid is an integrated component of the system and the work done by pressure is conservative, the potential energy of pressure is now included in the system energy. Let  $P$  denotes the pressure difference (internal - external),  $V$  denotes the enclosed volume, then the system energy can be written as the summation of strain energy and potential energy of pressure

$$\Pi = \Pi_S + \Pi_P(P, V) \quad (5.1)$$

The multi-stability, which is characterized by the system energy landscape, thus can be altered by both the structural design and the fluid pressure. Based on the nonlinear relationship between the volume and folding kinematics, Li et al. have successfully manipulated the stability type and stable configurations for a rigid origami tube based on the Miura-ori pattern [19]. Nonetheless, the deformation of origami panels has not been considered, while our results indicate that the panel stretching and bending can substantially affect the multi-stable behavior. In order to explore the pressurized influences of panel-deformable origami, it would first be needed to extend the bar and hinge model to capture the pressurized response rapidly yet accurately. Then the reduced-order model could explore three potential changes brought by fluidic pressure: i) a mono-stable origami can be bi/multi-stable when pressurized at certain levels; ii) a multi-stable origami (e.g. the Kresling cone) can lose the multi-stability after being pressurized; iii) changes of the stable configurations. Those effects would then be verified by fabricating and testing origami prototypes.

**Tune the tunability** By pressurizing reconfigurable origami structures, the tunable property can be further programmed by the pressure level. For example, stiffness tuning of the Kresling cone is determined by the initial geometry and material properties. In other words, once the origami cone is fabricated, the stiffness ratio  $\lambda_K = K_P/K_O$  cannot be changed (Fig. 5.1A). In pressurized origami, such property ratio is a function of the pressure difference  $P$ , thus it can be altered by manipulating the pressure level. The same idea can also be extended to rigid-foldable origami structures. For the deployable energy absorber presented in Chapter 2, the energy ratio can be tuned by changing the pressure level (Fig. 5.1B).

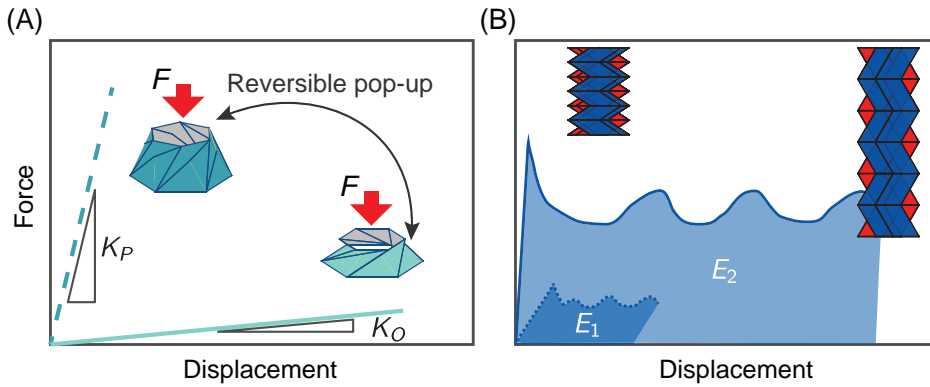


Figure 5.1: Program the tunability in (A) multi-stable origami and (B) rigid-foldable origami with internal pressure.

### 5.2.2.2 Fabrication techniques

Numerical analyses and experimental investigations have revealed numerous benefits brought by origami. However, in order to realize those great potentials in commercial applications, it is still necessary to figure out how to mass produce origami-inspired structures, while preserving their unique properties. Suitable fabrication techniques will need to be explored and developed to overcome the current limitations listed below.

**Paper-based origami** At meso-scales, origami structures can be easily fabricated by manually folding paper sheets with perforated patterns. Paper-based origami shows more modes beyond rigid kinematics, e.g., the crease buckling presented in Chapter 4 and the vertex pop-through [11]. Therefore, paper sheets are often selected for prototyping experimental samples that will be used to verify numerical predictions. Nonetheless, during the folding process, paper fibers near creases and vertices are yielded and permanently damaged, and the origami structures are prone to tears and breaks. As a result, paper is not a suitable material when the airtightness is required in making pneumatic origami structures. Paper is also not an ideal choice for manufacturing meter-scale origami structures. When scaling up, panels need to be thickened to provide enough bending stiffness, whereas folding thicker paper sheets will lead to significantly more damage of local material near creases.

**Large-scale origami with mechanical hinges** Due to the scaling limitation of paper creases, mechanical hinges have been involved in the fabrication of large-scale origami. Figure 5.2 shows the creases and vertices of a meter-scale origami tube made of corrugated plastic panels and piano hinges. These panels are 6 mm thick to limit the out-of-plane flexibility. To accommodate the panel thickness, spacers are placed between the edges of adjacent panels. Thus, the structure is not air-tight, and the creases cannot be buckled to achieve the pop-up deformation.

As a summary, it is worthwhile to explore different materials for fabricating origami structures, such as fiber-reinforced composites with large tolerance for large strains. Design methods to make thick but air-tight origami should also be studied.



Figure 5.2: The zoom-in view of a meter-scale origami tube assembled by connecting corrugated panels with piano hinges (tube courtesy: Anna Jia and Yi Zhu).

## BIBLIOGRAPHY

- [1] J. A. Faber, A. F. Arrieta, A. R. Studart, Bioinspired spring origami, *Science* 359 (6382) (2018) 1386–1391. [doi:10.1126/science.aap7753](https://doi.org/10.1126/science.aap7753).
- [2] E. T. Filipov, G. H. Paulino, T. Tachi, Origami tubes with reconfigurable polygonal cross-sections, *Proceedings of the Royal Society of London A: Mathematical, Physical and Engineering Sciences* 472 (2185). [doi:10.1098/rspa.2015.0607](https://doi.org/10.1098/rspa.2015.0607).
- [3] E. T. Filipov, T. Tachi, G. H. Paulino, Origami tubes assembled into stiff, yet reconfigurable structures and metamaterials, *Proceedings of the National Academy of Sciences* 112 (40) (2015) 12321–12326. [doi:10.1073/pnas.1509465112](https://doi.org/10.1073/pnas.1509465112).
- [4] J. Kim, D. Y. Lee, S. R. Kim, K. J. Cho, A self-deployable origami structure with locking mechanism induced by buckling effect, in: 2015 IEEE International Conference on Robotics and Automation (ICRA), 2015, pp. 3166–3171. [doi:10.1109/ICRA.2015.7139635](https://doi.org/10.1109/ICRA.2015.7139635).
- [5] M. Schenk, A. D. Viquerat, K. A. Seffen, S. D. Guest, Review of Inflatable Booms for Deployable Space Structures: Packing and Rigidization, *Journal of Spacecraft and Rockets* 51 (3) (2014) 762–778. [doi:10.2514/1.A32598](https://doi.org/10.2514/1.A32598).
- [6] J. M. Gattas, Z. You, Geometric assembly of rigid-foldable morphing sandwich structures, *Engineering Structures* 94 (2015) 149–159. [doi:10.1016/j.engstruct.2015.03.019](https://doi.org/10.1016/j.engstruct.2015.03.019).
- [7] S.-J. Kim, D.-Y. Lee, G.-P. Jung, K.-J. Cho, An origami-inspired, self-locking robotic arm that can be folded flat, *Science Robotics* 3 (16) (2018) eaar2915. [doi:10.1126/scirobotics.aar2915](https://doi.org/10.1126/scirobotics.aar2915).
- [8] Z. Zhai, Y. Wang, H. Jiang, Origami-inspired, on-demand deployable and collapsible mechanical metamaterials with tunable stiffness, *Proceedings of the National Academy of Sciences* 115 (9) (2018) 2032–2037. [doi:10.1073/pnas.1720171115](https://doi.org/10.1073/pnas.1720171115).
- [9] E. Boatti, N. Vasios, K. Bertoldi, Origami Metamaterials for Tunable Thermal Expansion, *Advanced Materials* 29 (26) (2017) 1700360. [doi:10.1002/adma.201700360](https://doi.org/10.1002/adma.201700360).
- [10] Z. Wang, L. Jing, K. Yao, Y. Yang, B. Zheng, C. M. Soukoulis, H. Chen, Y. Liu, Origami-Based Reconfigurable Metamaterials for Tunable Chirality, *Advanced Materials* 29 (27) (2017) 1700412. [doi:10.1002/adma.201700412](https://doi.org/10.1002/adma.201700412).

- [11] J. L. Silverberg, A. A. Evans, L. McLeod, R. C. Hayward, T. Hull, C. D. Santangelo, I. Cohen, Using origami design principles to fold reprogrammable mechanical metamaterials, *Science* 345 (6197) (2014) 647–650. [doi:10.1126/science.1252876](https://doi.org/10.1126/science.1252876).
- [12] Z. Zhai, Y. Wang, K. Lin, L. Wu, H. Jiang, In situ stiffness manipulation using elegant curved origami, *Science Advances* 6 (47) (2020) eabe2000. [doi:10.1126/sciadv.abe2000](https://doi.org/10.1126/sciadv.abe2000).
- [13] S. Sengupta, S. Li, Harnessing the anisotropic multistability of stacked-origami mechanical metamaterials for effective modulus programming, *Journal of Intelligent Material Systems and Structures* 29 (14) (2018) 2933–2945. [doi:10.1177/1045389X18781040](https://doi.org/10.1177/1045389X18781040).
- [14] Z. Zhao, X. Kuang, J. Wu, Q. Zhang, G. H. Paulino, H. J. Qi, D. Fang, 3D printing of complex origami assemblages for reconfigurable structures, *Soft Matter* 14 (39) (2018) 8051–8059. [doi:10.1039/C8SM01341A](https://doi.org/10.1039/C8SM01341A).
- [15] B. Tepavčević, V. Stojaković, D. Mitov, I. Bajšanski, M. Jovanović, Design to fabrication method of thin shell structures based on a friction-fit connection system, *Automation in Construction* 84 (2017) 207–213. [doi:10.1016/j.autcon.2017.09.003](https://doi.org/10.1016/j.autcon.2017.09.003).
- [16] S. Felton, M. Tolley, E. Demaine, D. Rus, R. Wood, A method for building self-folding machines, *Science* 345 (6197) (2014) 644–646. [doi:10.1126/science.1252610](https://doi.org/10.1126/science.1252610).
- [17] Z. Zhao, J. Wu, X. Mu, H. Chen, H. J. Qi, D. Fang, Origami by frontal photopolymerization, *Science Advances* 3 (4) (2017) e1602326. [doi:10.1126/sciadv.1602326](https://doi.org/10.1126/sciadv.1602326).
- [18] B. An, S. Miyashita, M. Tolley, D. M. Aukes, L. Meeker, E. D. Demaine, M. L. Demaine, R. J. Wood, D. Rus, An end-to-end approach to making self-folded 3D surface shapes by uniform heating, in: 2014 IEEE International Conference on Robotics and Automation (ICRA), 2014, pp. 1466–1473. [doi:10.1109/ICRA.2014.6907045](https://doi.org/10.1109/ICRA.2014.6907045).
- [19] S. Li, K. W. Wang, Fluidic origami with embedded pressure dependent multi-stability: a plant inspired innovation, *Journal of The Royal Society Interface* 12 (111). [doi:10.1098/rsif.2015.0639](https://doi.org/10.1098/rsif.2015.0639).
- [20] F. Pan, Y. Li, Z. Li, J. Yang, B. Liu, Y. Chen, 3D Pixel Mechanical Metamaterials, *Advanced Materials* 31 (25) (2019) 1900548. [doi:10.1002/adma.201900548](https://doi.org/10.1002/adma.201900548).
- [21] C. du Pasquier, T. Chen, S. Tibbits, K. Shea, Design and Computational Modeling of a 3D Printed Pneumatic Toolkit for Soft Robotics, *Soft Robotics* 6 (5) (2019) 657–663. [doi:10.1089/soro.2018.0095](https://doi.org/10.1089/soro.2018.0095).
- [22] S. Wu, Q. Ze, J. Dai, N. Udupi, G. H. Paulino, R. Zhao, Stretchable origami robotic arm with omnidirectional bending and twisting, *Proceedings of the National Academy of Sciences* 118 (36) (2021) e2110023118. [doi:10.1073/pnas.2110023118](https://doi.org/10.1073/pnas.2110023118).
- [23] E. T. Filipov, G. H. Paulino, T. Tachi, Deployable Sandwich Surfaces with High Out-of-Plane Stiffness, *Journal of Structural Engineering* 145 (2) (2019) 4018244. [doi:10.1061/\(ASCE\)ST.1943-541X.0002240](https://doi.org/10.1061/(ASCE)ST.1943-541X.0002240).

- [24] L. Wilson, S. Pellegrino, R. Danner, Origami Sunshield Concepts for Space Telescopes, Structures, Structural Dynamics, and Materials Conferences, American Institute of Aeronautics and Astronautics, Boston, Massachusetts, 2013. [doi:10.2514/6.2013-1594](https://doi.org/10.2514/6.2013-1594).
- [25] C. Burns, Giant accordian relief - yanko design, <https://www.yankodesign.com/2008/08/29/disaster-survivors-choose-giant-accordian-tm/>, Accessed: 2022-08-23.
- [26] P. Sareh, P. Chermprayong, M. Emmanuelli, H. Nadeem, M. Kovac, Rotororigami: A rotary origami protective system for robotic rotorcraft, *Science Robotics* 3 (22) (2018) eaah5228. [doi:10.1126/scirobotics.aah5228](https://doi.org/10.1126/scirobotics.aah5228).
- [27] Y. Zhu, M. Birla, K. R. Oldham, E. T. Filipov, Elastically and Plastically Foldable Electrothermal Micro-Origami for Controllable and Rapid Shape Morphing, *Advanced Functional Materials* 30 (40) (2020) 2003741. [doi:10.1002/adfm.202003741](https://doi.org/10.1002/adfm.202003741).
- [28] Q. Liu, W. Wang, M. F. Reynolds, M. C. Cao, M. Z. Miskin, T. A. Arias, D. A. Muller, P. L. McEuen, I. Cohen, Micrometer-sized electrically programmable shape-memory actuators for low-power microrobotics, *Science Robotics* 6 (52) (2021) eabe6663. [doi:10.1126/scirobotics.abe6663](https://doi.org/10.1126/scirobotics.abe6663).
- [29] L. Lu, X. Dang, F. Feng, P. Lv, H. Duan, Conical Kresling origami and its applications to curvature and energy programming, *Proceedings of the Royal Society A: Mathematical, Physical and Engineering Sciences* 478 (2257) (2022) 20210712. [doi:10.1098/rspa.2021.0712](https://doi.org/10.1098/rspa.2021.0712).
- [30] J.-E. Suh, Y. Miyazawa, J. Yang, J.-H. Han, Self-Reconfiguring and Stiffening Origami Tube, *Advanced Engineering Materials* 24 (5) (2022) 2101202. [doi:10.1002/adem.202101202](https://doi.org/10.1002/adem.202101202).
- [31] M. Schenk, S. D. Guest, Geometry of Miura-folded metamaterials, *Proceedings of the National Academy of Sciences* 110 (9) (2013) 3276–3281. [doi:10.1073/pnas.1217998110](https://doi.org/10.1073/pnas.1217998110).
- [32] K. Yang, S. Xu, J. Shen, S. Zhou, Y. M. Xie, Energy absorption of thin-walled tubes with pre-folded origami patterns: Numerical simulation and experimental verification, *Thin-Walled Structures* 103 (2016) 33–44. [doi:10.1016/j.tws.2016.02.007](https://doi.org/10.1016/j.tws.2016.02.007).
- [33] Q. Ze, S. Wu, J. Nishikawa, J. Dai, Y. Sun, S. Leanza, C. Zemelka, L. S. Novelino, G. H. Paulino, R. R. Zhao, Soft robotic origami crawler, *Science Advances* 8 (13) (2022) eabm7834. [doi:10.1126/sciadv.abm7834](https://doi.org/10.1126/sciadv.abm7834).
- [34] D. Melancon, B. Gorissen, C. J. Garca-Mora, C. Hoberman, K. Bertoldi, Multistable inflatable origami structures at the metre scale, *Nature* 592 (2021) 545–550. [doi:10.1038/s41586-021-03407-4](https://doi.org/10.1038/s41586-021-03407-4).
- [35] L. Dae-Young, K. Jae-Kyeong, S. Chang-Young, H. Jeong-Mu, C. Kyu-Jin, High-load capacity origami transformable wheel, *Science Robotics* 6 (2021) eabe0201, doi: 10.1126/scirobotics.abe0201. [doi:10.1126/scirobotics.abe0201](https://doi.org/10.1126/scirobotics.abe0201).

- [36] J. Ma, Z. You, Energy Absorption of Thin-Walled Square Tubes With a Prefolded Origami PatternPart I: Geometry and Numerical Simulation, *Journal of Applied Mechanics* 81 (1) (2013) 11003–11011. [doi:10.1115/1.4024405](https://doi.org/10.1115/1.4024405).
- [37] R. Sachse, A. Westermeier, M. Mylo, J. Nadasdi, M. Bischoff, T. Speck, S. Poppinga, Snapping mechanics of the Venus flytrap (*Dionaea muscipula*), *Proceedings of the National Academy of Sciences* 117 (27) (2020) 16035 – 16042. [doi:10.1073/pnas.2002707117](https://doi.org/10.1073/pnas.2002707117).
- [38] B. Gorissen, D. Melancon, N. Vassios, M. Torbati, K. Bertoldi, Inflatable soft jumper inspired by shell snapping, *Science Robotics* 5 (2020) eabb1967. [doi:10.1126/scirobotics.abb1967](https://doi.org/10.1126/scirobotics.abb1967).
- [39] Z. Yan, F. Zhang, J. Wang, F. Liu, X. Guo, K. Nan, Q. Lin, M. Gao, D. Xiao, Y. Shi, Y. Qiu, H. Luan, J. H. Kim, Y. Wang, H. Luo, M. Han, Y. Huang, Y. Zhang, J. A. Rogers, Controlled mechanical buckling for origami-inspired construction of 3d microstructures in advanced materials, *Advanced Functional Materials* 26 (2016) 2629–2639. [doi:10.1002/adfm.201504901](https://doi.org/10.1002/adfm.201504901).
- [40] D. Melancon, A. E. Forte, L. M. Kamp, B. Gorissen, K. Bertoldi, Inflatable Origami: Multimodal Deformation via Multistability, *Advanced Functional Materials* 32 (35) (2022) 2201891. [doi:10.1002/adfm.202201891](https://doi.org/10.1002/adfm.202201891).
- [41] N. P. Bende, T. Yu, N. A. Corbin, M. A. Dias, C. D. Santangelo, J. A. Hanna, R. C. Hayward, Overcurvature induced multistability of linked conical frusta: how a bendy straw' holds its shape, *Soft Matter* 14 (42) (2018) 8636–8642. [doi:10.1039/C8SM01355A](https://doi.org/10.1039/C8SM01355A).
- [42] Y. Liu, F. Pan, B. Ding, Y. Zhu, K. Yang, Y. Chen, Multistable shape-reconfigurable metawire in 3D space, *Extreme Mechanics Letters* 50 (2021) 101535. [doi:10.1016/j.eml.2021.101535](https://doi.org/10.1016/j.eml.2021.101535).
- [43] A. Márquez, P. G. Fazzini, J. L. Otegui, Failure analysis of flexible metal hose at compressor discharge, *Engineering Failure Analysis* 16 (6) (2009) 1912–1921. [doi:10.1016/j.engfailanal.2008.09.031](https://doi.org/10.1016/j.engfailanal.2008.09.031).
- [44] F. C. Bardi, H. Tang, M. Kulkarni, X. Yin, Structural Analysis of Cryogenic Flexible Hose, in: Proceedings of the ASME 2011 30th International Conference on Ocean, Offshore and Arctic Engineering, Vol. 3: Materials Technology; Jan Vugts Symposium on Design Methodology of Offshore Structures; Jo Pinkster Symposium on Second Order Wave Drift Forces, ASME, Rotterdam, The Netherlands, 2011, pp. 593–606. [doi:10.1115/OMAE2011-50238](https://doi.org/10.1115/OMAE2011-50238).
- [45] Z. Wo, J. M. Raneses, E. T. Filipov, Locking Zipper-Coupled Origami Tubes for Deployable Energy Absorption, *Journal of Mechanisms and Robotics* 14 (4) (2022) 041007. [doi:10.1115/1.4054363](https://doi.org/10.1115/1.4054363).
- [46] Z. Wo, E. T. Filipov, Bending Stability of Corrugated Tubes With Anisotropic Frustum Shells, *Journal of Applied Mechanics* 89 (4) (2022) 041005. [doi:10.1115/1.4053267](https://doi.org/10.1115/1.4053267).

- [47] R. Imada, T. Tachi, Geometry and kinematics of cylindrical waterbomb tessellation, *Journal of Mechanisms and Robotics* 14 (2022) 041009. [doi:10.1115/1.4054478](https://doi.org/10.1115/1.4054478).
- [48] J. B. Friedman, Flexible drinking straw (U.S. Patent, May 1 1951).
- [49] C. Jianguo, D. Xiaowei, Z. Ya, F. Jian, T. Yongming, Bistable Behavior of the Cylindrical Origami Structure With Kresling Pattern, *Journal of Mechanical Design* 137 (6) (2015) 061406. [doi:10.1115/1.4030158](https://doi.org/10.1115/1.4030158).
- [50] H. Yasuda, T. Tachi, M. Lee, J. Yang, Origami-based tunable truss structures for non-volatile mechanical memory operation, *Nature Communications* 8 (1) (2017) 962. [doi:10.1038/s41467-017-00670-w](https://doi.org/10.1038/s41467-017-00670-w).
- [51] M. Zhang, J. Yang, R. Zhu, Origami-Based Bistable Metastructures for Low-Frequency Vibration Control, *Journal of Applied Mechanics* 88 (5) (2021) 051009. [doi:10.1115/1.4049953](https://doi.org/10.1115/1.4049953).
- [52] J. Kaufmann, P. Bhowad, S. Li, Harnessing the Multistability of Kresling Origami for Reconfigurable Articulation in Soft Robotic Arms, *Soft Robotics* 9 (2) (2022) 212–223. [doi:10.1089/soro.2020.0075](https://doi.org/10.1089/soro.2020.0075).
- [53] X. M. Xiang, G. Lu, Z. You, Energy absorption of origami inspired structures and materials, *Thin-Walled Structures* 157 (2020) 107130. [doi:10.1016/j.tws.2020.107130](https://doi.org/10.1016/j.tws.2020.107130).
- [54] H. Fang, Y. Zhang, K. W. Wang, Origami-based earthworm-like locomotion robots, *Bioinspiration & Biomimetics* 12 (2017) 65003. [doi:10.1088/1748-3190/aa8448](https://doi.org/10.1088/1748-3190/aa8448).
- [55] T. Wierzbicki, W. Abramowicz, On the Crushing Mechanics of Thin-Walled Structures, *Journal of Applied Mechanics* 50 (4a) (1983) 727–734. [doi:10.1115/1.3167137](https://doi.org/10.1115/1.3167137).
- [56] K. Yang, S. Xu, S. Zhou, Y. M. Xie, Multi-objective optimization of multi-cell tubes with origami patterns for energy absorption, *Thin-Walled Structures* 123 (2018) 100–113. [doi:10.1016/j.tws.2017.11.005](https://doi.org/10.1016/j.tws.2017.11.005).
- [57] J. Ma, D. Hou, Y. Chen, Z. You, Quasi-static axial crushing of thin-walled tubes with a kite-shape rigid origami pattern: Numerical simulation, *Thin-Walled Structures* 100 (2016) 38–47. [doi:10.1016/j.tws.2015.11.023](https://doi.org/10.1016/j.tws.2015.11.023).
- [58] J. Qi, C. Li, Y. Tie, Y. Zheng, Y. Duan, Energy absorption characteristics of origami-inspired honeycomb sandwich structures under low-velocity impact loading, *Materials & Design* 207 (2021) 109837. [doi:10.1016/j.matdes.2021.109837](https://doi.org/10.1016/j.matdes.2021.109837).
- [59] M. Meloni, J. Cai, Q. Zhang, D. Sang-Hoon Lee, M. Li, R. Ma, T. E. Parashkevov, J. Feng, Engineering origami: A comprehensive review of recent applications, design methods, and tools, *Advanced Science* 8 (13) (2021) 2000636. [doi:10.1002/advs.202000636](https://doi.org/10.1002/advs.202000636).
- [60] J. U. Surjadi, L. Gao, H. Du, X. Li, X. Xiong, N. X. Fang, Y. Lu, Mechanical Metamaterials and Their Engineering Applications, *Advanced Engineering Materials* 21 (3) (2019) 1800864. [doi:10.1002/adem.201800864](https://doi.org/10.1002/adem.201800864).

- [61] S. Shan, S. H. Kang, J. R. Raney, P. Wang, L. Fang, F. Candido, J. A. Lewis, K. Bertoldi, Multistable Architected Materials for Trapping Elastic Strain Energy, *Advanced Materials* 27 (29) (2015) 4296–4301. [doi:10.1002/adma.201501708](https://doi.org/10.1002/adma.201501708).
- [62] Z. Wo, J. M. Raneses, E. T. Filipov, A Numerical and Experimental Study on the Energy Absorption Characteristics of Deployable Origami Tubes, in: Proceedings of the ASME 2021 International Design Engineering Technical Conferences and Computers and Information in Engineering Conference, Vol. 8B: 45th Mechanisms and Robotics Conference (MR), 2021, p. V08BT08A029. [doi:10.1115/DETC2021-66723](https://doi.org/10.1115/DETC2021-66723).
- [63] K. Miura, Method of packaging and deployment of large membranes in space, *Inst. of Space and Astronautical Science* 618 (1985) 1–9.
- [64] Q. Zhang, X. Wang, D. S. hoon Lee, J. Cai, Z. Ren, J. Feng, Development of kinetic origami canopy using arc miura folding patterns, *Journal of Building Engineering* 43 (2021) 103116. [doi:10.1016/j.jobe.2021.103116](https://doi.org/10.1016/j.jobe.2021.103116).
- [65] E. T. Filipov, T. Tachi, G. H. Paulino, Coupled Origami Tubes for Stiff Deployable Cantilevers, in: Proceedings of the ASME 2019 International Design Engineering Technical Conferences and Computers and Information in Engineering Conference, Vol. 5B: 43rd Mechanisms and Robotics Conference, 2019, p. V05BT07A023. [doi:10.1115/DETC2019-97096](https://doi.org/10.1115/DETC2019-97096).
- [66] ABAQUS, Abaqus FEA, Version 6.10 documentation (2010).
- [67] E. T. Filipov, K. Liu, T. Tachi, M. Schenk, G. H. Paulino, Bar and hinge models for scalable analysis of origami, *International Journal of Solids and Structures* 124 (2017) 26–45. [doi:10.1016/j.ijsolstr.2017.05.028](https://doi.org/10.1016/j.ijsolstr.2017.05.028).
- [68] F. Lechenault, B. Thiria, M. Adda-Bedia, Mechanical Response of a Creased Sheet, *Phys. Rev. Lett.* 112 (24) (2014) 244301. [doi:10.1103/PhysRevLett.112.244301](https://doi.org/10.1103/PhysRevLett.112.244301).
- [69] M. Sharifzadeh, Y. Jiang, R. Khodambashi, D. Aukes, Increasing the Life Span of Foldable Manipulators With Fabric, in: Proceedings of the ASME 2020 International Design Engineering Technical Conferences and Computers and Information in Engineering Conference, Vol. 10: 44th Mechanisms and Robotics Conference (MR), Virtual, Online, 2020, p. V010T10A087. [doi:10.1115/DETC2020-22757](https://doi.org/10.1115/DETC2020-22757).
- [70] S. Yuan, C. K. Chua, K. Zhou, 3D-Printed Mechanical Metamaterials with High Energy Absorption, *Advanced Materials Technologies* 4 (3) (2019) 1800419. [doi:10.1002/admt.201800419](https://doi.org/10.1002/admt.201800419).
- [71] N. P. Bende, A. A. Evans, S. Innes-Gold, L. A. Marin, I. Cohen, R. C. Hayward, C. D. Santangelo, Geometrically controlled snapping transitions in shells with curved creases, *Proceedings of the National Academy of Sciences* 112 (36) (2015) 11175–11180. [doi:10.1073/pnas.1509228112](https://doi.org/10.1073/pnas.1509228112).

- [72] J. Shim, C. Perdigou, E. R. Chen, K. Bertoldi, P. M. Reis, Buckling-induced encapsulation of structured elastic shells under pressure, *Proceedings of the National Academy of Sciences* 109 (16) (2012) 5978–5983. [doi:10.1073/pnas.1115674109](https://doi.org/10.1073/pnas.1115674109).
- [73] A. Reid, F. Lechenault, S. Rica, M. Adda-Bedia, Geometry and design of origami bellows with tunable response, *Phys. Rev. E* 95 (1) (2017) 13002. [doi:10.1103/PhysRevE.95.013002](https://doi.org/10.1103/PhysRevE.95.013002).
- [74] B. Li, Y.-P. Cao, X.-Q. Feng, H. Gao, Mechanics of morphological instabilities and surface wrinkling in soft materials: a review, *Soft Matter* 8 (21) (2012) 5728–5745. [doi:10.1039/C2SM00011C](https://doi.org/10.1039/C2SM00011C).
- [75] N. Hu, R. Burgueño, Buckling-induced smart applications: recent advances and trends, *Smart Materials and Structures* 24 (6) (2015) 63001. [doi:10.1088/0964-1726/24/6/063001](https://doi.org/10.1088/0964-1726/24/6/063001).
- [76] B. Zhang, Bistable and multi-stable thin-walled structures, Ph.D. thesis, University of Oxford, Oxford, UK (2017).
- [77] J. Shandro, A coaxial circle circuit: Comparison with conventional circle and bain circuit, *Canadian Anaesthetists' Society Journal* 29 (2) (1982) 121–125. [doi:10.1007/BF03007989](https://doi.org/10.1007/BF03007989).
- [78] R. Garg, Kinked inner tube of coaxial Bain circuit—need for corrugated inner tube, *Journal of Anesthesia* 23 (2) (2009) 306. [doi:10.1007/s00540-008-0719-y](https://doi.org/10.1007/s00540-008-0719-y).
- [79] K. C. Francis, L. T. Rupert, R. J. Lang, D. C. Morgan, S. P. Magleby, L. L. Howell, From Crease Pattern to Product: Considerations to Engineering Origami-Adapted Designs, in: *Proceedings of the ASME 2014 International Design Engineering Technical Conferences and Computers and Information in Engineering Conference*, Vol. 5B: 38th Mechanisms and Robotics Conference, ASME, Buffalo, New York, USA, 2014, p. V05BT08A030. [doi:10.1115/DETC2014-34031](https://doi.org/10.1115/DETC2014-34031).
- [80] B. Ni, H. Gao, Engineer Energy Dissipation in 3D Graphene Nanolattice Via Reversible Snap-Through Instability, *Journal of Applied Mechanics* 87 (3) (2019) 031012. [doi:10.1115/1.4045544](https://doi.org/10.1115/1.4045544).
- [81] M. Schenk, S. D. Guest, Origami folding: A structural engineering approach, in: P. Wang-Iverson, R. J. Lang, M. Yims (Eds.), *Origami 5: Fifth International Meeting of Origami Science, Mathematics, and Education*, CRC Press, New York, 2011, pp. 291–303.
- [82] K. Liu, G. H. Paulino, Nonlinear mechanics of non-rigid origami: an efficient computational approach, *Proceedings of the Royal Society of London A: Mathematical, Physical and Engineering Sciences* 473 (2206) (2017) 20170348. [doi:10.1098/rspa.2017.0348](https://doi.org/10.1098/rspa.2017.0348).
- [83] S. R. Woodruff, E. T. Filipov, Curved creases redistribute global bending stiffness in corrugations: theory and experimentation, *Meccanica* 56 (6) (2021) 1613–1634. [doi:10.1007/s11012-020-01200-7](https://doi.org/10.1007/s11012-020-01200-7).

- [84] S. R. Woodruff, E. T. Filipov, A bar and hinge model formulation for structural analysis of curved-crease origami, *International Journal of Solids and Structures* 204-205 (2020) 114–127. [doi:10.1016/j.ijsolstr.2020.08.010](https://doi.org/10.1016/j.ijsolstr.2020.08.010).
- [85] C. Lestringant, C. Maurini, A. Lazarus, B. Audoly, Buckling of an Elastic Ridge: Competition between Wrinkles and Creases, *Phys. Rev. Lett.* 118 (16) (2017) 165501. [doi:10.1103/PhysRevLett.118.165501](https://doi.org/10.1103/PhysRevLett.118.165501).
- [86] E. Riks, An incremental approach to the solution of snapping and buckling problems, *International Journal of Solids and Structures* 15 (7) (1979) 529–551. [doi:https://doi.org/10.1016/0020-7683\(79\)90081-7](https://doi.org/10.1016/0020-7683(79)90081-7).
- [87] S. E. Leon, E. N. Lages, C. N. de Araújo, G. H. Paulino, On the effect of constraint parameters on the generalized displacement control method, *Mechanics Research Communications* 56 (2014) 123–129. [doi:10.1016/j.mechrescom.2013.12.009](https://doi.org/10.1016/j.mechrescom.2013.12.009).
- [88] K. Bertoldi, V. Vitelli, J. Christensen, M. van Hecke, Flexible mechanical metamaterials, *Nature Reviews Materials* 2 (2017) 17066. [doi:10.1038/natrevmats.2017.66](https://doi.org/10.1038/natrevmats.2017.66).
- [89] Q. Zhong, J. Zhu, F. E. Fish, S. J. Kerr, A. M. Downs, H. Bart-Smith, D. B. Quinn, Tunable stiffness enables fast and efficient swimming in fish-like robots, *Science Robotics* 6 (57) (2021) eabe4088. [doi:10.1126/scirobotics.abe4088](https://doi.org/10.1126/scirobotics.abe4088).
- [90] G. Sumbre, G. Fiorito, T. Flash, B. Hochner, Octopuses Use a Human-like Strategy to Control Precise Point-to-Point Arm Movements, *Current Biology* 16 (8) (2006) 767–772. [doi:10.1016/j.cub.2006.02.069](https://doi.org/10.1016/j.cub.2006.02.069).
- [91] Y.-J. Kim, S. Cheng, S. Kim, K. Iagnemma, A Novel Layer Jamming Mechanism With Tunable Stiffness Capability for Minimally Invasive Surgery, *IEEE Transactions on Robotics* 29 (4) (2013) 1031–1042. [doi:10.1109/TRO.2013.2256313](https://doi.org/10.1109/TRO.2013.2256313).
- [92] S. Mintchev, J. Shintake, D. Floreano, Bioinspired dual-stiffness origami, *Science Robotics* 3 (20). [doi:10.1126/scirobotics.aau0275](https://doi.org/10.1126/scirobotics.aau0275).
- [93] B. Haghpanah, L. Salari-Sharif, P. Pourrajab, J. Hopkins, L. Valdevit, Multistable Shape-Reconfigurable Architected Materials, *Advanced Materials* 28 (36) (2016) 7915–7920. [doi:10.1002/adma.201601650](https://doi.org/10.1002/adma.201601650).
- [94] F. Hongbin, C. S. A., X. Yutong, W. KonWell, Programmable SelfLocking Origami Mechanical Metamaterials, *Advanced Materials* 30 (15) (2018) 1706311. [doi:10.1002/adma.201706311](https://doi.org/10.1002/adma.201706311).
- [95] Y. Zhang, Q. Wang, M. Tichem, F. van Keulen, Design and characterization of multi-stable mechanical metastructures with level and tilted stable configurations, *Extreme Mechanics Letters* 34 (2020) 100593. [doi:10.1016/j.eml.2019.100593](https://doi.org/10.1016/j.eml.2019.100593).
- [96] D. Vella, Buffering by buckling as a route for elastic deformation, *Nature Reviews Physics* 1 (7) (2019) 425–436. [doi:10.1038/s42254-019-0063-1](https://doi.org/10.1038/s42254-019-0063-1).

- [97] D. M. Kochmann, K. Bertoldi, Exploiting Microstructural Instabilities in Solids and Structures: From Metamaterials to Structural Transitions, *Applied Mechanics Reviews* 69 (5) (2017) 50801–50824. [doi:10.1115/1.4037966](https://doi.org/10.1115/1.4037966).
- [98] D. P. Holmes, A. J. Crosby, Snapping Surfaces, *Advanced Materials* 19 (21) (2007) 3589–3593. [doi:10.1002/adma.200700584](https://doi.org/10.1002/adma.200700584).
- [99] S. Janbaz, F. S. L. Bobbert, M. J. Mirzaali, A. A. Zadpoor, Ultra-programmable buckling-driven soft cellular mechanisms, *Mater. Horiz.* 6 (6) (2019) 1138–1147. [doi:10.1039/C9MH00125E](https://doi.org/10.1039/C9MH00125E).
- [100] Y. Zhang, D. Restrepo, M. Velay-Lizancos, N. D. Mankame, P. D. Zavattieri, Energy dissipation in functionally two-dimensional phase transforming cellular materials, *Scientific Reports* 9 (1) (2019) 12581. [doi:10.1038/s41598-019-48581-8](https://doi.org/10.1038/s41598-019-48581-8).
- [101] Z. Yan, F. Zhang, F. Liu, M. Han, D. Ou, Y. Liu, Q. Lin, X. Guo, H. Fu, Z. Xie, M. Gao, Y. Huang, J. Kim, Y. Qiu, K. Nan, J. Kim, P. Gutruf, H. Luo, A. Zhao, K.-C. Hwang, Y. Huang, Y. Zhang, J. A. Rogers, Mechanical assembly of complex, 3D mesostructures from releasable multilayers of advanced materials, *Science Advances* 2 (9) (2016) e1601014. [doi:10.1126/sciadv.1601014](https://doi.org/10.1126/sciadv.1601014).
- [102] J. O. Almen, A. Laszlo, The uniform-section disc spring, *Trans. ASME* 58 (4) (1936) 305 – 314.
- [103] D. Ilssar, M. Pukshansky, Y. Or, A. D. Gat, Dynamics of reconfigurable straw-like elements (2022). [doi:10.48550/ARXIV.2202.12657](https://doi.org/10.48550/ARXIV.2202.12657).
- [104] E. Bernardes, S. Viollet, Design of an origami bendy straw for robotic multistable structures, *Journal of Mechanical Design* 144 (3) (2021) 033301. [doi:10.1115/1.4052222](https://doi.org/10.1115/1.4052222).
- [105] S. Li, H. Fang, S. Sadeghi, P. Bhovad, K.-W. Wang, Architected Origami Materials: How Folding Creates Sophisticated Mechanical Properties, *Advanced Materials* 31 (5) (2019) 1805282. [doi:10.1002/adma.201805282](https://doi.org/10.1002/adma.201805282).
- [106] Z. Zhai, L. Wu, H. Jiang, Mechanical metamaterials based on origami and kirigami, *Applied Physics Reviews* 8 (4) (2021) 41319. [doi:10.1063/5.0051088](https://doi.org/10.1063/5.0051088).
- [107] J. L. Silverberg, J.-H. Na, A. A. Evans, B. Liu, T. C. Hull, C. D. Santangelo, R. J. Lang, R. C. Hayward, I. Cohen, Origami structures with a critical transition to bistability arising from hidden degrees of freedom, *Nat Mater* 14 (4) (2015) 389–393. [doi:10.1038/nmat4232](https://doi.org/10.1038/nmat4232).
- [108] E. T. Filipov, M. Redoutey, Mechanical characteristics of the bistable origami hyperbolic paraboloid, *Extreme Mechanics Letters* 25 (2018) 16–26. [doi:10.1016/j.eml.2018.10.001](https://doi.org/10.1016/j.eml.2018.10.001).
- [109] S. D. Guest, S. Pellegrino, The Folding of Triangulated Cylinders, Part I: Geometric Considerations, *Journal of Applied Mechanics* 61 (4) (1994) 773–777. [doi:10.1115/1.2901553](https://doi.org/10.1115/1.2901553).

- [110] A. Pagano, T. Yan, B. Chien, A. Wissa, S. Tawfick, A crawling robot driven by multi-stable origami, *Smart Materials and Structures* 26 (9) (2017) 94007. [doi:10.1088/1361-665x/aa721e](https://doi.org/10.1088/1361-665x/aa721e).
- [111] P. Bhovad, J. Kaufmann, S. Li, Peristaltic locomotion without digital controllers: Exploiting multi-stability in origami to coordinate robotic motion, *Extreme Mechanics Letters* 32 (2019) 100552. [doi:10.1016/j.eml.2019.100552](https://doi.org/10.1016/j.eml.2019.100552).
- [112] S. Ishida, T. Nojima, I. Hagiwara, Mathematical Approach to Model Foldable Conical Structures Using Conformal Mapping, *Journal of Mechanical Design* 136 (9) (2014) 091007. [doi:10.1115/1.4027848](https://doi.org/10.1115/1.4027848).
- [113] T. NOJIMA, Development of Foldable Conical Shell, *Transactions of the Japan Society of Mechanical Engineers Series C* 66 (647) (2000) 2463–2469. [doi:10.1299/kikaic.66.2463](https://doi.org/10.1299/kikaic.66.2463).
- [114] H. Sharma, S. H. Upadhyay, Geometric design and deployment behavior of origami inspired conical structures, *Mechanics Based Design of Structures and Machines* (2020) 1–25 [doi:10.1080/15397734.2020.1833738](https://doi.org/10.1080/15397734.2020.1833738).
- [115] Y. Zhu, M. Schenk, E. T. Filippov, A review on origami simulations: From kinematics, to mechanics, toward multiphysics, *Applied Mechanics Reviews* 74 (3) (2022) 030801. [doi:10.1115/1.4055031](https://doi.org/10.1115/1.4055031).
- [116] K. Liu, G. H. Paulino, Highly efficient nonlinear structural analysis of origami assemblages using the merlin2 software, in: R. J. Lang (Ed.), *Origami 7: Seventh International Meeting of Origami Science, Mathematics, and Education*, Vol. 4, Tarquin Group, St Albans, United Kingdom, 2018, pp. 1167–1182.
- [117] E. D. Demaine, M. L. Demaine, V. Hart, G. N. Price, T. Tachi, (Non)Existence of Pleated Folds: How Paper Folds Between Creases, *Graphs and Combinatorics* 27 (3) (2011) 377–397. [doi:10.1007/s00373-011-1025-2](https://doi.org/10.1007/s00373-011-1025-2).
- [118] B. A. DiDonna, T. A. Witten, Anomalous Strength of Membranes with Elastic Ridges, *Phys. Rev. Lett.* 87 (20) (2001) 206105. [doi:10.1103/PhysRevLett.87.206105](https://doi.org/10.1103/PhysRevLett.87.206105).
- [119] A. Lobkovsky, S. Gentges, H. Li, D. Morse, T. A. Witten, Scaling Properties of Stretching Ridges in a Crumpled Elastic Sheet, *Science* 270 (5241) (1995) 1482–1485. [doi:10.1126/science.270.5241.1482](https://doi.org/10.1126/science.270.5241.1482).
- [120] T. A. Witten, Stress focusing in elastic sheets, *Rev. Mod. Phys.* 79 (2) (2007) 643–675. [doi:10.1103/RevModPhys.79.643](https://doi.org/10.1103/RevModPhys.79.643).
- [121] S. Borodulina, A. Kulachenko, M. Nygård, S. Galland, Stress-strain curve of paper revisited, *Nordic Pulp & Paper Research Journal* 27 (2) (2012) 318–328. [doi:doi:10.3183/npprj-2012-27-02-p318-328](https://doi.org/10.3183/npprj-2012-27-02-p318-328).

- [122] C. Lauff, T. W. Simpson, M. Frecker, Z. Ounaies, S. Ahmed, P. von Lockette, R. Strzelec, R. Sheridan, J.-M. Lien, Differentiating Bending From Folding in Origami Engineering Using Active Materials, in: Proceedings of the ASME 2014 International Design Engineering Technical Conferences & Computers and Information Engineering Conference. Volume 5B: 38th Mechanisms and Robotics Conference, Buffalo, New York, USA, 2014, p. V05BT08A040. [doi:10.1115/DETC2014-34702](https://doi.org/10.1115/DETC2014-34702).
- [123] A. Giampieri, U. Perego, R. Borsari, A constitutive model for the mechanical response of the folding of creased paperboard, *International Journal of Solids and Structures* 48 (16) (2011) 2275–2287. [doi:10.1016/j.ijsolstr.2011.04.002](https://doi.org/10.1016/j.ijsolstr.2011.04.002).
- [124] L. Mentrasti, F. Cannella, M. Pupilli, J. S. Dai, Large bending behavior of creased paperboard. I. Experimental investigations, *International Journal of Solids and Structures* 50 (20) (2013) 3089–3096. [doi:10.1016/j.ijsolstr.2013.05.018](https://doi.org/10.1016/j.ijsolstr.2013.05.018).
- [125] S. W. Grey, F. Scarpa, M. Schenk, Mechanics of paper-folded origami: A cautionary tale, *Mechanics Research Communications* 107 (2020) 103540. [doi:10.1016/j.mechrescom.2020.103540](https://doi.org/10.1016/j.mechrescom.2020.103540).
- [126] C. Laschi, B. Mazzolai, M. Cianchetti, Soft robotics: Technologies and systems pushing the boundaries of robot abilities, *Science Robotics* 1 (1) (2016) eaah3690. [doi:10.1126/scirobotics.aah3690](https://doi.org/10.1126/scirobotics.aah3690).
- [127] K. Liu, L. S. Novelino, P. Gardoni, G. H. Paulino, Big influence of small random imperfections in origami-based metamaterials, *Proceedings of the Royal Society A: Mathematical, Physical and Engineering Sciences* 476 (2020) 20200236. [doi:10.1098/rspa.2020.0236](https://doi.org/10.1098/rspa.2020.0236).
- [128] S. V. Georgakopoulos, C. L. Zekios, A. Sattar-Kaddour, M. Hamza, A. Biswas, B. Clark, C. Ynchausti, L. L. Howell, S. P. Magleby, R. J. Lang, Origami antennas, *IEEE Open Journal of Antennas and Propagation* 2 (2021) 1020–1043. [doi:10.1109/OJAP.2021.3121102](https://doi.org/10.1109/OJAP.2021.3121102).